CHALMERS
UNIVERSITY OF TECHNOLOGY

Ultrasound-based assessment of skin and bone thickness in the temporal bone region

A feasibility study to support surgical planning in BAHS

Master's Thesis in Biomedical Engineering

Allegra Gasparetto & Victoria Steen

Department of Electrical Engineering, Division of Signal Processing and Biomedical Engineering
CHALMERS UNIVERSITY OF TECHNOLOGY
Gothenburg, Sweden 2026
www.chalmers.se

Master's thesis 2026

Ultrasound-based assessment of skin and bone thickness in the temporal bone region

A feasibility study to support surgical planning in BAHS

Allegra Gasparetto & Victoria Steen

CHALMERS
UNIVERSITY OF TECHNOLOGY

Department of Electrical Engineering
Division of Signal Processing and Biomedical Engineering
Chalmers University of Technology
Gothenburg, Sweden 2026

Ultrasound-based assessment of skin and bone thickness in the temporal bone region
A feasibility study to support surgical planning in BAHS

Allegra Gasparetto & Victoria Steen

Supervisor: Martin Johansson, Senior Director Research & Technology, Oticon Medical AB.

Supervisor: Karl-Johan Fredén Jansson, Researcher, Signal Processing and Biomedical Engineering, Electrical Engineering, Chalmers University of Technology.

Supervisor: Elangovan Yedeshkumar, Transducer Developer, Oticon Medical AB.

Examiner: Sabine Reinfeldt, Associate Professor, Signal Processing and Biomedical Engineering, Electrical Engineering, Chalmers University of Technology.

Master's Thesis 2026
Department of Electrical Engineering
Division of Signal Processing and Biomedical Engineering
Chalmers University of Technology
SE-412 96 Gothenburg
Telephone +46 31 772 1000

Cover: Conceptual visualization of a possible future handheld ultrasound thickness measurement device. Image generated using ChatGPT (OpenAI, 2026).

Typeset in LaTeX
Printed by Chalmers Reproservice
Gothenburg, Sweden 2026

Abstract

Hearing loss is a major global health concern, and bone-anchored hearing systems (BAHS) such as the Ponto™ system provide an important solution for patients who cannot benefit from conventional air conduction (AC) hearing aids. Successful implantation, however, depends strongly on the anatomical conditions at the implant site, where both cortical bone thickness and soft tissue thickness play critical roles in implant stability and soft tissue healing. In current clinical practice, bone thickness is typically assessed intraoperatively using a multi-step drilling procedure, while soft tissue thickness is measured manually with a needle and ruler during surgery. Preoperative computed tomography (CT) is therefore reserved mainly for patients with suspected abnormal anatomy, due to the associated ionizing radiation exposure and clinical cost. Ultrasound presents an attractive alternative because it is non-invasive, radiation-free, and widely accessible, and can be performed in the office prior ordering implants and performing the surgery.

While previous studies have explored ultrasound-based estimation of either soft tissue thickness or cranial bone thickness individually, limited research has addressed the combined assessment required for preoperative assessment in BAHS implantation. This thesis therefore investigated the feasibility of using ultrasound to simultaneously and site-specifically determine soft tissue and cortical bone thickness in the temporal bone region relevant to implantation of the Ponto™ system.

The study was conducted using analytical modelling and numerical simulations of ultrasound wave propagation in a multilayer structure. Different excitation waveforms, operating frequencies, and anatomical configurations were evaluated for their effects on signal amplitude, spatial pulse length (SPL), echo separability, and time-of-flight (ToF) accuracy.

The results demonstrated that ultrasound-based thickness determination is technically feasible under the investigated conditions. Across all simulated configurations, consistent interface reflections enabled reliable identification of relevant tissue boundaries. The findings showed that accurate determination of ToF is governed not by signal amplitude or SPL alone, but by the balance between signal strength, temporal compactness, and echo separability. Chirp excitation achieved a favourable combination of high voltage peak and low SPL, while pulse excitation demonstrated comparable overall performance. Stable ToF errors below 2–3 % were achieved in several configurations, with cortical bone consistently exhibiting lower error than soft tissue. The simulations further demonstrated robustness in the presence of blood vessels and secondary reflections, with a selected intermediate-frequency range providing the best compromise between penetration depth and temporal resolution.

Overall, the findings indicate that ultrasound has strong potential as a complementary tool for preoperative assessment in Ponto™ system implantation. Although further experimental validation is required, this work establishes a theoretical and numerical foundation for future development of ultrasound-based assessment methods for BAHS.

Keywords: ultrasound, A-mode ultrasound, temporal bone region, soft tissue thickness estimation, bone thickness estimation, BAHS, bone-anchored hearing system, preoperative assessment, non-invasive, feasibility study.

Acknowledgements

We would like to express our heartfelt gratitude to everyone who supported us throughout this Master's thesis journey. This project has been both challenging and rewarding, and it would not have been possible without the guidance, encouragement, and knowledge shared by so many people along the way.

First and foremost, we would like to sincerely thank our supervisor at Oticon Medical AB, Elangovan Yedeshkumar, for your continuous support, patience, and encouragement throughout the entire project. Your willingness to always make time for discussions, answer our questions, and guide us when we felt uncertain has meant a great deal to us. Beyond your technical guidance, we are especially grateful for the confidence you placed in us and for constantly encouraging us to grow, think independently, and trust our own abilities. Your support made a significant difference, both academically and personally.

We would also like to thank our supervisor at Oticon Medical AB, Martin Johansson, for your valuable insights, thoughtful feedback, and broad perspective throughout this work. Your experience helped us look beyond the details and better understand the bigger picture of the project, which greatly contributed to the direction and development of this thesis.

A sincere thank you also goes to our supervisor at Chalmers University of Technology, Karl-Johan Fredén Jansson, for your constructive feedback, guidance, and engaging discussions throughout the project. Your support and input have been highly appreciated during this process.

We would further like to thank our examiner, Sabine Reinfeldt, for your insightful feedback and support throughout the thesis work. Your perspectives encouraged us to reflect more critically on our work and helped strengthen the quality of the thesis.

In addition, we are very grateful to Johannes Kocher, Tomas Johansson, Maria Åberg Håkansson, and Marsel Ganeyev for generously sharing your knowledge, ideas, and time with us. The discussions, advice, and support you provided have been invaluable to the progress of this work.

Finally, we would like to acknowledge the use of AI language models for minor language assistance during the writing process, as well as for generating the illustrative image of the conceptual device design presented in the Future Work chapter. These tools were used carefully and responsibly and did not influence the scientific integrity or conclusions of this thesis.

To everyone who has been part of this journey, thank you. Your support, encouragement, and belief in us have made this experience both meaningful and unforgettable.

Allegra Gasparetto & Victoria Steen, Gothenburg, May 2026

List of Acronyms

Below is the list of acronyms that have been used throughout this thesis listed in alphabetical order:

AC	Air Conduction
atBCD	Active Transcutaneous Bone Conduction Device
BAHS	Bone-Anchored Hearing System
BC	Bone Conduction
BCD	Bone Conduction Device
CT	Computed Tomography
FWHM	Full Width at Half Maximum
MIPS	Minimally Invasive Ponto Surgery
percBCD	Percutaneous Bone Conduction Device
PMMA	Polymethyl Methacrylate
PRF	Pulse Repetition Frequency
ptBCD	Passive Transcutaneous Bone Conduction Device
PZT	Lead Zirconate Titanate
SNR	Signal-to-Noise Ratio
SNHL	Sensorineural Hearing Loss
SPL	Spatial Pulse Length
SSD	Single-Sided Deafness
ToF	Time-of-Flight

Nomenclature

Material Properties and Acoustic Quantities

ρ	Density of the medium
E	Young's modulus
ν	Poisson's ratio
K	Bulk modulus
G	Shear modulus
c	Longitudinal wave velocity
λ	Wavelength
f	Frequency
Z	Acoustic impedance
d	Layer thickness
R	Reflection coefficient at an interface
T	Transmission coefficient at an interface
t	One-way propagation time
t_{echo}	Round-trip echo time
Δt_{echo}	Time difference between consecutive echoes

System Constraints

t_{window}	Acquisition time window
PRF	Pulse repetition frequency
N_{cycles}	Number of excitation cycles
t_{exc}	Excitation duration
SPL	Spatial pulse length
R_{axial}	Axial resolution
Δt	Temporal discretization step
$h_{\max}$	Maximum mesh element size

Design Parameters

f_0	Operating frequency of the piezoelectric element
d_P	Thickness of the piezoelectric element
d_{BR}	Thickness of the buffer rod
D_P	Diameter of the piezoelectric element
N	Near-field length

Evaluation Metrics

V_P	Excitation voltage amplitude
$SPL@FWHM$	Spatial pulse length at full width at half maximum
ToF	Time-of-flight

Contents

List of Figures

List of Tables

1 Introduction

Hearing loss is a major global health concern affecting nearly 20 % of the population worldwide, with over 430 million people experiencing disabling forms of the condition [1]. Beyond impaired auditory perception, hearing loss is associated with reduced quality of life, social isolation, and increased cognitive burden, highlighting the importance of effective rehabilitation strategies.

Among the available treatment options, bone conduction (BC) hearing devices provide an important alternative for patients who cannot benefit from conventional air conduction (AC) hearing aids [2]. These systems transmit sound vibrations through the skull directly to the inner ear, bypassing the outer and middle ear. One widely used solution is the bone-anchored hearing system (BAHS), a bone conduction device (BCD). Successful implantation depends strongly on local anatomical conditions. Insufficient bone thickness may compromise implant stability and osseointegration, while inappropriate abutment length, the part that permanently penetrates the skin, relative to soft tissue thickness may cause skin reactions or reduced sound processor retention.

Currently, bone thickness is assessed intraoperatively using a multi-step drilling procedure, where either a 3 or 4 mm implant is selected. A one-stage procedure using a 4 mm implant is generally preferred due to its superior stability and survival rate. Soft tissue thickness is similarly determined intraoperatively using a needle and ruler, requiring multiple implant and abutment length combinations to be available during surgery. In cases of suspected abnormal anatomy, computed tomography (CT) may be used preoperatively to evaluate cranial bone structure [3]. However, CT involves ionizing radiation, is not always justified for routine use, and does not allow site-specific confirmation during surgery. A non-invasive and site-specific preoperative method for determining both bone and soft tissue thickness could therefore support optimal implant placement while avoiding thin bone regions, large blood vessels, or air pockets, and allow the correct implant-abutment combination to be selected prior to surgery.

Ultrasound offers a non-invasive, radiation-free, and cost-effective alternative widely available in clinical practice. The global medical ultrasound device market, valued at approximately US$ 7.9 billion in 2021, reflects its widespread adoption and ongoing technological development [4]. Ultrasound has been used in medical diagnostics since the early 20th century and is now one of the most widely used imaging modalities in medicine [5]. Previous studies have demonstrated its potential for measuring soft tissue thickness and cranial bone thickness, particularly using A-mode techniques [6–9], as well as for preoperative assessment [10]. However, existing work has largely evaluated these parameters separately, despite both being required for preoperative assessment in BAHS implantation.

The present work addresses this gap by investigating the feasibility of an ultrasound-based method for the combined and site-specific determination of soft tissue and cortical bone thickness in the temporal region relevant to implantation of the Oticon Ponto™ system. Using analytical and numerical approaches, the study evaluates whether ultrasound can provide sufficient accuracy for preoperative thickness assessment and explores key factors influencing measurement performance.

1.1 Oticon Medical AB and Clinical Context

This thesis was carried out in collaboration with Oticon Medical AB (Askim, Sweden), a company developing implantable BC hearing solutions, including the Oticon Ponto™ system which serves as the clinical application context of the project [11, 12]. Ultrasound offers a non-invasive, radiation-free approach for determining tissue thickness. By transmitting acoustic signals into the intended implant site and analysing reflected echoes, it may enable the determination of both soft tissue and bone thickness. However, the layered anatomy of the region makes this technically challenging. Hereafter, the Oticon Ponto™ system is referred to as the Ponto system.

1.2 Aim and Research Questions

The aim of this thesis is to investigate the feasibility of an ultrasound-based method for determining site-specific soft tissue thickness and cortical bone thickness in the temporal bone region relevant to preoperative assessment in Ponto system implantation. The work is based on analytical and numerical methods and focuses on the potential of ultrasound for preoperative thickness assessment. The thesis addresses the following research questions:

- To what extent can the local soft tissue thickness in the temporal bone region be accurately determined using ultrasound-based methods?
- To what extent can the local cortical bone thickness be determined using ultrasound, considering the limitations of wave propagation in hard tissue?
- Is the achievable measurement accuracy sufficient to meet the clinical requirements for implantation of the Ponto system?
- What are the key design parameters of an ultrasonic transducer required to enable a reliable determination of tissue thickness in this application?

1.3 Limitations

This thesis is limited to analytical and numerical evaluation of ultrasound-based method for determining thickness and does not include full device development or regulatory certification. Although experimental validation is subsequently warranted, it could not be executed within the time constraints for this work. Proposed next steps, including experimental validation and future device design, is however outlined in this report. The proposed method is intended for the determination of local thickness at the planned implant site in the context of the Ponto system and is not intended to replace diagnostic imaging when broader anatomical assessment is required.

2 Theory

This chapter presents the theoretical foundations relevant to this thesis. It begins with an overview of head anatomy and the auditory system, followed by the physiological mechanisms of hearing and the main types of hearing loss to establish the clinical context. BAHS, with particular focus on the Ponto system and its surgical aspects, are then introduced. The chapter continues with the fundamental principles of ultrasound, including wave propagation, key acoustic parameters, and transducer design, before discussing its applications in medical imaging and interaction with biological tissues. Finally, the principles of ultrasound-based thickness estimation are presented, with emphasis on ToF methods and factors affecting measurement accuracy.

2.1 Anatomy of the Head

This section presents an overview of the anatomy of the human head relevant to this thesis, including the human scalp, skull, and dura mater.

2.1.1 The Scalp

The scalp forms the superficial soft tissue covering the skull [13]. It consists of five layers, remembered by the mnemonic SCALP: skin, connective tissue, aponeurosis, loose connective tissue and periosteum (Figure 2.1). The skin is relatively thick and often hair-bearing [13, 14].

Under the skin lies a dense connective tissue layer containing the principal blood vessels and nerves of the scalp. This layer connects the skin layer to the epicranial aponeurosis, a tendon-like layer that connects the frontalis and occipital muscles. The loose, connective tissue layer beneath it contains numerous blood vessels and allows movement of the scalp over the underlaying skull, and separates the aponeurotic layer from the periosteum. The periosteum is the deepest layer of the scalp and adherent to the outer surface skull bones at the cranial sutures.

In this thesis, “skin” is sometimes used as a simplified term for the soft tissue layer overlying the skull.

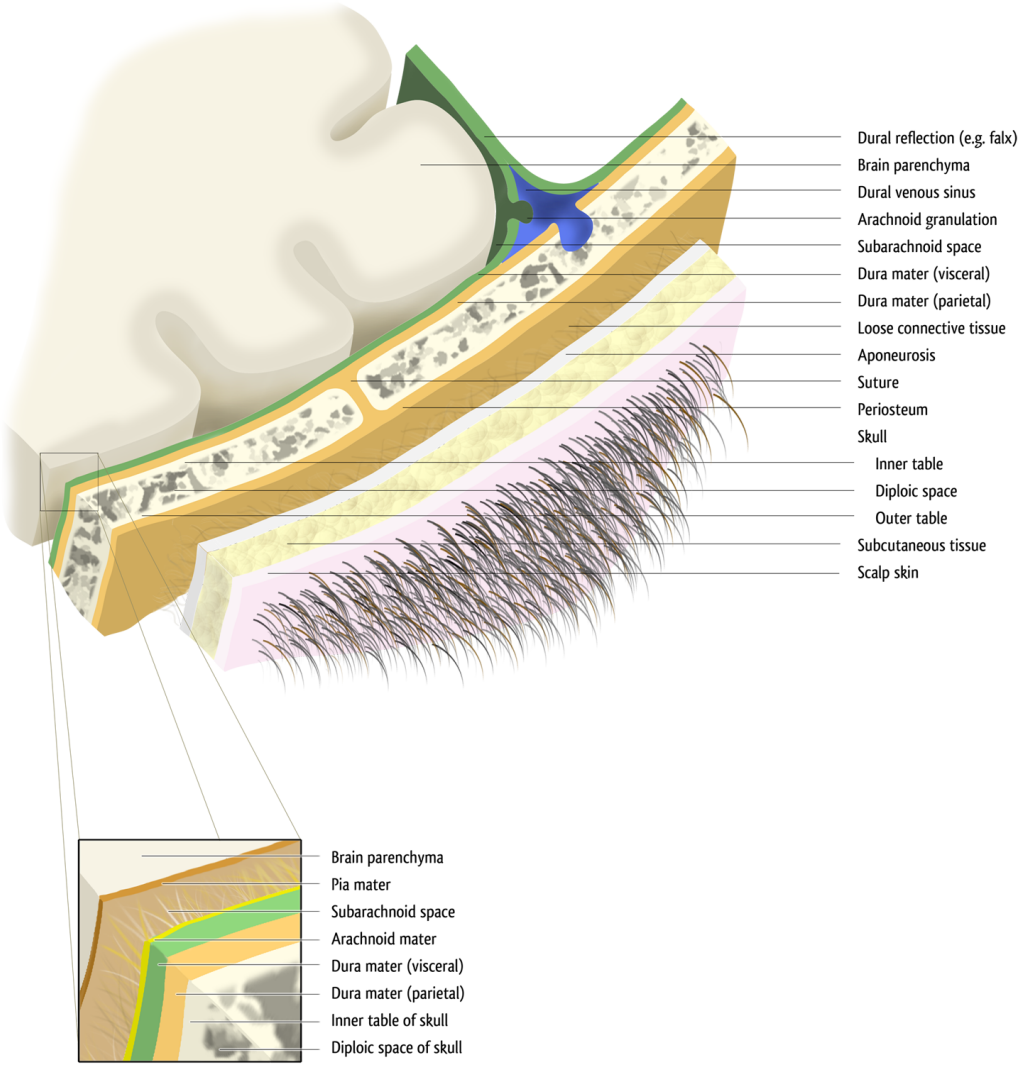

Figure 2.1: Schematic illustration of the layered anatomy of the scalp, skull, and intracranial meningeal structures, including the relationships between the soft tissues, cranial bone layers, and dura mater [15].

2.1.2 The Skull

The skull, or cranium, is the most superior part of the human axial skeleton and forms a rigid protective casing for the brain and related structures [16]. In most adults, the skull consists of 22 bones joined in cranial sutures, providing structural integrity while also reflecting developmental growth patterns. Beyond protecting the brain, the skull defines the shape of the head, provides attachment sites for muscles and tendons of the scalp and face, and contains multiple openings that allow nerves and blood vessels to pass between intracranial and extracranial regions.

Anatomically, the skull is divided into the neurocranium, which encloses the brain, and the viscerocranium, which forms the facial skeleton [16]. The upper part of the neurocranium, the calvaria, includes the frontal, parietal, temporal, and occipital bones (Figure 2.2). It is organized by large sutures lines, such as the coronal, sagittal, squamosal, and lambdoid sutures.

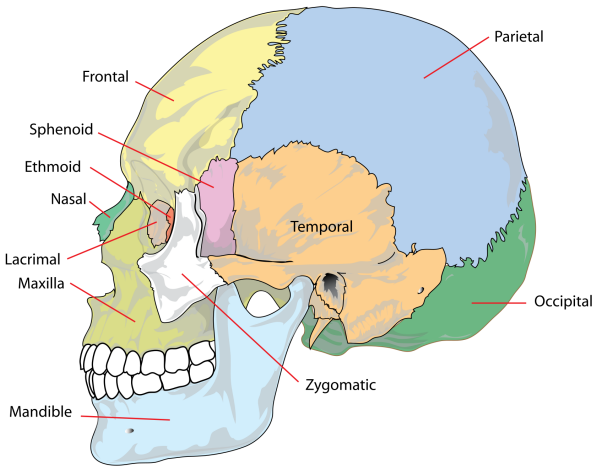

Figure 2.2: Lateral view of the human skull illustrating the major cranial and facial bones, with emphasis on the temporal bone region relevant to BAHS implantation [17].

2.1.2.1 The Temporal Bone

The temporal bone is the largest bony structure in the temporal region of the human skull [18]. The temporal bone is closely related to hearing and balance. It includes a dense, compact region which, due to its pyramidal geometry and hardness, is often referred to as the *petrous pyramid*. Anatomically, the temporal bone contains key structures involved in hearing, including the ear canal, ossicles in the middle ear structures that transmit sound, and the cochlea in the inner ear, as well as the balance organs (Figure 2.3) [18]. Important nerves also pass through it via the internal auditory canal, including the facial nerve (cranial nerve VII) and the vestibulocochlear nerve (cranial nerve VIII). In a clinical way, the mastoid part of the temporal bone is relevant, as it is commonly used as the fixation site for BAHS.

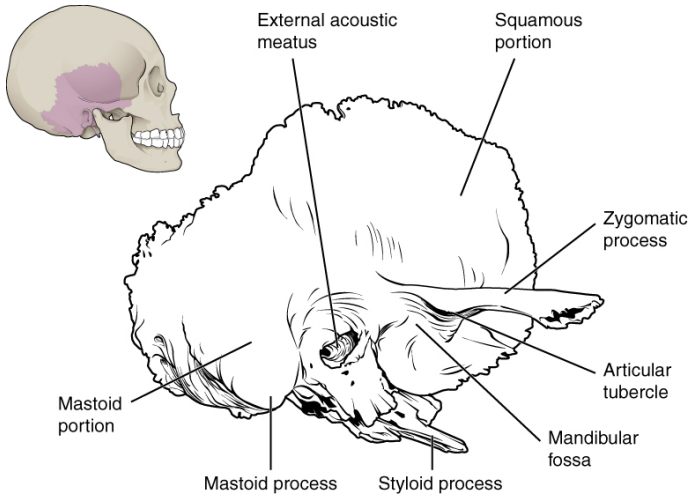

Figure 2.3: Overview of the structure of the temporal bone [19].

2.1.3 The Dura Mater

The dura mater, or dura, is a layer of connective tissue that surround the brain and spinal cord [20]. It is a dense and fibrous tissue that consists of a periosteal/endosteal layer that covers the inner surface of the skull and a meningeal layer that continues as the spinal dura. Between these two layers lie the dural venous sinuses. The dura also forms folds that help support the brain and limit its movement within the skull. Since it forms an important protective barrier around the brain, its anatomy is clinically relevant in cranial surgery and trauma.

2.2 The Auditory System

The human auditory system converts acoustic pressure waves into neural signals through a set of mechanical and sensory processes. Understanding the key anatomical structures involved in this process is essential to differentiate AC hearing from BC hearing and to motivate rehabilitation approaches that bypass parts of the system.

2.2.1 Anatomy of the Auditory System

The ear is commonly divided into three parts; the outer ear, middle ear, and inner ear (Figure 2.4) [21, 22]. The outer ear consists of the auricle, also known as the pinna, which is the visible part of the ear responsible for collecting sound waves from the surrounding environment. Included in the outer ear is the external ear canal and the tympanic membrane, also known as the eardrum. The tympanic membrane is what separates the outer ear and the middle ear. The middle ear is an air-filled space limited internally by the oval window. This space contains three small bones, or ossicles, called the malleus, the incus and the stapes. The main function of the middle ear is to transmit vibrations of incoming sound waves to the inner ear via the ossicles. The inner ear contains the cochlea, as well as a cavity filled with semicircular canals called the vestibule. The vestibule is responsible for

sensing position and motion. The cochlea is also part of where the vestibulocochlear nerve forms that transmit sound to the brain.

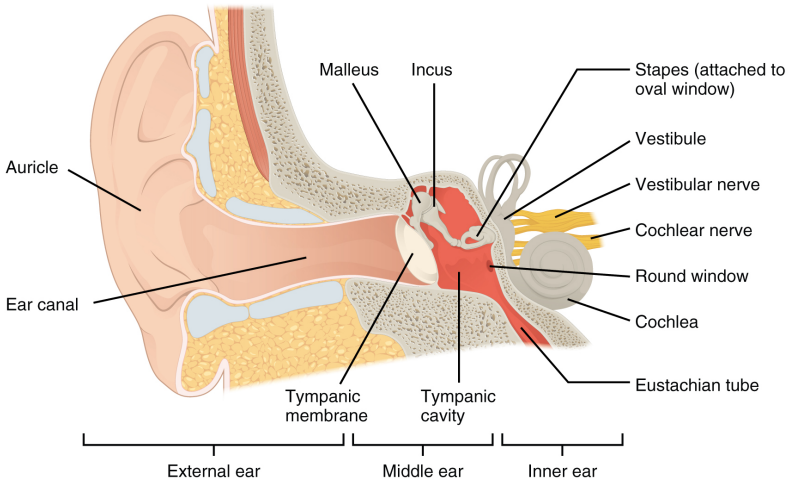

Figure 2.4: Anatomy of the human ear: outer, middle, and inner sections [23].

2.3 Physiology of Hearing

Hearing can be mediated through AC or BC. Although AC is the most common pathway in perceiving sound, BC provides an alternative path that becomes clinically important when the function of the outer or middle ear is compromised. This section provides an overview to AC hearing and BC hearing.

2.3.1 Air Conduction

With AC, the outer ear collects sound waves from the environment to the ear canal [21]. Sound waves cause the tympanic membrane to vibrate, which in turn stimulates the ossicles. The ossicles pass the energy of the vibrations to the cochlea. The cochlea is filled with fluid and its internal walls houses sensorineural hair cells [22]. The vibrations will cause the fluid to ripple and stimulate the sensorineural hair cells, inducing a neural-electrical potential and thus translating mechanical sound vibrations into electrical signals. These signals are then carried by the auditory nerve to the brain, where they are perceived as sound.

2.3.2 Bone Conduction

BC is the process where sound is transmitted to the cochlea through vibrations of the skull bone, cartilage and soft tissues [24, 25]. These vibrations set the cochlear fluids and inner structures in motion, stimulating the mechanisms responsible for hearing. In contrast to AC, where sound travels through the outer and middle ear, BC bypasses these structures and directly stimulates the inner ear. Thus, BC provides an alternative hearing pathway that does not depend on the normal function

of the outer or middle ear.

2.4 Hearing Loss

Hearing loss is commonly categorized by the anatomical location of the impairment. This categorization provides a useful framework for describing symptoms and underlying mechanisms and is closely related to the choice of clinical intervention. In this section, conductive hearing loss, sensorineural hearing loss, mixed hearing loss, and single-sided deafness are described.

2.4.1 Conductive Hearing Loss

Conductive hearing loss occurs when sound transmission is compromised in the outer or middle ear, meaning there is a loss of sound transmission from the pinna to the inner ear [22]. Problems that can occur resulting in a conductive hearing loss can be due to perforation of the tympanic membrane or loss of ossicular function, among others. Hearing loss due to these complications can often be restored with surgical intervention. Conductive hearing loss may also arise from congenital abnormalities, such as incomplete formation of the external ear or the external auditory canal [26]. In addition, blockage of the external auditory canal by cerumen, debris, or foreign bodies, for example, can reduce sound transmission and lead to conductive hearing loss.

2.4.2 Sensorineural Hearing Loss

Sensorineural hearing loss (SNHL) occurs when there are complications in the neural transmission of sound [22]. The parts of the ear associated with SNHL are the cochlea and the auditory nerve. Damages to these organs can be caused by various diseases or disorders, most often resulting in the loss of hair cells in the cochlea. Different regions of the cochlea handle different frequencies of sound. The loss of hair cells at the base of the cochlea causes a loss of high-pitched sound, whereas the loss of hair cells near the apex causes a loss of low-pitched sound.

2.4.3 Mixed Hearing Loss

Mixed hearing loss occurs when there are both conductive and sensorineural components that contribute to the hearing loss [22].

2.4.4 Single-sided Deafness

Single-sided deafness (SSD) occurs when there is a hearing loss in one ear while the other ear functions as near-normal or normal [27]. The hearing loss in the impaired ear is commonly a severe to profound SNHL. Difficulties with sound localization, noisy environments, tinnitus, and perception of position and motion are typical effects of SSD.

2.5 Bone Conduction Devices

Unlike conventional AC hearing aids, BCDs are devices that transmit sound to the cochlea by mechanical vibration of the skull [2, 28]. BCDs include both non-surgical conventional devices, for example devices worn on a softband, and implantable devices. Implantable BCDs can be divided into percutaneous BCDs (percBCDs), passive transcutaneous BCDs (ptBCDs), and active transcutaneous BCDs (atBCDs) [2, 29].

In a percBCD, the external sound processor is connected to an osseointegrated implant through a skin-penetrating abutment. Because the implant is anchored directly to the skull bone, these devices are commonly referred to as BAHS. This direct mechanical coupling allows sound vibrations to be transmitted efficiently to the skull bone, bypassing the outer and middle ear.

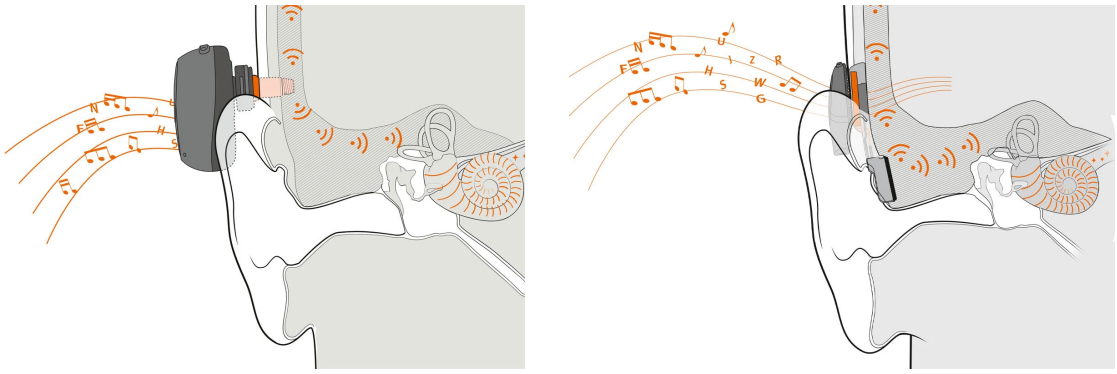

(a) Percutaneous implant **(b)** Transcutaneous implant

Figure 2.5: Different designs of implantable BCDs: (a) Oticon Ponto System (percBCD), (b) Oticon Sentio™ System (atBCD). Images reproduced with kind permission from Oticon Medical AB ©.

The clinical use of BAHS is well established in cases where middle ear surgery has failed to treat the hearing. Examples of currently available percBCDs include the Ponto system (Oticon Medical AB, Askim, Sweden) [30], and the Cochlear™ Baha® Connect System (Cochlear Bone-Anchored Solutions AB, Mölnlycke, Sweden), [31]. In this thesis, the Ponto system is described as a representative example of a percBCD/BAHS.

2.5.1 The Oticon Ponto™ System

Commercially introduced in 2009, the Ponto system is a BAHS and one of the clinically available BAHS options for individuals with hearing loss [32]. It consists of an osseointegrated titanium implant with a skin-penetrating abutment mounted on top that provides percutaneous connection, and an external sound processor attached to the abutment (Figure 2.6a) [33]. The implant is inserted in the temporal bone, while the abutment connects the implant to the external sound processor and enables transmission of vibrations to the skull. The abutment is currently available in four different lengths: 6 mm, 9 mm, 12 mm and 14 mm (Figure 2.6b) [3]. The

appropriate abutment length is selected based on the patient's soft tissue thickness, with the respective lengths intended for tissue thickness ranges of 0.5-3 mm, 3-6 mm, 6-9 mm and 9-12 mm. The implant is available in lengths of 3 mm and 4 mm, where the appropriate length is selected based on the thickness of the skull bone.

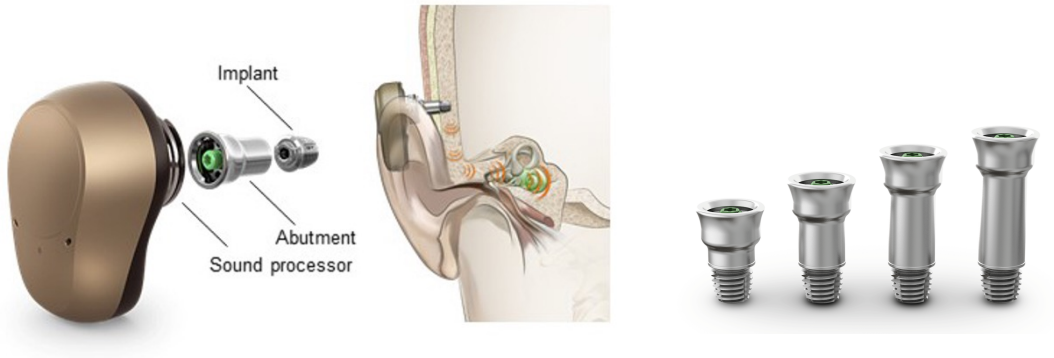

(a) Ponto system with implant.

(b) Examples of abutments used with the system.

Figure 2.6: Overview of the Ponto system and its main components used in bone-anchored hearing rehabilitation. The figure illustrates (a) the sound processor, abutment, connection screw, and titanium implant, where vibrations generated by the sound processor are transmitted through the skull bone to the cochlea via BC, and (b) the available abutment lengths used to connect the external sound processor to the implant. Images reproduced with kind permission from Oticon Medical AB ©.

2.5.2 Surgical Relevance of Skin and Bone Thickness

Skin and bone thickness at the planned implant site are important considerations in Ponto implantation. Soft tissue thickness is used for abutment selection, whereas bone thickness and bone quality influence the choice of surgical approach, including whether a single-stage or two-stage procedure is appropriate. Certain surgical approaches have more specific anatomical requirements, making preoperative assessment of local tissue dimensions clinically relevant for planning and safe implantation, particularly for patient with expected anatomical variations.

2.6 Implantation of the Ponto System

Surgical techniques used for Ponto system implantation have developed from the linear incision technique with tissue preservation toward increasingly minimally invasive approaches. As the suitability of different surgical techniques depends in part on local anatomical conditions, preoperative assessment of the implant site is an important component of surgical planning. While the linear incision technique remains a well-established and broadly applicable method, newer techniques such as minimally invasive Ponto surgery (MIPS) and MONO have been developed with the aim of reducing soft tissue trauma and improving surgical efficiency. Both linear incision and MIPS technique rely on a three step drilling with stepwise deepening of the bone cavity, whereas the MONO is performed in a single drilling step.

2.6.1 Preoperative Assessment

According to the Ponto surgical manual and the MONO addendum, preoperative assessment of the implant site includes evaluation of soft tissue thickness and expected bone conditions, since these factors influence both abutment selection and the choice of surgical technique [3, 34]. Soft tissue thickness may be assessed using a needle and a ruler, and conventional ultrasound may also be used in some cases. Bone thickness and quality are considered intraoperatively and verified during the drilling phase and may, when indicated, be preoperatively evaluated using radiological imaging such as CT, particularly when thin bone is suspected.

2.6.2 Linear Incision Procedure

The Linear incision procedure with tissue preservation is an established surgical procedure for implantation of the Ponto system [3]. In this procedure, after measuring the skin thickness, a linear skin incision is made down to the periosteum. The incision is opened and the periosteum is removed around the implant site. A guide drill is used to perform the two-step drilling to assess bone thickness and prepare the osteotomy, followed by widening the hole with a countersink drill. After insertion of the implant, a biopsy punch is used to create a hole over the abutment. The skin is then eased over the abutment and the incision is sutured closed and a healing cap and dressing are applied. The procedure can be performed as a single-stage or two-stage surgery, where the most fitting choice depends primarily on bone quality and bone thickness. Single-stage surgery is recommended for most adults with normal bone quality above 3 mm, whereas two-stage surgery is recommended in cases of thin bone or poor bone quality.

In a randomized controlled trial by Calon et al., the linear incision technique with tissue preservation was used as the control method [28]. Although the procedure represented an improvement over older methods, the authors noted that the procedure still requires greater tissue manipulation due to flap elevation and suturing, which may increase discomfort for the patient. This was part of the rationale for the development of less invasive techniques.

2.6.3 Minimally Invasive Ponto Surgery

Minimally Invasive Ponto Surgery (MIPS) was developed as a punch-only alternative to the linear incision procedure. The aim was to reduce tissue trauma while preserving surrounding soft tissue and vascular supply [28]. Instead of making a linear incision and raising a flap, MIPS uses a small circular punch incision. The procedure is then performed directly through the circular punch opening, without the need for a linear incision or flap elevation. The rationale behind this method is that maintaining the surrounding soft tissue integrity may support more effective wound healing and reduce postoperative complications.

In the trial by Calon et al., MIPS resulted in significantly reduced loss of skin sensibility, less skin sagging, improved cosmetic outcomes and shorter surgical time compared with the linear incision procedure [28]. A retrospective 10-year study by Cruz et al. supports the general shift toward minimally invasive approaches in bone-anchored hearing implant surgery [35]. Minimally invasive techniques showed significantly shorter surgery duration than the linear incision procedure and less frequent reports of postoperative complications.

2.6.4 MONO Procedure

The MONO procedure for Ponto implantation is a newer minimally invasive technique developed to refine the MIPS procedure [34]. It follows the same general minimally invasive approach as MIPS, but differs in the drilling stage. Its defining feature is that the osteotomy is prepared in a single drill step rather than through a multi-step drill sequence used in both MIPS and the linear incision technique.

MONO is a single-stage procedure intended for adult patients with normal anatomy, expected bone thickness of at least 5 mm and soft tissue thickness of 12 mm or less [34]. Hence, this technique is only intended for the 4 mm implant. In order to standardise and streamline the technique, a MONO Surgery Kit has been developed (Figure 2.7), containing a cannula, the MONO drill, a soft healing cap and an insertion indicator [36]. The drill used in the MONO procedure has a parabolic twist design intended to allow the osteotomy to be prepared in a single drilling step. Preclinical evaluations have also reported lower heat generation than with the conventional linear incision and MIPS drill systems.

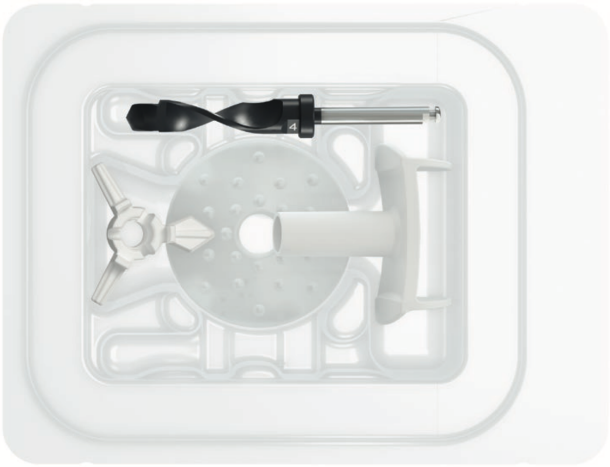

Figure 2.7: The MONO Surgery Kit, containing a cannula, the MONO drill, a soft healing cap and an insertion indicator. Images reproduced with kind permission from Oticon Medical AB. ©

2.7 Fundamentals of Ultrasound

Ultrasound refers to mechanical pressure waves with frequencies above the upper limit of human hearing, typically above 20 kHz. In medical and ultrasonic measurement applications, frequencies are commonly in the megahertz range [4, 37, 38]. These waves propagate through elastic media as mechanical disturbances characterized by variations in pressure, density, and particle motion.

The understanding of acoustic wave propagation, wavelength, acoustic impedance, and wave interactions at material interfaces is essential for the design of ultrasonic measurement systems. In the context of this thesis, these principles form the theoretical foundation for the development of a pulse-echo system for the determination of biological layer thicknesses, particularly skin and bone.

2.7.1 Acoustic Wave Propagation

Ultrasound propagates as an acoustic wave, meaning that it is a mechanical disturbance transmitted through a material medium by coupled fluctuations of pressure and particle displacement [4, 38]. As the wave travels, particles oscillate around their equilibrium positions, creating successive compressions and rarefactions that transport energy without causing net transport of matter (Figure 2.8). In solids, different wave modes may exist, including longitudinal, shear, and surface waves. However, in fluids and soft biological tissues, shear waves are strongly attenuated or do not propagate efficiently due to the negligible shear rigidity of the medium. Therefore, ultrasonic propagation in these media is dominated by longitudinal waves, in which particle motion is parallel to the direction of wave propagation. For this reason, only longitudinal waves are considered in this study.

The propagation velocity of ultrasound depends on the mechanical properties of the medium, primarily its density and elastic stiffness [4, 38]. In general, stiffer

and less compressible materials support higher sound velocities. Consequently, ultrasound propagates relatively slowly in soft tissue and considerably faster in dense structures such as cortical bone. This variation in wave velocity plays a central role in determining both the interaction of ultrasound with biological structures and the interpretation of reflected signals.

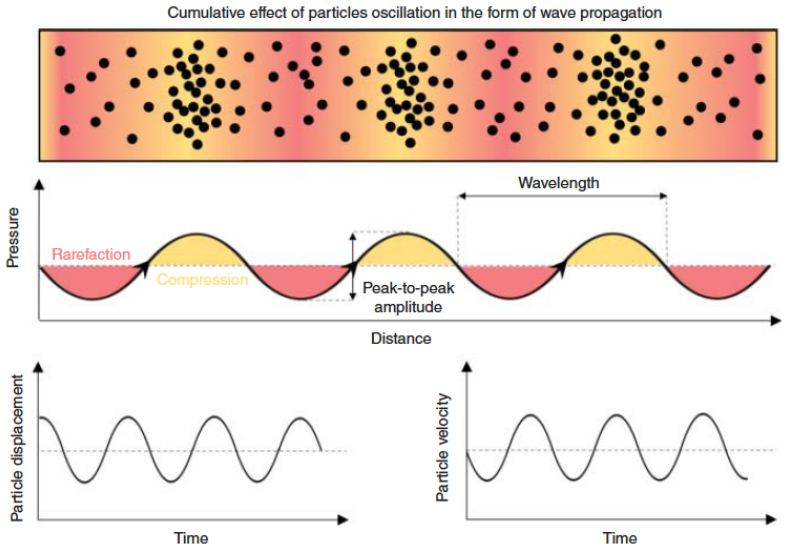

Figure 2.8: Illustration of acoustic wave propagation and its fundamental properties. The figure shows the relationship between particle oscillation and wave propagation, including regions of compression and rarefaction, wavelength, pressure variation, particle displacement, and particle velocity as functions of distance and time [38].

2.7.2 Wavelength, Frequency and Resolution

A key parameter in ultrasound is the operating frequency, which in medical applications commonly ranges from 2 MHz to 20 MHz [37, 38]. The wavelength λ is the spatial distance between two successive compressions and is related to the propagation speed c and frequency f by:

$$\lambda = \frac{c}{f} \tag{2.1}$$

This relationship shows that higher frequencies correspond to shorter wavelengths. Since wavelength defines the minimum spatial scale that can be resolved, shorter wavelengths provide improved spatial resolution and enable the detection of thinner layers and smaller structures. However, increasing the frequency also leads to increased attenuation, particularly in highly absorptive and scattering media such as bone. As a result, the selection of the operating frequency involves a fundamental trade-off between spatial resolution and penetration depth. This trade-off is a key design consideration in the ultrasonic system developed in this work.

2.7.3 Acoustic Impedance

A central parameter governing ultrasound propagation is the acoustic impedance [4, 38]. Physically, acoustic impedance represents the opposition of a medium to particle motion induced by pressure variations, indicating how much pressure is required to generate a given motion within the material. It is defined as

$$Z = \rho c \tag{2.2}$$

where ρ is the density of the medium and c is the speed of sound within it. By combining both inertial and elastic properties, acoustic impedance serves as a fundamental descriptor of how a material responds to acoustic excitation. Media with high acoustic impedance require larger pressure amplitudes to achieve the same particle velocity, whereas low-impedance materials respond more readily to the passage of an acoustic wave.

In biological systems, acoustic impedance varies significantly with tissue composition [4, 37]. Soft tissues typically exhibit values around 1.5–1.7 MRayl, while cortical bone commonly ranges from approximately 6 to 8 MRayl. Piezoelectric ceramics such as Lead zirconate titanate (PZT) exhibit considerably higher values, often above 20 MRayl. These differences directly determine how ultrasound behaves at material interfaces.

2.7.4 Reflection and Transmission at Interfaces

When an ultrasonic wave reaches an interface between two media with different acoustic impedances, part of the wave is reflected and part is transmitted (Figure 2.9) [4, 37, 38]. This behaviour follows from the continuity of pressure and particle velocity at the boundary. The proportion of the reflected wave amplitude depends on the degree of impedance and can be quantified by the pressure amplitude reflection coefficient:

$$R = \frac{Z_2 - Z_1}{Z_2 + Z_1} \tag{2.3}$$

where Z_1 and Z_2 are the acoustic impedances of the first and second media, respectively. When the acoustic impedances are similar, most of the wave energy is transmitted, whereas large acoustic impedance mismatches result in strong reflections and limited transmission.

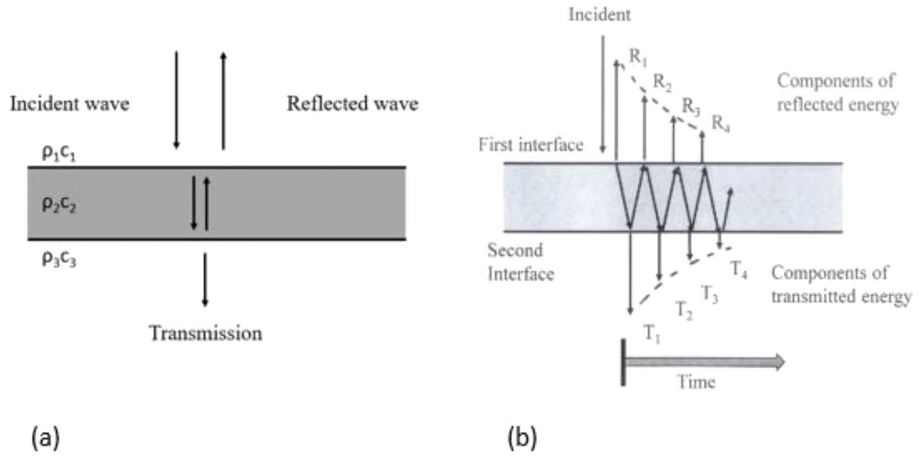

Figure 2.9: Reflection and transmission of a longitudinal wave at normal incidence on an interface between two media with different acoustic impedances: (a) single reflection and transmission, and (b) multiple reflections within the second medium. (From: Ultrasonics, 4th Edition by Leonard Bond, Copyright © 2024 by CRC Press. Reproduced by permission of Taylor & Francis Group.)

This behaviour has two important implications. On one hand, acoustic impedance mismatches are essential for ultrasonic measurement techniques, as they generate the echoes that reveal the location and properties of internal structures. On the other hand, excessive mismatches can significantly reduce the amount of energy transmitted into the medium, thereby limiting penetration depth and signal strength.

Importantly, acoustic impedance mismatches are not only present within the biological medium but also within the ultrasonic system itself. If not properly controlled, these internal reflections can reduce transmission efficiency and introduce additional echoes that complicate signal interpretation.

2.8 Ultrasound Signal Excitation and Measurement Modes

Building on the fundamental principles of ultrasound propagation and wave interaction described in the previous section, practical ultrasonic systems require controlled generation and measurement of these waves. The characteristics of the excitation signal and the selected measurement mode directly influence resolution, penetration depth, and overall system performance. For this reason, parameters such as frequency content, signal duration, waveform shape, and operating mode must be carefully selected in accordance with the specific application.

2.8.1 Center Frequency and Bandwidth

The center frequency represents the main operating frequency of the transmitted ultrasonic signal and is typically selected close to the resonance frequency of the piezoelectric transducer [4, 37]. It determines both the wavelength of the transmitted wave and the penetration characteristics within the medium. Higher center

frequencies correspond to shorter wavelengths and therefore improve spatial resolution, allowing smaller interfaces and thinner layers to be distinguished. However, higher frequencies are also associated with increased attenuation, particularly in highly scattering media such as bone, which reduces penetration depth and weakens deeper echoes.

Closely related to the center frequency is the bandwidth, which describes the range of frequencies over which the transducer and excitation signal can operate effectively [4, 37]. It is commonly defined around the center frequency and is directly linked to the temporal characteristics of the transmitted signal. A wide bandwidth enables the generation of short pulses, improving temporal resolution and facilitating the separation of closely spaced echoes. This is particularly important in pulse-echo thickness estimation for accurate identification of front-wall and back-wall reflections, coming from the beginning nad the end of a layer. In contrast, narrowband systems are associated with longer pulses and reduced temporal resolution, which may lead to overlap between echoes originating from adjacent interfaces.

2.8.2 Signal Duration

The duration of the transmitted signal is a key parameter affecting both temporal resolution and signal energy [4, 37]. Short-duration pulses provide high temporal resolution, allowing echoes from closely spaced interfaces to be clearly separated in time. This is essential for reliable determination of thickness of thin biological layers such as skin and bone.

However, short pulses contain less acoustic energy, which can reduce the amplitude of the received echoes and lower the signal-to-noise ratio (SNR) [4, 37]. This limitation becomes particularly relevant in highly attenuating media, where deeper reflections are already weak. Longer excitation signals, in contrast, carry more energy and improve signal detectability and SNR. The trade-off is reduced temporal resolution, since echoes from nearby interfaces may overlap in time.

This balance between temporal resolution and transmitted energy is therefore a central consideration in ultrasonic system design.

2.8.3 Excitation Waveform Shape

Beyond duration alone, the shape of the excitation waveform determines how energy is distributed in both time and frequency.

A short pulse is commonly used in pulse-echo systems because it provides excellent temporal resolution and facilitates echo separation [4]. However, due to its short duration, the transmitted energy is limited. A sine burst consists of a finite number of sinusoidal cycles at a defined frequency. Compared to a single pulse, it provides higher transmitted energy and improved control over the frequency content, but its longer duration may reduce temporal resolution.

For applications requiring both high transmitted energy and good temporal resolution, coded excitation techniques such as chirp signals can be employed [6] [39]. A chirp is a frequency-modulated waveform in which the frequency varies continuously over time within a defined bandwidth. This approach allows a long-duration, high-energy signal to be transmitted while maintaining high temporal resolution through pulse compression during signal processing. Such techniques are particularly advantageous in highly attenuating media, where sufficient transmitted energy is required to detect weak reflections from deeper interfaces.

2.8.4 Excitation Voltage

The excitation voltage determines the amplitude of the electrical signal applied to the piezoelectric transducer and directly influences the amplitude of the generated ultrasonic wave [4, 37]. Higher excitation voltages produce larger mechanical deformation of the piezoelectric element, resulting in stronger transmitted acoustic pressure waves and increased echo amplitudes. This improves signal detectability and can enhance the SNR, particularly for weak reflections originating from deeper structures.

However, the excitation voltage must remain within the operational limits of both the transducer and the driving electronics to avoid material damage, non-linear behaviour, or excessive heating.

2.8.5 Operating Modes

Ultrasonic systems can operate in different measurement modes depending on the intended application [4, 37]. In amplitude mode (A-mode), the received signal is represented as echo amplitude as a function of time or depth, where each peak corresponds to a reflecting interface within the medium. This mode is particularly suitable for thickness estimation and is the primary operating mode considered in this work. Brightness mode (B-mode) extends this concept by converting echo amplitudes into brightness values to form a two-dimensional cross-sectional image. While B-mode is widely used in clinical imaging, A-mode provides a more direct representation of echo timing and is therefore better suited for precise thickness measurements.

2.8.6 Pulse-echo Measurement Principle

In a pulse-echo system, a single transducer is used to both transmit and receive the ultrasonic signal (Figure 2.10) [4, 37]. An electrical excitation is applied to the transducer, causing it to emit an ultrasonic pulse into the medium. As the wave propagates, it encounters interfaces where acoustic properties change, such as between skin and bone. At each interface, part of the wave is reflected back toward the transducer, while the remainder continues deeper into the medium. The returning echoes are then converted back into electrical signals, with each echo corresponding to a specific interface.

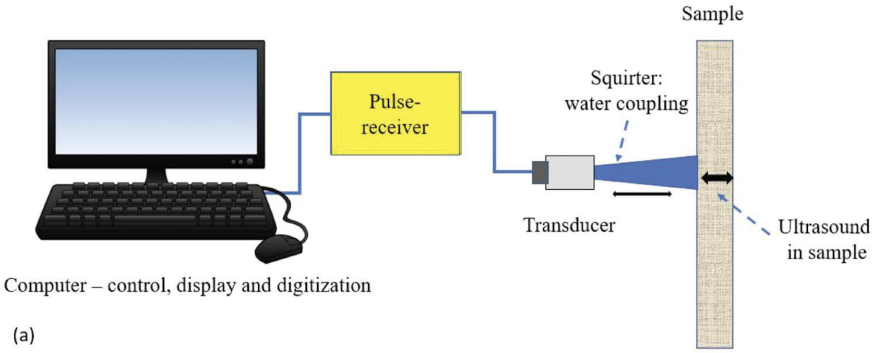

Figure 2.10: Schematic illustration of a pulse-echo ultrasonic measurement system used for ultrasound signal acquisition. The figure shows the main components involved in signal generation, wave propagation through the medium, reflection at material interfaces, and reception of the returning echoes by the transducer. (From: *Ultrasonics*, 4th Edition by Leonard Bond, Copyright © 2024 by CRC Press. Reproduced with permission from Taylor & Francis Group.)

The ability to distinguish between these echoes depends critically on their temporal separation. If the transmitted signal is too long, or if interfaces are closely spaced, the echoes may overlap and become difficult to resolve. Consequently, signal duration and bandwidth play a crucial role in measurement accuracy. In addition, attenuation reduces the amplitude of echoes from deeper structures, making the detection of weak signals, such as the back-wall reflection of bone, particularly challenging. This further emphasizes the importance of carefully selecting excitation parameters and signal processing strategies.

2.9 Piezoelectric Ultrasonic Transducers Design

Having established how ultrasonic signals are generated and measured, the practical realization of an ultrasonic system requires a device capable of both generating and receiving acoustic waves. This function is performed by an ultrasonic transducer, which converts electrical energy into mechanical waves and vice versa through the piezoelectric effect (Figure 2.11) [4, 37].

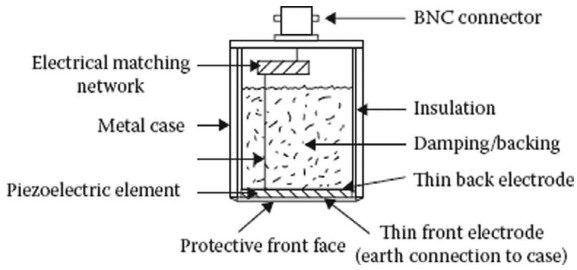

Figure 2.11: Cross-sectional view of an ultrasonic transducer based on a piezoelectric element. The figure illustrates the internal transducer structure, including the piezoelectric material, backing layer, and acoustic matching layer used to improve ultrasonic wave transmission and reception. (From: *Ultrasonics*, 4th Edition by Leonard Bond, Copyright © 2024 by CRC Press. Reproduced with permission from Taylor & Francis Group.)

2.9.1 Piezoelectric Transducer Principle

Piezoelectric materials contain small electric dipoles that can be aligned through a polarization process [4, 37]. After polarization, the material is able to convert electrical energy into mechanical motion, and mechanical motion into electrical signals, a behaviour known as electromechanical coupling (Figure 2.12). When an electrical signal is applied, the material expands and contracts, generating ultrasonic waves that propagate into the surrounding medium. After transmission, the same element functions as a receiver, converting returning echoes into measurable electrical signals.

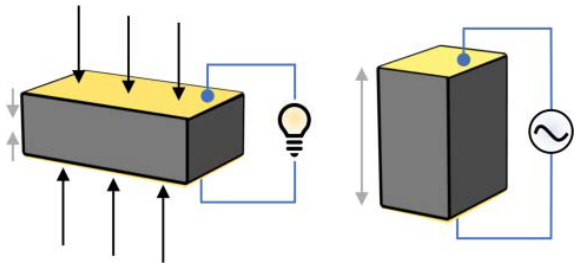

Figure 2.12: Illustration of the piezoelectric effect in transmitting and receiving modes. The figure shows voltage generation in response to applied mechanical stress (receiving mode) and mechanical deformation generated by an applied voltage (transmitting mode) [38].

The performance of the transducer is governed by several interrelated parameters, including resonance frequency, bandwidth, and energy transfer efficiency. The resonance frequency defines the frequency at which the piezoelectric element most efficiently converts electrical energy into mechanical vibrations. Operating near this frequency enables strong signal generation and improved sensitivity. The bandwidth determines the range of frequencies over which the transducer operates effectively and directly influences temporal resolution, as discussed in the previous section. A wide bandwidth allows the generation of short pulses and improves the ability to resolve closely spaced interfaces.

In addition, the efficiency of energy transfer into the medium depends strongly on acoustic impedance matching between the transducer and the surrounding materials. These characteristics are controlled by the internal structure of the transducer, including the piezoelectric element, backing material, and intermediate layers. Consequently, careful design of these components is required to achieve an optimal balance between signal strength, resolution, and penetration depth.

2.9.2 Piezoelectric Element Design

The piezoelectric element is the active component responsible for both the generation and detection of ultrasonic waves [4, 37]. Its performance depends on the selected material and its geometric dimensions. The thickness of the element primarily determines the resonance frequency. For thickness-mode operation, the resonance frequency is approximately inversely proportional to the element thickness, meaning that thinner elements operate at higher frequencies.

Material selection influences electromechanical coupling efficiency, acoustic impedance, and bandwidth [4, 37]. Piezoelectric ceramics such as PZT are commonly used due to their high sensitivity and efficient energy conversion. In addition, different element configurations, such as single-element or dual-element designs, can be used depending on the specific measurement requirements.

2.9.3 Backing Material Design

The backing material is located behind the piezoelectric element and plays a key role in shaping the temporal response of the transducer [4, 37]. Its primary function is to damp the vibrations of the piezoelectric element after excitation, thereby reducing ringing and shortening the emitted pulse. This improves temporal resolution and facilitates the separation of closely spaced echoes. A highly attenuating backing material produces strong damping, leading to shorter pulses and broader bandwidth, but may reduce the transmitted signal amplitude. Conversely, weaker damping increases signal amplitude but prolongs ringing and narrows the bandwidth. The selection of the backing material therefore requires a careful balance between pulse duration, bandwidth, and transmitted energy.

2.9.4 Acoustic Coupling Conditions

Efficient transmission of ultrasound requires proper acoustic coupling between the transducer and the medium [4, 37]. Due to the very low acoustic impedance of air, even small air gaps can result in almost complete reflection of the transmitted wave and severe signal loss [40].

To overcome this limitation, coupling media such as water or gel are commonly used [40]. These materials eliminate air gaps and provide stable transmission conditions with relatively low attenuation. Water is particularly suitable for controlled experimental setups due to its well-characterized acoustic properties. Alternatively, direct contact between the transducer and the sample may be used. While this approach simplifies the setup and can improve signal amplitude, it introduces additional uncertainties. Variations in applied pressure can compress soft tissue layers, altering their thickness, while small angular misalignments can affect the propagation path. Furthermore, changes in contact conditions may influence the effective acoustic impedance at the interface.

2.9.5 Acoustic Impedance Mismatch and Matching Layers

Even with proper coupling, a significant acoustic impedance mismatch exists between the piezoelectric transducer and biological tissue [4, 37]. This mismatch leads to strong reflections at the interface and reduces the amount of acoustic energy transmitted into the medium. To mitigate this effect, matching layers are introduced between the transducer and the tissue to create a gradual transition in acoustic impedance.

A common approach is the use of a quarter-wavelength matching layer [4]. In this configuration, the layer thickness is selected such that reflections from its boundaries interfere destructively, thereby minimizing reflection and maximizing transmission at a specific frequency. However, this condition is frequency-dependent and is therefore most effective for narrowband signals. For broadband applications, multiple matching layers can be employed [41]. By gradually varying the acoustic impedance across several layers, energy transmission can be improved over a wider frequency range, preserving signal strength across the bandwidth.

2.9.6 Buffer Rods and Delay Lines

In pulse-echo measurements, temporal separation between transmitted signals and received echoes is essential [4, 37]. Buffer rods are therefore introduced between the transducer and the medium to create a controlled time delay. This delay prevents overlap between the transmitted pulse and early reflections, enabling clear identification of interfaces such as the front-wall and back-wall echoes.

In addition to improving temporal separation, buffer rods can provide mechanical protection and enhance system stability. However, they also introduce additional interfaces within the system, which may generate internal reflections. These reflections must be considered during signal interpretation. Consequently, the material properties and geometry of the buffer rod must be carefully selected to ensure reliable measurement performance.

2.10 Ultrasound in Medical Applications

Having established how ultrasonic waves are generated, controlled, and coupled into a medium through transducer design, their practical relevance becomes evident in medical applications.

2.10.1 Advantages of Ultrasound Imaging

Ultrasound is widely used in clinical practice due to its ability to provide non-invasive imaging of internal anatomical structures [4]. Unlike ionizing imaging modalities such as X-ray or CT, ultrasound does not expose patients to radiation, making it a safe technique for repeated use. This is particularly important in clinical scenarios requiring continuous monitoring or follow-up examinations. In addition, ultrasound imaging can be performed in real time, allowing clinicians to observe dynamic processes such as blood flow, organ motion, and responses to interventions as they occur.

2.10.2 Applications in Soft Tissue Imaging

The primary domain of ultrasound in medicine is soft tissue imaging [4]. Structures such as muscles, organs, and blood vessels can be visualized effectively due to their relatively low acoustic impedance differences and moderate attenuation properties.

These characteristics allow sufficient transmission of acoustic energy and the generation of detectable echoes from internal interfaces. As a result, ultrasound has become a standard imaging modality in applications such as abdominal imaging, cardiology, and obstetrics.

2.10.3 Limitations in Hard Tissue Imaging

In contrast, imaging of hard tissues such as bone presents significant challenges. The large acoustic impedance mismatch between soft tissue and bone leads to strong reflections at the interface, limiting the amount of energy that penetrates deeper into the structure. Furthermore, bone exhibits high absorption and scattering, which attenuate the transmitted wave and reduce the amplitude of signals originating from deeper regions [42]. Consequently, conventional ultrasound imaging is less effective for visualizing structures beyond or within bone, and specialized techniques or adapted system designs are often required.

2.11 Ultrasound Interaction with Biological Tissues

While the previous section highlighted the practical applications of ultrasound in medicine, the effectiveness of these applications depends fundamentally on how ultrasonic waves interact with biological tissues.

2.11.1 Ultrasound Propagation in Biological Tissues

While reflections at interfaces determine where echoes are generated, the propagation of ultrasound between these interfaces is equally important. As the wave travels through biological tissues, its behaviour is governed by the mechanical and structural properties of the medium [37, 38]. Variations in density, stiffness, and internal composition influence not only the propagation speed, but also how the wave is attenuated, scattered, and reflected during its path. As a result, the received signal is shaped both by the location of interfaces and by the cumulative changes the wave undergoes during propagation. Understanding these effects is essential for correctly interpreting ultrasonic measurements and for designing systems capable of distinguishing between different tissue layers, such as skin and bone in this study.

2.11.2 Attenuation Mechanisms in Tissue

As ultrasound propagates through tissue, its amplitude decreases due to attenuation [4]. This attenuation is primarily caused by two mechanisms: absorption and scattering. Absorption converts part of the acoustic energy into heat, while scattering redistributes energy in different directions due to microscopic variations within the tissue. Both effects increase with frequency, meaning that higher-frequency waves lose energy more rapidly as they propagate. This introduces an important trade-off in ultrasonic system design. Higher frequencies provide improved spatial resolution due to shorter wavelengths, but they also reduce penetration depth. Lower frequencies, in contrast, allow deeper penetration but at the cost of reduced resolution.

This trade-off is particularly relevant in the present study, where reflections from deeper interfaces, such as the back-wall of the bone layer, must remain detectable.

2.11.3 Ultrasound Propagation in the Skin Layer

In the temporal bone region, the first significant reflection occurs at the skin surface. Although skin has a complex layered structure, it can be approximated acoustically as soft tissue with relatively low acoustic impedance and moderate attenuation. Because the acoustic impedance mismatch between the transducer and the skin is small, only a limited portion of the wave is reflected, while most of the acoustic energy is transmitted into the tissue. Despite its relatively low amplitude, the skin front-wall echo plays a crucial role, as it provides a reference point for ToF measurements. Variations in skin thickness, whether due to anatomical differences or applied contact pressure, can shift the timing of this echo and must therefore be considered in the interpretation of the received signal.

2.11.4 Ultrasound Propagation in the Bone Layer

As the wave continues to propagate, it reaches the bone, where a strong reflection occurs at the interface between soft tissue and bone due to the large acoustic impedance mismatch. This interface typically produces the dominant echo in the received signal. However, for thickness estimation of the bone, it is also necessary to detect reflections from the back-wall of the bone. This is significantly more challenging, as the wave undergoes strong attenuation within the bone due to both absorption and scattering. These effects reduce the amplitude of the transmitted wave, making the back-wall echo weaker and more difficult to identify. Consequently, the ability to detect the back-wall reflection depends on a careful balance between sufficient transmitted energy and adequate resolution. This again highlights the importance of selecting appropriate operating frequency, excitation signal characteristics, and signal processing techniques to ensure reliable detection of relevant echoes.

2.12 Ultrasound Thickness Estimation

The propagation and interaction mechanisms described in the previous sections form the basis for ultrasonic thickness estimation. By analyzing the time delay between reflections from different interfaces, it becomes possible to quantify layer thickness, as described in the following section.

2.12.1 Pulse-echo Thickness Estimation Principle

The reflections generated at material interfaces, together with attenuation effects during propagation, form the basis for estimating the thickness of biological structures (Figure 2.13) [4, 37]. By analyzing the timing of these echoes, it is possible to relate the received signal directly to the geometry of the medium. Specifically, ultrasound enables thickness estimation of layered materials by measuring the time delay between a transmitted pulse and echoes reflected from internal interfaces. This

approach, known as the pulse-echo technique, is widely used in both medical ultrasound and non-destructive testing, and forms the foundation of the measurement method proposed in this work.

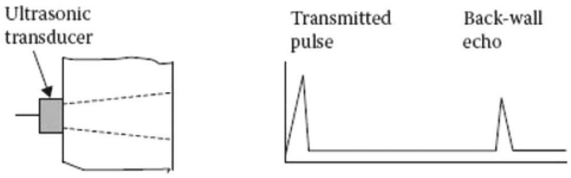

Figure 2.13: Principle of pulse-echo thickness estimation using normally incident longitudinal ultrasonic waves. (Adapted from: Ultrasonics, 4th Edition by Leonard Bond, Copyright © 2024 by CRC Press. Reproduced by permission of Taylor & Francis Group.)

In the context of this study, the received signal contains multiple echoes corresponding to different interfaces. The first significant echo is generated at the skin front-wall, followed by reflections from the soft tissue–bone boundary and the back-wall of the bone. The time differences between these echoes contain the information required to determine the thickness of the individual layers. To extract this information, a quantitative relationship between propagation time and distance is required.

2.12.2 Time-of-flight Thickness Calculation

The thickness of a layer can be determined using the ToF of the ultrasonic pulse, which represents the time required for the wave to travel from the transducer to an interface and back [4]. When the speed of sound in the material, c, is known, the thickness d can be calculated from the measured time delay as

$$d = \frac{c\,\Delta t}{2}, \tag{2.4}$$

where Δt_{echo} is the time difference between the relevant echoes. The factor of two accounts for the round-trip propagation of the wave between the transducer and the interface. Therefore, accurate determination of thickness depends on precise identification of these echoes in the received signal.

In this work, the skin thickness is determined from the time difference between the front-wall echo at the skin surface and the reflection from the skin–bone interface, which represents the back-wall of the skin layer. Similarly, the bone thickness is determined from the time difference between the reflection at the skin–bone interface, acting as the front-wall of the bone, and the echo from the back-wall of the bone. Accurate detection of these echoes is essential, as errors in their identification directly translate into errors in the calculated thickness. In particular, the back-wall echo of the bone may be weak due to strong attenuation within the bone, making it more challenging to detect compared to the front-wall reflections.

2.12.3 Factors Affecting Accuracy

The accuracy of this method depends on several factors. The speed of sound must be known with sufficient precision, as uncertainties in this parameter directly affect

the thickness calculation. In addition, the echoes must be clearly distinguishable and well separated in time, which requires an adequate SNR. Attenuation, especially within bone, can further reduce the amplitude of deeper echoes and complicate their detection.

These considerations highlight that the accurate determination of thickness depends not only on the mathematical relationship between time and distance, but also on the overall quality of the measured signal and the effectiveness of the chosen excitation and processing strategies.

3 Methods

This chapter describes the methodology used to design, simulate, and evaluate the ultrasound system developed in this project. The workflow consisted of analytical modelling, numerical simulation, transducer design, and experimental validation through measurements.

3.1 Analytical Modelling

An analytical model was developed to describe ultrasonic wave propagation through the multilayer structure consisting of the piezoelectric transducer, a single buffer rod, skin, and bone. The modelling workflow followed a sequential physics-based approach. First, the mechanical properties of each material were defined and used to derive the corresponding acoustic characteristics. These properties were then used to determine the reflection and transmission behavior at each interface. Based on the propagation velocities and layer thicknesses, the forward travel time and the echo arrival times from the relevant interfaces were determined. These timing quantities were subsequently used to derive the temporal resolution requirements for distinguishing echoes originating from skin and bone. Finally, the achievable axial resolution was evaluated from the pulse duration and excitation waveform parameters, and the transducer together with the buffer rod geometry was designed to maximize acoustic transmission and echo detectability.

3.1.1 Assumptions

To simplify the analytical formulation, the following assumptions were adopted:

- All materials were assumed to be homogeneous, isotropic, and linearly elastic.
- Acoustic propagation was modeled as longitudinal plane waves traveling perpendicular to the interfaces.
- Interfaces between adjacent layers were assumed to be perfectly planar and mechanically bonded.
- Acoustic attenuation, mode conversion, and scattering within the materials were neglected.
- Skin and bone were modeled as uniform layers with constant acoustic properties.

Under these assumptions, wave propagation can be treated as a one-dimensional problem along the axial direction of the transducer. Perfect bonding at the interfaces ensures continuity of acoustic pressure and particle velocity across layer boundaries. Neglecting attenuation and scattering allows the model to focus on first-order propagation behaviour and timing characteristics.

3.1.2 Acoustic Wave Propagation

Acoustic wave propagation in an elastic medium is governed by the three-dimensional wave equation, which describes the spatial and temporal evolution of the displacement field $u(\mathbf{r}, t)$. In its general form, it can be written as

$$\nabla^2 u(\mathbf{r}, t) = \frac{1}{c^2} \frac{\partial^2 u(\mathbf{r}, t)}{\partial t^2} \tag{3.1}$$

where c is the longitudinal wave velocity in the medium. Since the present analytical model assumes longitudinal plane waves propagating normal to the layer interfaces, the problem can be simplified to one spatial dimension along the axial direction of the transducer. Under this assumption, the wave equation reduces to

$$\frac{\partial^2 u(x, t)}{\partial x^2} = \frac{1}{c^2} \frac{\partial^2 u(x, t)}{\partial t^2} \tag{3.2}$$

The general solution of the one-dimensional wave equation is given by d'Alembert's solution,

$$u(x, t) = f(x - ct) + g(x + ct), \tag{3.3}$$

which represents the superposition of a forward-propagating wave $f(x - ct)$ and a backward-propagating wave $g(x+ct)$. In the present context, the forward component describes the transmitted wave travelling through the layered structure, while the backward component represents waves reflected at the interfaces between materials.

3.1.3 Mechanical and Acoustic Properties

The acoustic response of each layer depends on its mechanical properties. For each material included in the model, the density ρ, Young's modulus E, and Poisson's ratio ν were defined based on values reported in the literature. These parameters were used as the starting point for deriving the remaining mechanical and acoustic quantities required in the analytical model.

From E and ν, two additional elastic constants were determined: the bulk modulus K, which describes the resistance of a material to volumetric compression, and the shear modulus G, which characterizes its resistance to shear deformation. These quantities were calculated as

$$K = \frac{E}{3(1 - 2\nu)} \tag{3.4}$$

and

$$G = \frac{E}{2(1 + \nu)} \tag{3.5}$$

respectively.

Once the elastic moduli and density are known, the longitudinal wave velocity in the material can be evaluated from

$$c = \sqrt{\frac{K + \frac{4}{3}G}{\rho}}. \tag{3.6}$$

This expression was used for the solid layers in the model. For skin, experimentally reported values of longitudinal wave velocity were used directly.

The wavelength of the ultrasonic wave in each material depends on the propagation velocity in that medium and on the operating frequency of the transducer. Once the longitudinal wave velocity has been determined, the wavelength can be calculated using equation 2.1 with the operating frequency of the piezoelectric transducer, f_0. Since the wave velocity varies from one material to another, the wavelength also changes across the different layers of the multilayer structure.

When the density and longitudinal wave velocity are known, the acoustic impedance of the material can be evaluated from equation 2.2. Acoustic impedance is a key parameter in layered acoustic systems because it governs the partition of wave energy at the interface between two media.

3.1.3.1 Biological Tissue Modelling

The mechanical modelling of biological tissues in the temporal bone region is challenging due to the inherent variability and heterogeneous structure of cranial anatomy. Both skin and cortical bone exhibit spatially dependent mechanical behaviour influenced by anatomical location, physiological conditions, and measurement methodology.

Several studies have addressed the characterization of cranial tissues from complementary perspectives, including temporal bone thickness evaluation for implant design, macroscopic mechanical testing of cranial bone samples, and whole-head finite element models developed for BC wave propagation [43–45]. These studies collectively highlight the variability of reported material properties and the importance of selecting representative values consistent with cranial wave transmission behaviour.

In the present work, the material properties for skin and cortical bone were selected from a validated finite element head model specifically developed for bone conducted sound transmission [46]. The selected dataset was chosen due to its direct relevance to cranial wave propagation and its validation against experimental observations. The adopted values were further verified to lie within the range reported in the literature, ensuring consistency with previously published cranial bone mechanics data.

3.1.3.2 Choice of Piezoelectric and Buffer Rod Materials

PZT was selected as the piezoelectric material due to its high electromechanical coupling efficiency and well-established use in ultrasonic transducer design. Its high acoustic impedance enables efficient conversion of electrical energy into mechanical vibrations, while its resonance behaviour allows precise frequency control through geometric tuning.

Polymethyl methacrylate (PMMA) was selected as the buffer rod material due to its favourable acoustic and mechanical properties. Its intermediate acoustic impedance improves energy transfer between the transducer and biological tissue, while its structural stability and machinability make it suitable for precise geometric implementation. In addition, PMMA supports the realization of a quarter-wavelength thickness design, which is beneficial for optimizing wave transmission.

3.1.4 Reflection and Transmission at Interfaces

The acoustic impedances of adjacent layers were used to evaluate wave behaviour at each interface. For an incident wave propagating from medium 1 to medium 2, the pressure reflection coefficient was calculated from equation 2.3 and the transmission coefficient as

$$T = \frac{2Z_2}{Z_2 + Z_1}. \tag{3.7}$$

These coefficients were used to evaluate the fraction of the incident wave amplitude reflected at each interface and the fraction transmitted further through the layered structure.

3.1.5 Timing and Pulse Parameters

The propagation time through the different layers is of central importance because the measured echo delays form the basis for determining the thickness of the skin and bone layers.

For a wave traveling through a layer of thickness d with longitudinal velocity c, the one-way travel time is given by

$$t = \frac{d}{c}. \tag{3.8}$$

However, the experimentally measured signal corresponds to an echo returning to the transducer after reflection at an interface. For this reason, the relevant quantity is the round-trip travel time, which can be written as

$$t_{echo} = \frac{2d}{c}. \tag{3.9}$$

This expression constitutes the basis of the ToF approach used in this work to determine skin and bone thickness from ultrasonic measurements.

The latest expected echo determines the minimum acquisition window required to capture all relevant reflections without overlap, defined as $t_{window} = t_{echo,total}$.

To prevent ambiguity between successive emitted pulses, the pulse repetition frequency (PRF) must be chosen such that a new pulse is not transmitted before all relevant echoes from the previous pulse have returned. The corresponding PRF is therefore given by

$$PRF = \frac{1}{t_{window}}. \tag{3.10}$$

The temporal duration of the transmitted ultrasonic pulse depends on the number of excitation cycles used to drive the transducer. For an excitation burst consisting of N_{cycles} cycles, the pulse duration was expressed as

$$t_{exc} = \frac{N_{cycles}}{f_0}. \tag{3.11}$$

3.1.6 Resolution Analysis

The ability of the system to distinguish between echoes originating from closely spaced interfaces depends on the spatial extent of the transmitted ultrasonic pulse. This is commonly described by the spatial pulse length (SPL), which represents the physical length occupied by the pulse as it propagates through a given medium.

The SPL is determined by the number of excitation cycles and the wavelength in the propagation medium, and can be expressed as

$$SPL = ct_{exc} = N_{cycles}\lambda, \tag{3.12}$$

where λ is the wavelength in the propagation medium. Since a shorter pulse occupies a smaller spatial region, reducing the SPL length improves the ability of the system to separate echoes returning from nearby interfaces.

Based on this relation, the axial resolution is commonly approximated as half the SPL,

$$R_{axial} = \frac{SPL}{2}. \tag{3.13}$$

The axial resolution therefore represents the minimum separation along the propagation direction for which two reflecting interfaces can still be identified as distinct echoes in the received signal.

In the present application, axial resolution is a key design parameter because the measurement system is intended to determine both skin and bone thickness in the temporal bone region. From a practical point of view, the required resolution is linked to the dimensional increments relevant for the surgical components. The derived axial resolution was compared with the expected interface separations in skin and bone to evaluate whether distinct reflections could be resolved. For skin thickness assessment, a resolution on the order of 1.5 mm was considered sufficient, since common abutment lengths are available in discrete steps of 6, 9, 12, and 14 mm. For bone thickness assessment, a finer resolution of 1 mm was targeted, as implant lengths differ by only 1 mm, between 3 and 4 mm. The analytical derivation of SPL and axial resolution was therefore used to evaluate whether the selected transducer frequency and pulse characteristics were compatible with these measurement requirements.

In addition to axial resolution, the temporal separation between echoes from the skin and bone interfaces also affects the practical detectability of the corresponding reflections. For this reason, both pulse length and ToF differences were considered when assessing the feasibility of the determination of thickness.

3.1.7 Transducer Design

The acoustic properties derived in the previous steps were then used to define the main geometric parameters of the ultrasonic transducer. In particular, the dimensions and materials of the piezoelectric element and the matching layer were selected to ensure efficient generation and transmission of ultrasonic waves toward the biological tissues of interest.

The thickness of the piezoelectric element was chosen to satisfy the thickness resonance condition. Under this operating mode, the piezoelectric layer resonates when its thickness is equal to half the acoustic wavelength in the material. The required piezoelectric thickness can therefore be expressed as

$$d_P = \frac{c_P}{2f_0}, \tag{3.14}$$

where c_P is the longitudinal wave velocity in the piezoelectric material.

After defining the piezoelectric thickness from the thickness resonance condition, the front matching structure was designed to improve acoustic transmission from the high-impedance piezoelectric element to the much lower impedance biological tissue. A single buffer rod was introduced between the transducer and the tissue interface to guide the ultrasonic wave and improve mechanical coupling. The thickness of the matching layer was determined according to the quarter-wavelength principle. The thickness was chosen as an odd multiple of one quarter of the wavelength in the corresponding material,

$$d_{BR} = (2n-1)\frac{\lambda}{4}, \tag{3.15}$$

where n is an integer defining the selected odd multiple. This criterion was used to determine the thickness of the buffer rod.

Once the matching layer thickness was established, the diameter of the piezoelectric element was derived based on the diffraction criterion. In order to maintain a relatively concentrated acoustic field throughout the matching structure, the near-field length was chosen to be approximately equal to the total thickness of the matching layer. The near-field length N of a circular transducer is given by

$$N = \frac{D_P^2}{4\lambda_{BR}}, \tag{3.16}$$

where D_P is the transducer diameter and λ_{BR} is the wavelength in the buffer rod layer. By imposing the condition that the near-field length should match the total buffer rod thickness, that is, $N \approx d_{BR}$, the transducer diameter can be evaluated by rearranging the previous expression as

$$D_P = \sqrt{4\lambda_{BR} d_{BR}}, \tag{3.17}$$

where d_{BR} is the total thickness of the buffer rod structure. This design choice ensures that the acoustic beam remains in the near field over approximately the entire

length of the buffer rod, thereby limiting beam divergence before the wave reaches the tissue interface.

3.2 Numerical Simulation

Following the analytical design phase, numerical simulations were carried out to study the transient response of the ultrasonic transducer and to investigate how the generated wave propagates through the different intermediate layers before reaching the bone interface. The numerical model was primarily used to evaluate the influence of excitation frequency, waveform shape, and tissue thickness on the received US signal, as well as to support the resolution and penetration depth analysis discussed in the following sections.

All simulations were implemented in COMSOL Multiphysics® version 6.4 using a time-dependent multiphysics model. The excitation signals were generated and normalized in MATLAB R2024b and then imported into COMSOL.

3.2.1 Simulation Model

The numerical model was constructed to reproduce the complete ultrasonic propagation path, starting from the transducer and extending through the biological layers of interest. The geometry included the backing layer, the piezoelectric element, the buffer rod, the skin layer, and the temporal bone. Particular attention was given to preserving consistency with the dimensions obtained from the analytical model, so that the numerical simulations could directly validate the theoretical evaluations. At the same time, the tissue layers were introduced as variable geometric parameters in order to allow systematic investigation of thickness-related effects.

From a physics perspective, the model combines electrical, structural, and acoustic domains. The electrical excitation of the piezoelectric element was described using the electrostatics interface, while the mechanical response of the backing, piezoelectric material, buffer rod, and bone layers was modeled through solid mechanics. Since wave propagation in the skin layer is better described as an acoustic pressure field, this region was assigned to the pressure acoustics interface. The coupling between the electrical and mechanical behaviour of the piezoelectric element was introduced through the piezoelectricity multiphysics interface, allowing direct conversion of the applied voltage excitation into structural vibration and subsequent wave transmission.

3.2.2 Material Properties

The material properties assigned to each domain were selected according to literature values and manufacturer specifications. For the solid layers, namely backing, buffer rod, and bone, the material definition included density, Young's modulus, and Poisson's ratio, which are the fundamental parameters governing elastic wave propagation in the structural domain. For the skin layer, the acoustic behaviour

was described using density and speed of sound, which directly determine wave velocity and acoustic impedance. A more detailed material description was required for the piezoelectric element. In this case, the model included density, compliance matrix in Voigt notation, electromechanical coupling matrix in Voigt notation, and relative permittivity matrix. This complete constitutive definition was necessary to accurately reproduce the electromechanical conversion process.

3.2.3 Boundary Conditions

Since the geometry of the transducer assembly is symmetric with respect to its central axis, only one half of the domain was considered in the simulations. This choice significantly reduced the computational cost without affecting the physical accuracy of the results. A symmetry boundary condition was therefore applied along the longitudinal axis of the model.

At each interface between adjacent solid layers, continuity conditions ensured proper transmission of displacement and stress, allowing the ultrasonic wave to propagate through the layered structure without artificial discontinuities. At the transition between the buffer rod and the skin layer, acoustic-structure coupling was imposed to describe the transfer of energy from the solid domain into the acoustic medium.

The electrical excitation was introduced through a terminal-type circuit boundary condition applied to the piezoelectric element. This included the definition of a voltage source, ground node, resistor, and external terminal.

In order to evaluate the received signal, a boundary probe was positioned at the interface between the piezoelectric element and the buffer rod. This location was selected to capture the raw ultrasound signal returning to the transducer after reflection from the different interfaces.

3.2.4 Excitation

A central part of the numerical investigation was the study of different excitation strategies. The excitation frequency was varied between 2 MHz and 8 MHz in order to analyse the trade-off between penetration depth and axial resolution. In addition to the frequency sweep, three different waveform shapes were considered, namely pulse, sine burst, and chirp excitation. This comparison was introduced to evaluate how the temporal structure of the input signal affects the transmitted energy and the quality of the received echoes. Each waveform was first generated in MATLAB by defining the required centre frequency and temporal duration. Before importing the signals into COMSOL, tapering windows were applied to smooth the waveform edges and reduce numerical artifacts caused by abrupt discontinuities. For the sine burst and chirp signals, a Tukey window was used, while the pulse excitation was tapered using a Hanning window (Figure A.1, A.2 in Appendix A). This preprocessing stage was particularly important for the transient simulations, as it improved spectral behaviour and reduced undesired high-frequency components.

3.2.5 Mesh

The computational domain was discretized using a free quadrilateral mesh. The mesh density was selected based on the wavelength in the piezoelectric material, with the maximum element size imposed as

$$h_{\max} = \frac{\lambda_P}{10}, \tag{3.18}$$

where λ_P is the wavelength in the piezoelectric material. This criterion ensured that the propagating ultrasonic wave was sufficiently resolved throughout the geometry, especially in the higher-frequency simulations where the wavelength becomes significantly smaller.

3.2.6 Study

The transient behaviour of the system was analysed using a time-dependent study. The temporal discretization was chosen as

$$\Delta t = \frac{1}{60 f_0}, \tag{3.19}$$

where f_0 is the centre frequency of the excitation. This time step was selected to ensure sufficiently dense sampling of the ultrasonic waveform in the time domain and to accurately capture the arrival time of the reflected echoes. Beyond the transient response itself, parametric studies were performed to investigate the influence of tissue thickness.

3.2.7 Simulation Approach

Once the numerical model and solver settings were established, the simulation approach was structured as a sequence of targeted studies to systematically investigate the influence of key parameters on the received ultrasonic signal.

First, a reference simulation was defined to serve as a baseline for all subsequent analyses. This configuration employed a centre frequency of 5 MHz with a skin thickness of 5 mm and a bone thickness of 10 mm. The reference case was used to verify model behaviour and to tune transducer parameters.

Next, an excitation study was performed to compare different waveform types, including pulse, sine burst, and chirp excitation. These signals were evaluated at discrete frequencies of 2 MHz, 4 MHz, and 8 MHz in order to assess their influence on transmitted energy, echo amplitude, and temporal resolution.

Following this, a more detailed frequency sweep was conducted for pulse and chirp excitation. The frequency range between 2 MHz and 8 MHz was investigated to better understand the trade-off between penetration depth and axial resolution, and to identify an optimal operating range for the application.

To evaluate the sensitivity of the system to anatomical variability, separate parametric studies were performed for bone and skin thickness. In the bone thickness study, the bone layer was varied while maintaining a constant skin thickness of 5 mm. Conversely, in the skin thickness study, the skin layer was varied while keeping the bone thickness fixed at 10 mm. These analyses enabled independent assessment of the influence of each layer on attenuation, echo timing, and signal amplitude. In addition, the worst-case scenario was considered. In this configuration, both the skin and bone thicknesses were reduced to 3 mm.

Finally, a simulation scenario incorporating a blood vessel structure was introduced to examine its impact on wave propagation, echo characteristics, and signal interpretation within the multilayer tissue model. Two idealized vessel geometries were investigated to represent different orientations with respect to the tissue layers, where a circular cross-section was used to model vessels oriented perpendicular to the layered structure, while a rectangular geometry was adopted to approximate vessels aligned parallel to the tissue interfaces.

3.2.8 Simulation Outputs

The primary output of the simulations was the raw ultrasound signal measured at the piezoelectric–buffer rod interface. This signal was then used for post-processing and comparison between the different excitation frequencies, waveform types, and tissue thickness configurations. Particular focus was placed on echo amplitude, ToF, and axial resolution, as these parameters directly support the assessment of imaging performance.

3.3 Post-processing algorithm

Following the numerical simulations performed in COMSOL, the resulting ultrasound signals were exported and post-processed in MATLAB. The workflow was structured into four main stages: signal extraction, signal processing, feature extraction, and evaluation metric analysis.

3.3.1 Signal Extraction

The raw ultrasound signal was defined as the voltage measured at the interface between the piezoelectric element and the buffer rod. This signal contains both the transmitted excitation and the subsequent reflections generated at material interfaces within the multilayer structure. To ensure that only physically meaningful reflections were considered, the signal was truncated by discarding the initial portion up to 5 μs. This choice is supported by the analytical derivation of the minimum round-trip propagation time within the system, ensuring that early-time components, primarily associated with excitation artifacts and numerical transients, are excluded from the analysis.

3.3.2 Signal Processing

The signal processing stage was adapted depending on the excitation type. For chirp excitations, the received signal was cross-correlated with the transmitted waveform. This operation acts as a matched filter, leading to temporal compression of the broadband signal and an improvement in SNR, in agreement with analytical predictions. For pulse and sine burst excitations, the received signal was directly used without additional correlation, as these excitation types inherently produce temporally localized responses.

The analytic signal was computed using the Hilbert transform, and its magnitude was taken to obtain the signal envelope. This transformation suppresses high-frequency oscillations while preserving the amplitude modulation associated with echo arrivals, thereby facilitating a more robust identification of reflection events.

3.3.3 Feature Extraction

Peak detection was performed on the envelope signal using a constrained approach (Figure 3.1). A minimum peak distance of 2 μs was imposed, based on the analytically derived ToF separation between consecutive reflections from adjacent interfaces. This ensures that each detected peak corresponds to a distinct physical echo and prevents multiple detections of the same reflection. In addition, minimum peak prominence and height thresholds were set to 5 % of the maximum envelope amplitude. This relative thresholding is consistent with the analytical expectation of amplitude decay due to attenuation and acoustic impedance mismatches, allowing weaker but physically meaningful reflections to be identified while suppressing noise-induced fluctuations.

For each detected peak, a set of characteristic metrics was extracted in order to quantitatively describe the signal and evaluate the performance of the different excitation strategies (Figure 3.1). These metrics were selected based on their direct physical interpretation and their relevance to the analytical model of ultrasonic wave propagation.

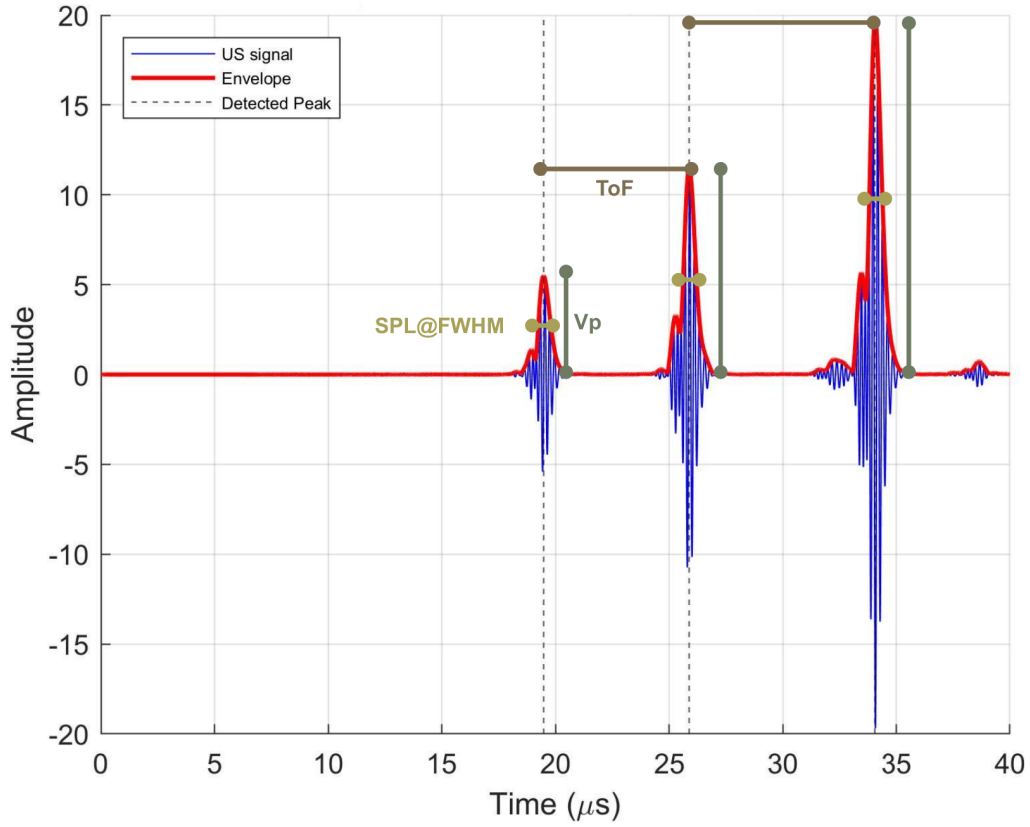

Figure 3.1: Example of ultrasound signal processing and feature extraction used for quantitative ultrasound analysis. The plot illustrates the normalized amplitude of the raw ultrasound signal (continuous blue line), its corresponding amplitude envelope (continuous red line), and the detected peaks (dashed black lines). Key features are extracted from the envelope, including the peak voltage (V_p), the spatial pulse length at full width at half maximum (SPL@FWHM), and the ToF between successive reflections.

3.3.3.1 Voltage Peak

The first metric is the peak voltage, defined as

$$V_P = \max |V(t)|, \tag{3.20}$$

which represents the maximum amplitude of the received echo (Figure 3.1). Physically, V_P provides a measure of the strength of the ultrasonic reflection. A higher peak voltage indicates more efficient transmission through the multilayer structure, as well as lower attenuation and reflection losses at the interfaces. This metric is therefore essential for assessing the detectability of echoes and the overall signal quality.

3.3.3.2 Spatial Pulse Length at the Full Width at Half Maximum

The second metric is the SPL evaluated at the full width at half maximum (SPL@FWHM) (Figure 3.1). This quantity is derived from the temporal extent of the peak and is defined as

$$\text{SPL@FWHM} = t^{II} - t^{I}, \quad \text{with} \quad V(t^{I}) = V(t^{II}) = \frac{V_P}{2} \tag{3.21}$$

where t^I and t^{II} denote the time instants at which the signal amplitude reaches half of the peak value. This metric characterizes the temporal width of the echo and provides insight into pulse distortion effects. A larger width indicates pulse broadening, which may arise from dispersion, scattering, or multiple reflections within the layered structure. From a practical perspective, SPL@FWHM is directly related to the achievable temporal resolution, as narrower pulses enable a clearer separation between closely spaced echoes.

3.3.3.3 Time-of-flight

The third and most critical metric is the ToF, computed as

$$\mathrm{ToF} = t_P^{(n+1)} - t_P^{(n)}, \tag{3.22}$$

where $t_P^{(n)}$ and $t_P^{(n+1)}$ represent the temporal positions of two consecutive peaks (Figure 3.1). The ToF corresponds to the propagation time of the ultrasonic wave between two reflection events and is directly linked to the thickness of the intermediate layer and the acoustic velocity of the material. As such, this metric constitutes the primary observable for the determination of thickness.

3.3.3.4 Selection Criteria for Excitation and Frequency

The selection of the most suitable excitation and frequency range was guided by a combined analysis of these metrics. In particular, high peak amplitudes were preferred to ensure strong and detectable echoes, while small relative variations between peak amplitudes were considered indicative of stable signal transmission across interfaces. At the same time, narrow pulse widths were favoured, as they correspond to improved temporal resolution and reduced overlap between adjacent echoes.

Despite the importance of amplitude and pulse width, the ToF remains the dominant performance metric in this study, as it directly influence the accuracy of the determined thickness. Consequently, the evaluation of excitation strategies prioritizes configurations that minimize ToF error while maintaining sufficient signal amplitude and temporal resolution.

3.3.4 Evaluation Metric Analysis

To enable a consistent comparison across different excitation strategies, the extracted peak amplitudes and widths at half maximum were normalized with respect to their maximum values within each signal.

The accuracy of the ToF measurements was evaluated by computing the relative error with respect to the theoretical values obtained from the analytical model. This provides a quantitative measure of the deviation between simulated and expected propagation times.

Finally, the material thickness was determined from the measured ToF values, assuming a known speed of sound and a round-trip propagation path. The comparison

between the determined and nominal thickness values was used to assess the performance of the different excitation and signal processing approaches in terms of accuracy and robustness.

In this context, both the magnitude and the sign of the ToF errors were considered. While the magnitude of the error quantifies the overall accuracy, the sign provides insight into the nature of the deviation. In particular, a positive error indicates an overestimation of the thickness, whereas a negative error corresponds to an underestimation. This distinction is relevant for identifying systematic biases associated with specific excitation strategies or frequency ranges.

3.4 Ultrasonic Transducer Design and Experimental Setup

The results obtained from the analytical modelling and numerical simulations are used to define the design requirements for the ultrasonic transducer.

A central design parameter is the operating frequency, which governs the trade-off between penetration depth and spatial resolution. Accordingly, the operating frequency range is selected to ensure that reflections from both superficial structures and deeper interfaces can be adequately detected. In addition to frequency selection, the choice of excitation waveform constitutes another critical design consideration, since it determines the transmitted acoustic energy. The achievable system bandwidth and damping characteristics further influence the capability to resolve closely spaced reflectors, imposing design constraints on both the piezoelectric element and the backing material. Finally, acoustic impedance matching between the transducer and the propagation medium is addressed to maximize transmission efficiency.

A corresponding experimental setup was defined to support future implementation and validation of the method.

4 Results

This chapter presents the main results obtained throughout this thesis. To maintain clarity and avoid an overly extensive results section, only selected figures and results are included in the main text. Additional results, including supplementary figures, are provided in the Appendix.

4.1 Analytical Modelling Results

This section presents the results obtained from the analytical model described in Section 3.1. The analysis follows the same logical sequence as the model formulation, starting from the definition of material properties and progressing through wave propagation characteristics, interface behaviour, temporal response, resolution limits, and final transducer design parameters.

4.1.1 Material Properties and Derived Acoustic Quantities

The analytical model is initialized using the mechanical properties of the considered materials.

Table 4.1: Mechanical input parameters and derived acoustic properties used in the analytical model for the materials of interest: the piezoelectric element, the PMMA buffer rod, skin, and cortical bone.

Material	Density ρ (kg/m^3)	Young's modulus E (MPa)	Poisson's ratio ν	Wave velocity c (m/s)	Acoustic impedance Z (MRayl)	Wavelength λ (mm)
P	7500	64000	0.30	3389.27	25.42	0.68
BR	1190	3200	0.35	2077.45	2.47	0.42
S	900	-	-	1540.00	1.39	0.31
B	1800	8000	0.30	2446.00	4.40	0.49

Abbreviations: P = Piezoelectric element, BR = Buffer rod, S = Skin, B = Cortical bone.

The input parameters include density, Young's modulus, and Poisson's ratio, from which the acoustic quantities are derived, including wave velocity, acoustic impedance, and wavelength at the selected operating frequency of 5 MHz (Table 4.1). The acoustic impedance is highest for the piezoelectric element, reflecting its high density and stiffness, while the lowest impedance is observed in skin. The buffer rod and cortical bone exhibit intermediate impedance values. Similarly, at a constant frequency, the wavelength follows the same trend as the wave velocity. Accordingly, the piezoelectric material exhibits the largest wavelength, while skin has the shortest wavelength, with the buffer rod and cortical bone again taking intermediate values.

4.1.2 Interface Response: Reflection and Transmission

Using the acoustic impedance values reported in Table 4.1, the cumulative reflection and transmission coefficients were calculated for all relevant interfaces in the propagation path.

Table 4.2: Calculated cumulative reflection and transmission coefficients at material interfaces.

	Reflection R	Transmission T
P–BR	0.82	0.18
BR–S	0.05	0.13
S–B	0.07	0.06
B–D	0.05	0.01

Abbreviations: P = Piezoelectric element, BR = Buffer rod, S = Skin, B = Cortical bone, D = Dura mater. Interfaces are denoted by the materials on either side.

The results show that reflection is dependent on the degree of acoustic impedance mismatch between adjacent materials (Table 4.2). The highest reflection coefficient is observed at the P–BR interface, where the impedance difference is largest. Accordingly, transmission is reduced at interfaces with high acoustic impedance mismatch and remains relatively higher when the mismatch is small, as observed for the BR–S, S–B, and B–D interfaces.

4.1.3 Temporal Response and Echo Separation

The temporal behaviour of the system was evaluated using a ToF formulation based on the wave velocities of the individual layers. Since the propagation time is directly dependent on layer thickness, the analysis was performed for a range of representative skin and bone thickness values between 3 mm and 10 mm.

Table 4.3: Calculated round-trip travel times for varying layer thicknesses at material interfaces of interest.

Round-trip travel time (μs)								
	Thickness							
	3 mm	4 mm	5 mm	6 mm	7 mm	8 mm	9 mm	10 mm
S–B	6.58	7.88	9.18	10.48	11.78	13.08	14.38	15.67
B–D	9.04	11.15	13.27	15.39	17.50	19.62	21.73	23.85

Abbreviations: S = Skin, B = Cortical bone, D = Dura mater. Interfaces are denoted by the materials on either side.

For each configuration, the propagation times across the multilayer structure were computed, allowing estimation of both one-way and round-trip travel times (Table 4.3). The sequence of received echoes follows the order of the interfaces encountered by the propagating wave. The first detectable reflection originates from the BR–S interface, the second reflection is generated at the S–B boundary, and a third reflection is associated with the B–D interface. The BR–S reflection occurs at a

constant time delay of 2.69 μs, as it depends only on the fixed buffer rod thickness. In contrast, the round-trip travel time increases with layer thickness for both the S–B and B–D interfaces.

4.1.4 Resolution and System Constraints

The propagation times reported in Table 4.3 were used to define the required acquisition time window to capture the latest returning echo, as well as to derive the time resolution within the skin and bone layers for varying thicknesses.

Table 4.4: Time resolutions (μs) for varying layer thicknesses for skin and bone.

Time resolution (μs)								
	Thickness							
	3 mm	4 mm	5 mm	6 mm	7 mm	8 mm	9 mm	10 mm
S	3.90	5.19	6.49	7.79	9.09	10.39	11.69	12.99
B	2.45	3.27	4.09	4.91	5.72	6.54	7.36	8.18

Abbreviations: S = Skin, B = Cortical bone.

For both tissues, the travel time increases with layer thickness, reflecting the direct proportionality between propagation time and distance (Table 4.4). Moreover, the propagation time is consistently longer in skin than in bone for the same thickness, due to the lower wave velocity in soft tissue.

Table 4.5: Axial resolution for varying excitation frequencies for skin and bone layers.

Axial resolution (mm)							
	Frequency						
	2 MHz	3 MHz	4 MHz	5 MHz	6 MHz	7 MHz	8 MHz
S	2.31	1.54	1.16	0.92	0.77	0.66	0.58
B	3.67	2.45	1.83	1.47	1.22	1.05	0.92

Abbreviations: S = Skin, B = Cortical bone.

While the time resolution is governed by the echo arrival times, the axial resolution is primarily determined by the excitation frequency (Table 4.5). The results show that axial resolution is higher in the skin layer compared to bone, due to its shorter wavelength. In both materials, the axial resolution improves with increasing frequency, highlighting the trade-off between resolution and penetration depth in the system design.

4.1.5 Transducer and Buffer Rod Design Parameters

The final step of the analytical model consists in deriving the geometric parameters of the transducer system.

Table 4.6: Derived transducer and buffer rod geometric parameters (mm) for varying excitation frequencies.

Geometric transducer and buffer rod parameters (mm)							
	Frequency						
	2 MHz	3 MHz	4 MHz	5 MHz	6 MHz	7 MHz	8 MHz
d_{BR}	10.65	7.10	5.32	4.26	3.55	3.04	2.66
d_P	0.85	0.56	0.42	0.34	0.28	0.24	0.21
D_P	6.65	4.43	3.33	2.66	2.22	1.90	1.66

Abbreviations: d_{BR} = Thickness of buffer rod, d_P = Thickness of piezoelectric element, D_P = Diameter of piezoelectric element.

The buffer rod thickness decreases with increasing excitation frequency, but does not impose significant manufacturability constraints within the considered frequency range (Table 4.6). Similarly, both the piezoelectric element thickness and diameter decrease with frequency. These parameters were directly used as inputs for the numerical simulations described in Section 3.2.

4.2 Numerical Simulation Results

The numerical model described in Section 3.2 was used to analyse the transient response of the ultrasonic system and to quantify the influence of excitation waveform, frequency, and tissue geometry on the received ultrasound signal at the piezoelectric–buffer rod interface. The results are presented in terms of ultrasound signals, amplitude envelopes, ToF, and spatial pulse characteristics.

4.2.1 Simulation Setup

The simulations were performed using the multilayer configuration introduced in Section 3.2.1, representing the complete propagation path from the transducer to the bone interface. The model consists of the backing layer, piezoelectric element, buffer rod, skin layer, and temporal bone (Figure 4.1). Material properties and boundary conditions were defined as described in the numerical model, ensuring continuity of mechanical and acoustic fields across interfaces.

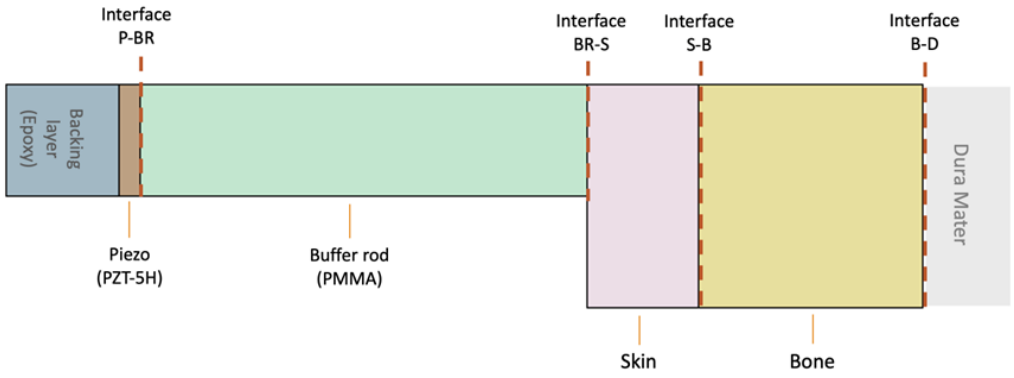

Figure 4.1: Schematic representation of the multilayer acoustic model used to interpret the measured ultrasound signals. Abbrevations: P=Piezo, BR=Buffer Rod, S=Skin, B=Bone, D=Dura Mater.

4.2.2 Influence of Excitation Waveform

Three excitation waveforms were applied to the piezoelectric element: pulse, sine burst, and chirp (Figure 4.2). The chirp and sine burst signals exhibit longer temporal durations compared to the pulse excitation. While the pulse and sine burst are narrowband signals centered at a single frequency, the chirp spans a broader frequency range.

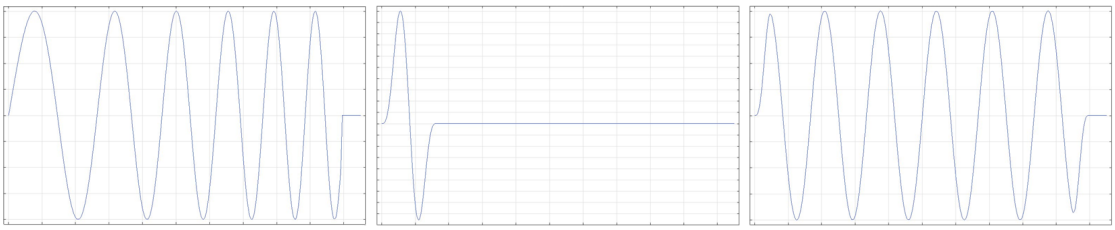

(a) Chirp excitation **(b)** Pulse excitation **(c)** Sine burst excitation

Figure 4.2: Temporal structures of excitation waveforms used for ultrasonic signal transmission: (a) chirp signal, (b) short pulse, and (c) sine burst.

The corresponding ultrasound signals, amplitude envelopes, and detected peaks were compared for excitation frequencies of 2, 4, and 8 MHz (Figures 4.3, 4.4 and Figures B.1, B.2, B.3 in Appendix B). For all excitation types and frequencies, the same sequence of reflections is observed, corresponding to the BR–S, S–B, and B–D interfaces.

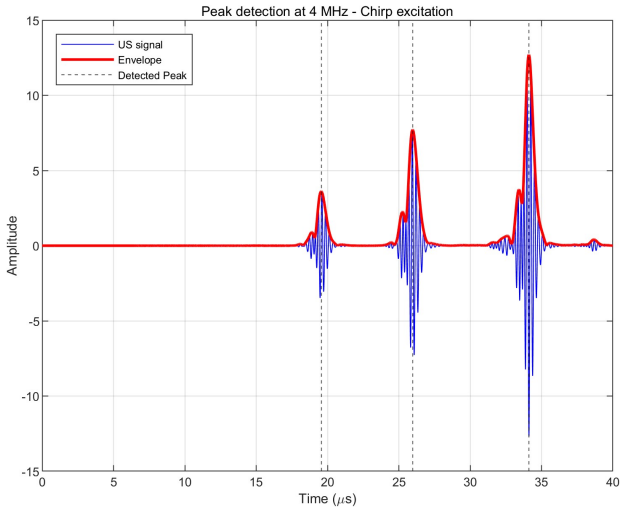

(a) Chirp excitation, 4 MHz

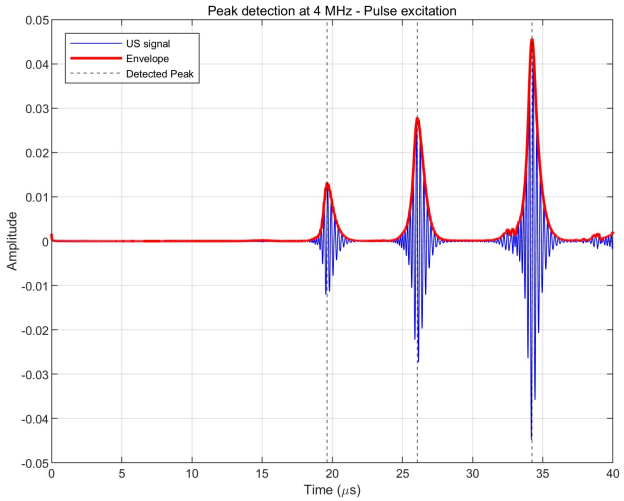

(b) Pulse excitation, 4 MHz

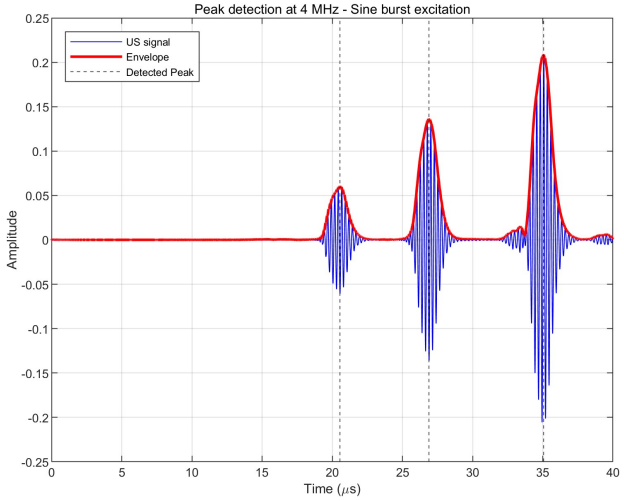

(c) Sine Burst excitation, 4 MHz

Figure 4.3: Comparison of raw ultrasound signals, amplitude envelopes, and detected peaks at 4 MHz for different excitations: (a) chirp, (b) pulse, and (c) sine burst.

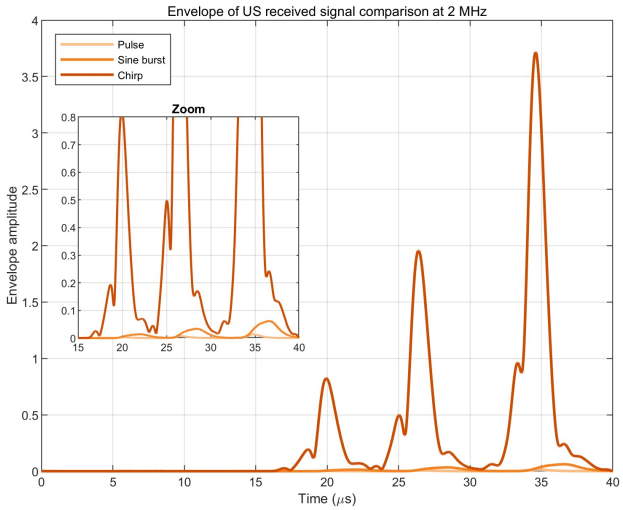

(a) 2 MHz

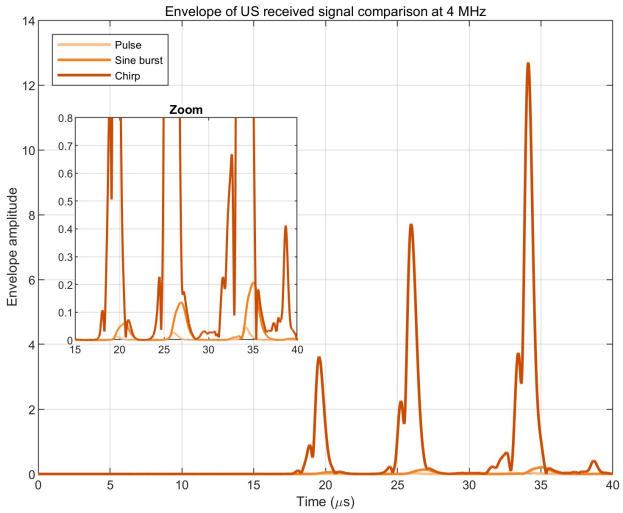

(b) 4 MHz

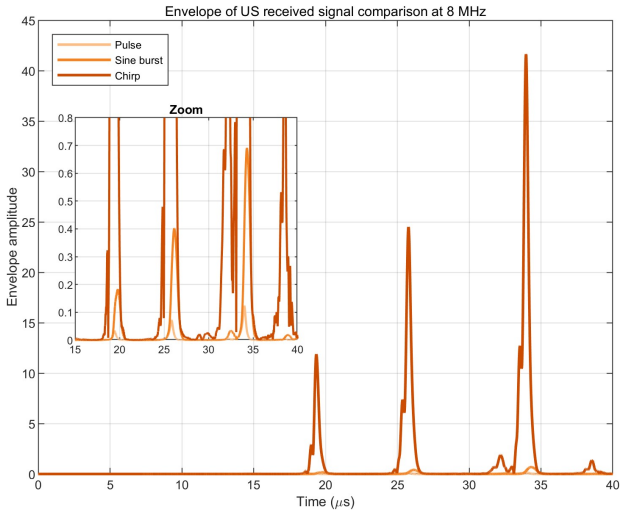

(c) 8 MHz

Figure 4.4: Comparison of received ultrasound signal envelopes for chirp, pulse, and sine burst excitations for different frequencies: (a) 2 MHz, (b) 4 MHz, and (c) 8 MHz.

Table 4.7: Voltage peaks (V) for varying excitation types and frequencies at material interfaces of interest.

	Voltage peaks (V)								
	Chirp			Pulse			Sine Burst		
	2 MHz	4 MHz	8 MHz	2 MHz	4 MHz	8 MHz	2 MHz	4 MHz	8 MHz
BR–S	0.825	3.623	11.891	0.003	0.013	0.035	0.014	0.061	0.184
S–B	1.956	7.717	24.503	0.007	0.028	0.073	0.034	0.136	0.402
B–D	3.716	12.698	41.642	0.014	0.046	0.124	0.062	0.209	0.692

Abbreviations: BR = Buffer rod, S = Skin, B = Cortical bone, D = Dura mater. Interfaces are denoted by the materials on either side.

A clear trend is observed in the amplitude of the received ultrasound signals (Table 4.7). At all interfaces and frequencies, the peak amplitude is consistently highest for chirp excitation, followed by sine burst and pulse excitation. In addition, for all excitation types, the peak amplitude increases with frequency, indicating enhanced signal strength at higher operating frequencies.

Table 4.8: SPL@FWHM (μs) for varying excitation types and frequencies at material interfaces of interest

	SPL@FWHM (μs)								
	Chirp			Pulse			Sine Burst		
	2 MHz	4 MHz	8 MHz	2 MHz	4 MHz	8 MHz	2 MHz	4 MHz	8 MHz
BR–S	1.373	0.669	0.336	1.475	0.732	0.356	2.910	1.442	0.724
S–B	1.400	0.731	0.378	1.594	0.847	0.404	2.992	1.485	0.735
B–D	1.395	0.668	0.379	1.601	0.756	0.405	3.004	1.480	0.727

Abbreviations: BR = Buffer rod, S = Skin, B = Cortical bone, D = Dura mater. Interfaces are denoted by the materials on either side.

In terms of temporal characteristics, chirp and pulse excitations generate more compact ultrasound responses, with sharper envelopes and better-defined peaks compared to sine burst excitation. This is reflected in the SPL@FWHM values (Table 4.8), where chirp and pulse consistently produce lower values than sine burst across all interfaces and frequencies. In contrast, sine burst excitation produces broader envelopes, resulting in reduced separation between adjacent peaks and a more extended temporal response.

Table 4.9: Error percentage in ToF for varying excitation types and frequencies for the skin and bone layer.

	ToF error percentage								
	Chirp			Pulse			Sine Burst		
	2 MHz	4 MHz	8 MHz	2 MHz	4 MHz	8 MHz	2 MHz	4 MHz	8 MHz
S	-0.0077	-0.0141	-0.0131	0.0115	-0.0115	-0.0125	-0.0205	-0.0256	-0.0247
B	0.0024	-0.0042	-0.0001	-0.0027	-0.0001	0.0004	0.0075	-0.0011	-0.0004

Abbreviations: S = Skin, B = Cortical bone.

When analysing the ToF results, the variability across excitation waveforms is limited, with comparable values obtained for chirp, pulse, and sine burst excitations across all frequencies and interfaces (Table 4.9 and Figure 4.5). In terms of magnitude, the relative error remains low for both skin and bone layers, staying below 3 % independent of excitation type and frequency. A general tendency towards negative error values is observed, particularly for the skin layer, indicating a slight systematic underestimation of the ToF. In contrast, the bone layer exhibits smaller deviations overall, with consistently lower error magnitudes compared to skin across all excitation conditions.

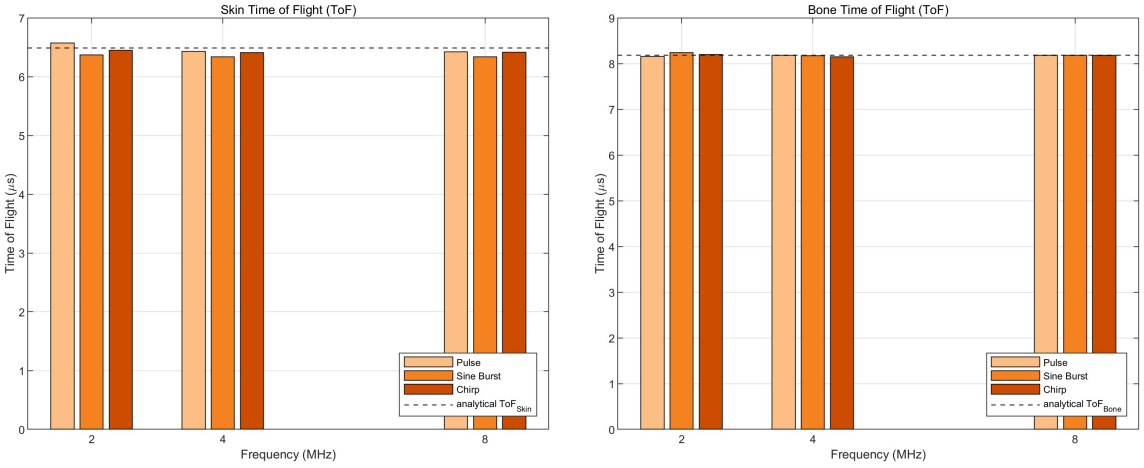

(a) Skin layer **(b)** Bone layer

Figure 4.5: Comparison of ToF errors for skin and bone across excitation frequencies of 2, 4, and 8 MHz. Error bars quantify variability across excitation waveforms (chirp, pulse, and sine burst), while the dashed horizontal line denotes the analytical reference solution. Subfigures correspond to (a) skin and (b) bone.

Based on the comparative analysis of chirp, pulse, and sine burst excitations, sine burst excitation is excluded from the subsequent analysis due to its consistently inferior performance in terms of temporal resolution and peak separation compared to chirp and pulse excitations.

4.2.3 Frequency-dependent Signal Behaviour

A detailed frequency sweep between 2 MHz and 8 MHz was performed for chirp and pulse excitation (Figures 4.6, 4.7). Across all interfaces, both excitation types exhibit consistent frequency-dependent behaviour.

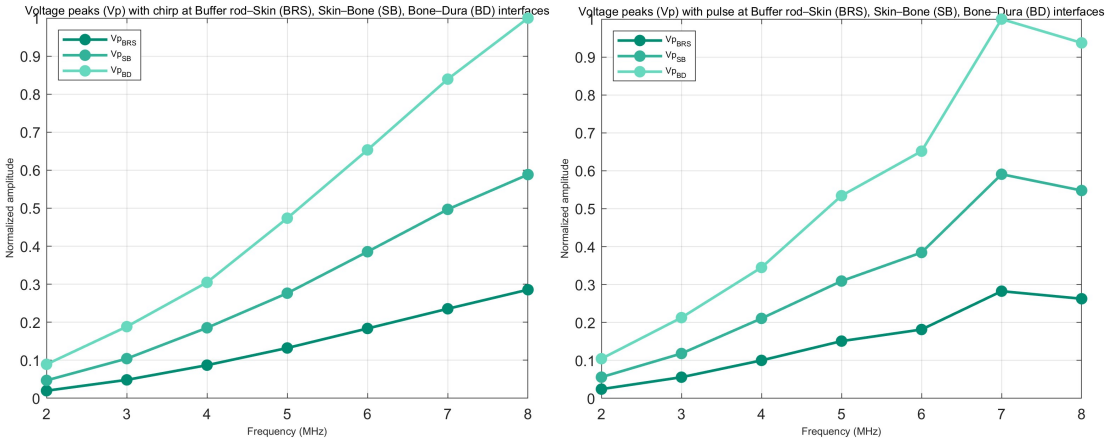

(a) Chirp excitation **(b)** Pulse excitation

Figure 4.6: Comparison of voltage peak (Vp) over a frequency range of 2–8 MHz at the buffer rod–skin (BRS), skin–bone (SB), and bone–dura (BD) interfaces for different excitations: (a) chirp and (b) pulse.

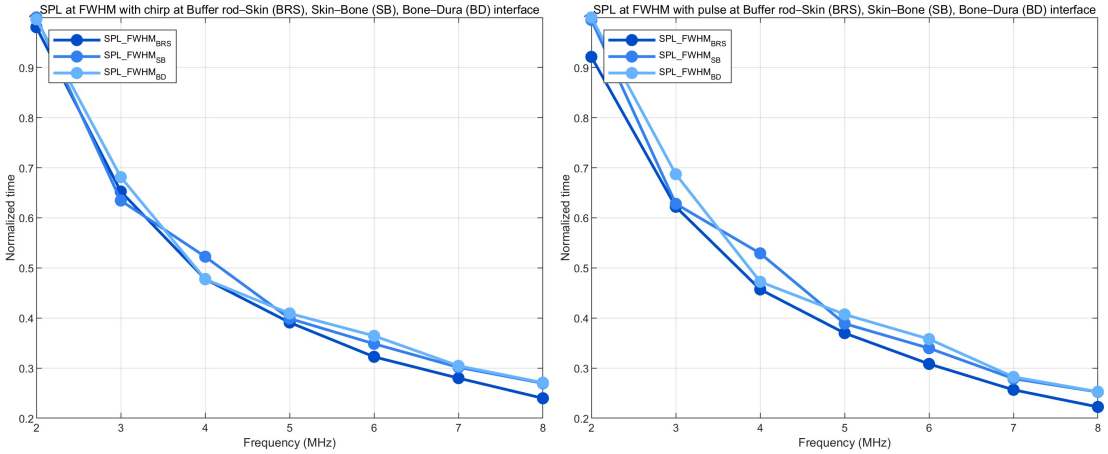

(a) Chirp excitation **(b)** Pulse excitation

Figure 4.7: Comparison of spatial pulse length at full width at half maximum (SPL@FWHM) as a function of frequency (2–8 MHz) at the buffer rod–skin (BRS), skin–bone (SB), and bone–dura (BD) interfaces for different excitations: (a) chirp and (b) pulse.

Table 4.10: Voltage peaks (V) for varying excitation frequencies with chirp excitation at material interfaces of interest.

Voltage peaks (V)							
	Frequency						
	2 MHz	3 MHz	4 MHz	5 MHz	6 MHz	7 MHz	8 MHz
BR–S	0.825	2.015	3.623	5.505	7.645	9.803	11.891
S–B	1.956	4.342	7.717	11.509	16.052	20.693	24.503
B–D	3.716	7.846	12.698	19.726	27.206	34.958	41.642

Abbreviations: BR = Buffer rod, S = Skin, B = Cortical bone, D = Dura mater. Interfaces are denoted by the materials on either side.

Table 4.11: Voltage peaks (V) for varying excitation frequencies with pulse excitation at material interfaces of interest.

Voltage peaks (V)							
	Frequency						
	2 MHz	3 MHz	4 MHz	5 MHz	6 MHz	7 MHz	8 MHz
BR–S	0.003	0.007	0.013	0.020	0.024	0.037	0.035
S–B	0.007	0.016	0.028	0.041	0.051	0.078	0.073
B–D	0.014	0.028	0.046	0.071	0.086	0.132	0.124

Abbreviations: BR = Buffer rod, S = Skin, B = Cortical bone, D = Dura mater. Interfaces are denoted by the materials on either side.

For chirp excitation, the peak amplitude remains relatively low up to approximately 4 MHz, after which a more pronounced increase is observed (Table 4.10). A similar trend is found for pulse excitation, where the voltage peak remains limited below 3–4 MHz and increases more markedly at higher frequencies (Table 4.11). In addition, at higher frequencies the relative difference in voltage peak between interfaces becomes more pronounced for both excitation types.

Table 4.12: SPL@FWHM (μs) for varying excitation frequencies with chirp excitation at material interfaces of interest.

SPL@FWHM (μs)							
	Frequency						
	2 MHz	3 MHz	4 MHz	5 MHz	6 MHz	7 MHz	8 MHz
BR–S	1.373	0.914	0.669	0.547	0.452	0.392	0.336
S–B	1.400	0.888	0.731	0.558	0.488	0.422	0.378
B–D	1.395	0.954	0.668	0.573	0.510	0.426	0.379

Abbreviations: BR = Buffer rod, S = Skin, B = Cortical bone, D = Dura mater. Interfaces are denoted by the materials on either side.

Table 4.13: SPL@FWHM (μs) for varying excitation frequencies with pulse excitation at material interfaces of interest.

SPL@FWHM (μs)							
	Frequency						
	2 MHz	3 MHz	4 MHz	5 MHz	6 MHz	7 MHz	8 MHz
BR–S	1.475	0.996	0.732	0.592	0.494	0.411	0.356
S–B	1.594	1.006	0.847	0.623	0.544	0.447	0.404
B–D	1.601	1.100	0.756	0.652	0.573	0.452	0.405

Abbreviations: BR = Buffer rod, S = Skin, B = Cortical bone, D = Dura mater. Interfaces are denoted by the materials on either side.

In contrast, the SPL@FWHM decreases with increasing frequency for both excitation types, reflecting progressively shorter SPLs at higher operating frequencies (Tables 4.12 and 4.13). Up to approximately 4 MHz, this reduction is more pronounced, with relatively large changes between successive frequency steps. Above approximately 6 MHz, the rate of reduction becomes smaller, indicating a gradual stabilization of the peak width. Notably, SPL@FWHM remains largely similar across all interfaces for a given frequency and excitation type, suggesting that spatial confinement is primarily governed by excitation frequency rather than interface properties.

Table 4.14: Error percentage in ToF for varying excitation frequencies with chirp excitation for skin and bone layers.

ToF error percentage							
	Frequency						
	2 MHz	3 MHz	4 MHz	5 MHz	6 MHz	7 MHz	8 MHz
S	-0.0062	-0.0173	-0.0126	-0.0128	-0.0122	-0.0113	-0.0116
B	0.0024	0.0079	-0.0042	0	0.0004	-0.0010	-0.0001

Abbreviations: S = Skin, B = Cortical bone.

Table 4.15: Error percentage in ToF for varying excitation frequencies with pulse excitation for skin and bone layers.

ToF error percentage							
	Frequency						
	2 MHz	3 MHz	4 MHz	5 MHz	6 MHz	7 MHz	8 MHz
S	0.0013	-0.0122	-0.0100	-0.0108	-0.0092	-0.0080	-0.0110
B	-0.0026	0.0099	-0.0001	0.0016	0.0018	-0.0005	0.0004

Abbreviations: S = Skin, B = Cortical bone.

The variation in ToF appears frequency-dependent but non-systematic, with fluctuations of the error percentage rather than a consistent increase or decrease (Tables 4.14 and 4.15). Across all configurations, the error magnitude is generally higher for the skin layer compared to the bone layer. For chirp excitation, the magnitude of the error remains consistently below 1.8 %, with the lowest deviations observed

at 2 MHz for the skin and at 5 MHz for the bone. For pulse excitation, the error magnitude is further reduced, remaining below 1.3 % across all frequencies. The lowest errors are observed at 2 MHz for the skin and at 4 MHz for the bone. Additionally, the errors are predominantly negative, indicating a tendency toward slight underestimation of the measured thickness.

Overall, the intermediate-frequency range is characterised by relatively close voltage peaks combined with a noticeable reduction in SPL@FWHM compared to lower frequencies. This region therefore represents a balance between signal amplitude growth and improved spatial confinement for both chirp and pulse excitations.

4.2.4 Parametric Study: Tissue Thickness Effects

Variations in tissue thickness lead to observable changes in the ultrasound signal characteristics and ToF. Differences in layer thickness primarily affect the temporal position and separation of reflected echoes, as well as the presence and spacing of secondary reflections within the signal.

4.2.4.1 Bone Thickness Variation

The effect of bone thickness on the received ultrasound signal was evaluated for thicknesses ranging from 3 mm to 10 mm (Figures 4.8, 4.9 and Figures B.4, B.5, B.6, and B.7 in Appendix B). For smaller thickness values, the back-wall echo of the bone appears in close temporal proximity to the front-wall reflection. Additionally, secondary peaks are observed following the main reflections, indicating the presence of multiple internal reflections within the layered structure. As the bone thickness increases, the temporal separation between the front-wall and back-wall echoes increases proportionally. This behaviour is consistent across both chirp and pulse excitation.

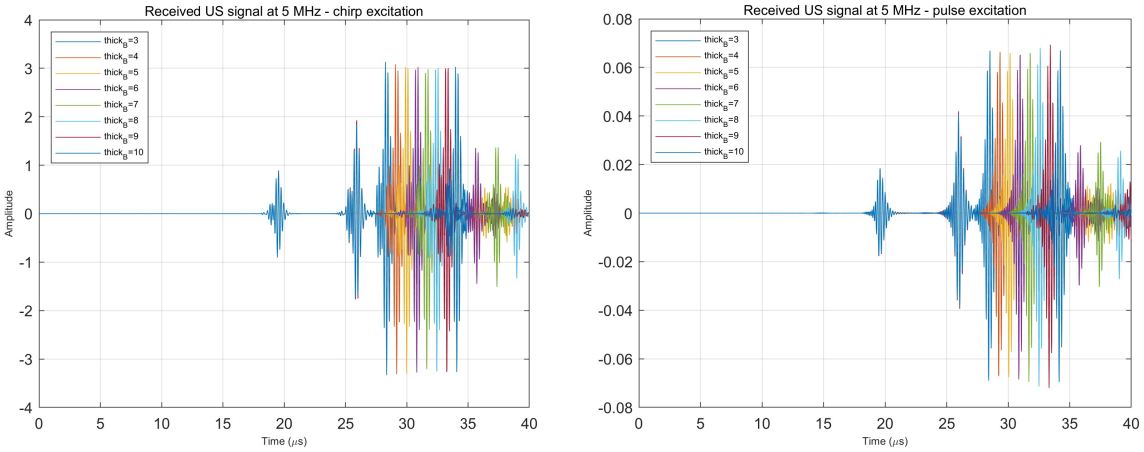

(a) Chirp excitation, 5 MHz

(b) Pulse excitation, 5 MHz

Figure 4.8: Comparison of received ultrasound signals across varying bone thicknesses (3–10 mm) for different excitations: (a) chirp, and (b) pulse.

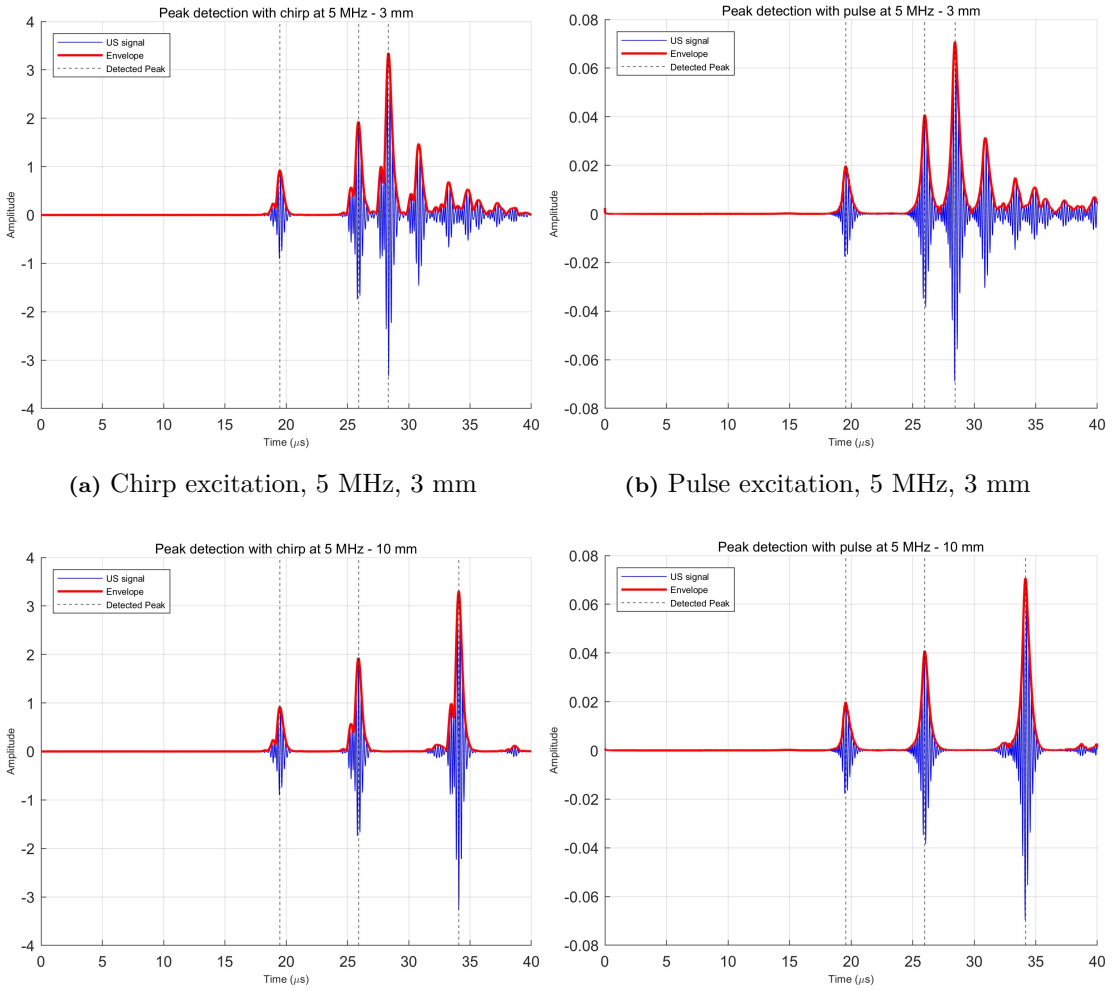

(a) Chirp excitation, 5 MHz, 3 mm

(b) Pulse excitation, 5 MHz, 3 mm

(c) Chirp excitation, 5 MHz, 10 mm

(d) Pulse excitation, 5 MHz, 10 mm

Figure 4.9: Comparison of raw ultrasound signals, amplitude envelopes, and detected peaks for chirp and pulse excitation for extreme-case bone thicknesses: (a, b) 3 mm, and (c,d) 10 mm.

Table 4.16: Error percentage in ToF of the bone with chirp excitation for different bone thicknesses and frequencies.

ToF error percentage								
	Bone thickness							
	3 mm	4 mm	5 mm	6 mm	7 mm	8 mm	9 mm	10 mm
4 MHz	-0.0041	0.0031	-0.0024	-0.0061	-0.0035	-0.0061	-0.0027	-0.0024
5 MHz	-0.0041	-0.0031	-0.0024	0.0020	0	0	0	0
6 MHz	-0.0041	0.0031	-0.0024	-0.0020	0	0	0	0

Table 4.17: Error percentage in ToF of the bone with pulse excitation for different bone thicknesses and frequencies.

ToF error percentage								
	Bone thickness							
	3 mm	4 mm	5 mm	6 mm	7 mm	8 mm	9 mm	10 mm
4 MHz	0.0122	-0.0031	-0.0024	-0.0061	-0.0070	0	-0.0027	0
5 MHz	0.0041	-0.0031	0.0024	0.0020	0.0070	0.0031	0	0
6 MHz	-0.0041	0.0031	-0.0024	-0.0020	0.0035	0	0	0.0024

When analysing the ToF error across varying bone thicknesses, the results exhibit consistently low variability for both chirp and pulse excitations over the investigated frequency range (Tables 4.16, 4.17). The relative error remains minimal in all cases, always with magnitude below 1.2 %. The largest deviation is observed for pulse excitation at 4 MHz and 3 mm bone thickness, representing the only instance exceeding 1 % error magnitude. In contrast, several configurations result in error values equal to 0 %, predominantly at higher thicknesses of 8, 9, and 10 mm. Notably, such zero-error cases are less frequent for pulse excitation, with six instances, compared to eight instances for chirp excitation, suggesting a higher occurrence of exact ToF under chirp-based configurations.

4.2.4.2 Skin Thickness Variation

In the same way, the effect of skin thickness on the received US signal was evaluated for thicknesses ranging from 3 mm to 10 mm (Figures 4.10, 4.11 and Figures B.8, B.9, B.10, and B.11 in Appendix B). Across all configurations, the front- and back-wall reflections of the skin layer remain clearly identifiable, with the back-wall echo shifting progressively in time as thickness increases. For the thinner cases, the two main reflections are closely spaced in time and the appearance of additional minor peaks attributed to internal secondary reflections. As thickness increases, these reflections become more temporally separated. This trend is consistently observed for both chirp and pulse excitation.

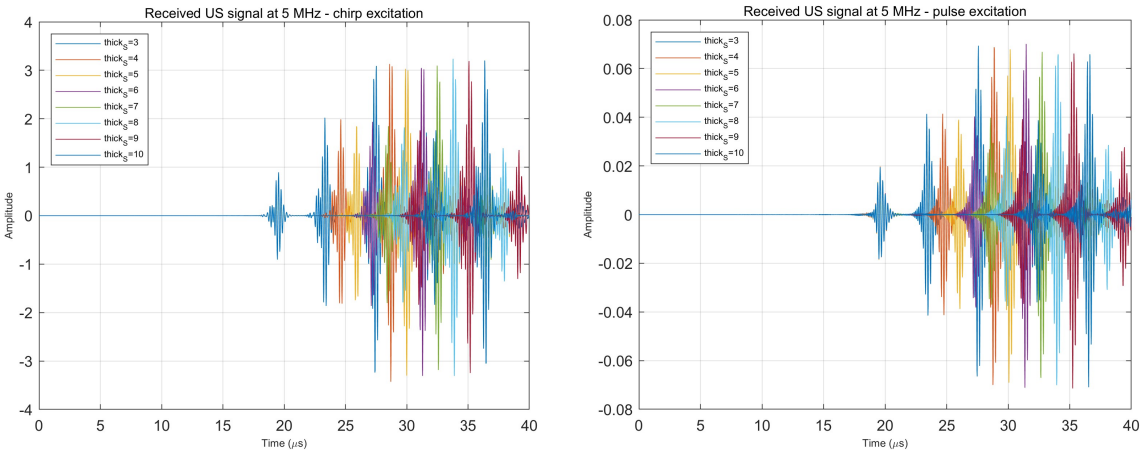

(a) Chirp excitation, 5 MHz

(b) Pulse excitation, 5 MHz

Figure 4.10: Comparison of received ultrasound signals across varying skin thicknesses (3–10 mm) for different excitations: (a) chirp, and (b) pulse.

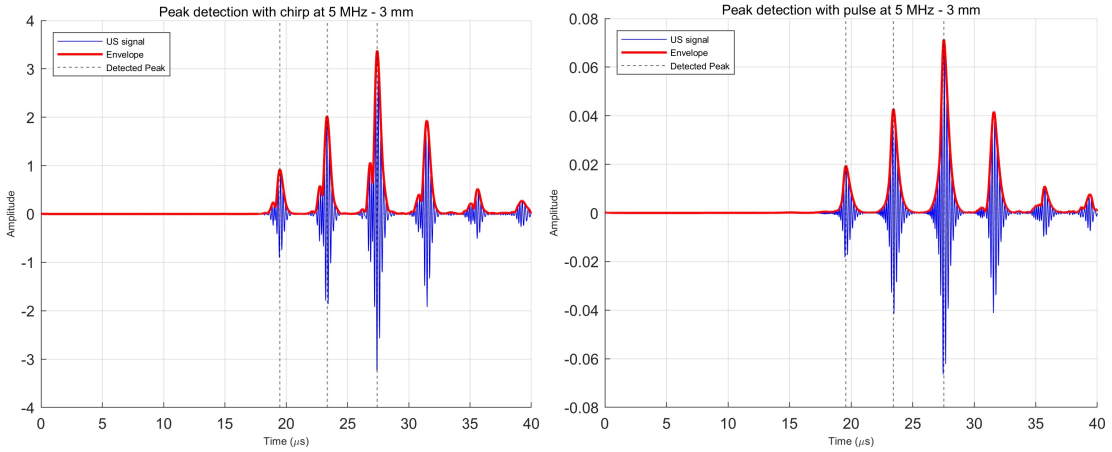

(a) Chirp excitation, 5 MHz, 3 mm

(b) Pulse excitation, 5 MHz, 3 mm

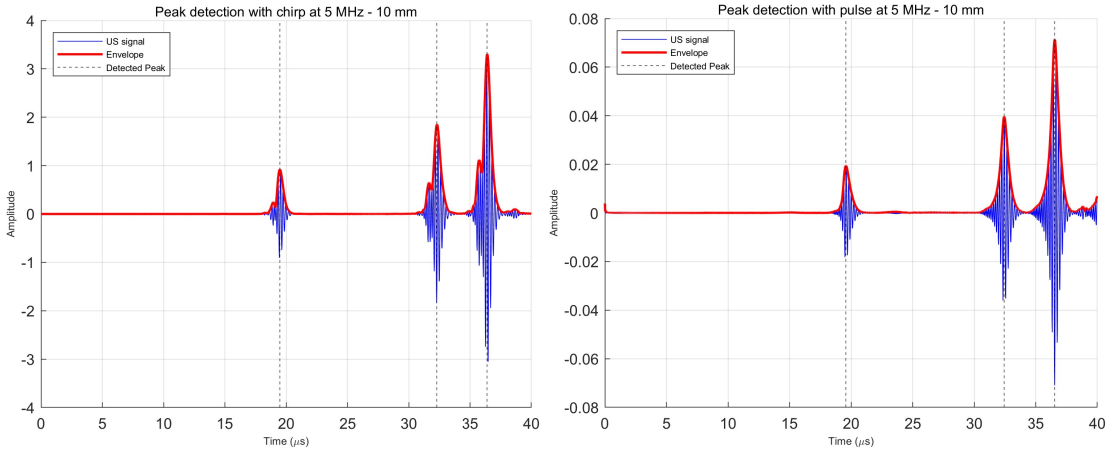

(c) Chirp excitation, 5 MHz, 10 mm

(d) Pulse excitation, 5 MHz, 10 mm

Figure 4.11: Comparison of raw ultrasound signals, amplitude envelopes, and detected peaks for chirp and pulse excitation for extreme-cases of skin thickness: (a, b) 3 mm, and (c,d) 10 mm.

Table 4.18: Error percentage in ToF of the skin with chirp excitation for different skin thicknesses and frequencies.

ToF error percentage								
	Skin thickness							
	3 mm	4 mm	5 mm	6 mm	7 mm	8 mm	9 mm	10 mm
4 MHz	-0.0154	-0.0135	-0.0139	-0.0116	-0.0121	-0.0125	-0.0128	-0.0131
5 MHz	-0.0103	-0.0135	-0.0108	-0.0116	-0.0121	-0.0125	-0.0128	-0.0131
6 MHz	-0.0154	-0.0135	-0.0139	-0.0116	-0.0121	-0.0125	-0.0128	-0.0115

Table 4.19: Error percentage in ToF of the skin with pulse excitation for different skin thicknesses and frequencies.

ToF error percentage								
	Skin thickness							
	3 mm	4 mm	5 mm	6 mm	7 mm	8 mm	9 mm	10 mm
4 MHz	-0.0205	-0.0135	-0.0077	-0.0116	-0.0121	-0.0106	-0.0128	-0.0115
5 MHz	-0.0103	-0.0135	-0.0077	-0.0116	-0.0099	-0.0106	-0.0094	-0.0115
6 MHz	-0.0154	-0.0096	-0.0077	-0.0090	-0.0099	-0.0087	-0.0094	-0.0100

When analysing the ToF error across varying skin thicknesses, the results exhibit consistently low variability for both chirp and pulse excitations over the investigated frequency range (Tables 4.18, 4.19). For chirp excitation, the error is uniformly negative with magnitude remaining between 1 % and 1.5 %, suggesting a very small but systematic underestimation. For pulse excitation, the underestimation persists, but a slightly higher sensitivity to thickness variations is observed at lower values, particularly at 3 mm, where the maximum error magnitude of 2 % is recorded at 4 MHz. However, as thickness increases, error magnitude remain between 0.8 % and 1.4 %.

4.2.4.3 Worst Case Scenario

Under worst case conditions, the determination of the ToF remained robust for both chirp and pulse excitation at operating frequencies of 4, 5, and 6 MHz (Figure 4.12, and Figure B.12 in Appendix B). The variation in ToF error was relatively limited across the investigated frequency range, although a stronger frequency dependence was observed for pulse excitation compared to chirp excitation. For chirp excitation, the error magnitude associated with the skin layer remained consistently close to 1.5 %, while the error magnitude for the bone layer remained below 1 % at all frequencies and approached zero at 5 MHz. For pulse excitation, the skin-layer error increased in magnitude from 0.8 % at 4 MHz to 1.7 % at 6 MHz. In contrast, the error magnitude for the bone layer varied between 1.9 % and 0.1 %, with the smallest deviation again observed at 5 MHz.

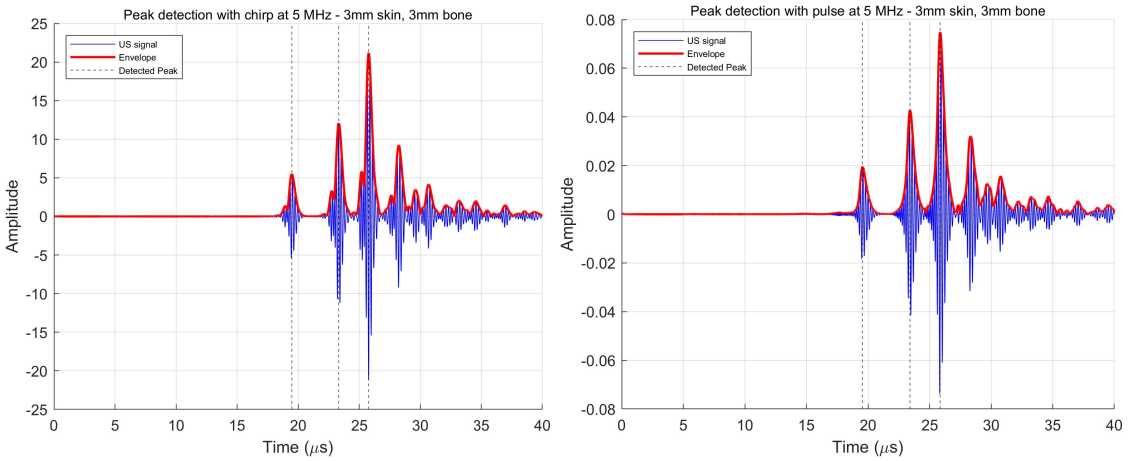

(a) Chirp excitation, 5 MHz

(b) Pulse excitation, 5 MHz

Figure 4.12: Comparison of raw ultrasound signals, amplitude envelopes, and detected peaks results under worst-case operating conditions at operating frequency of 5 MHz for different excitations: (a) chirp and (b) pulse.

4.2.5 Extended Study Including a Blood Vessel Structure

The reference simulation was compared with the two investigated vessel geometries for chirp excitation at 5 MHz (Figure 4.13).

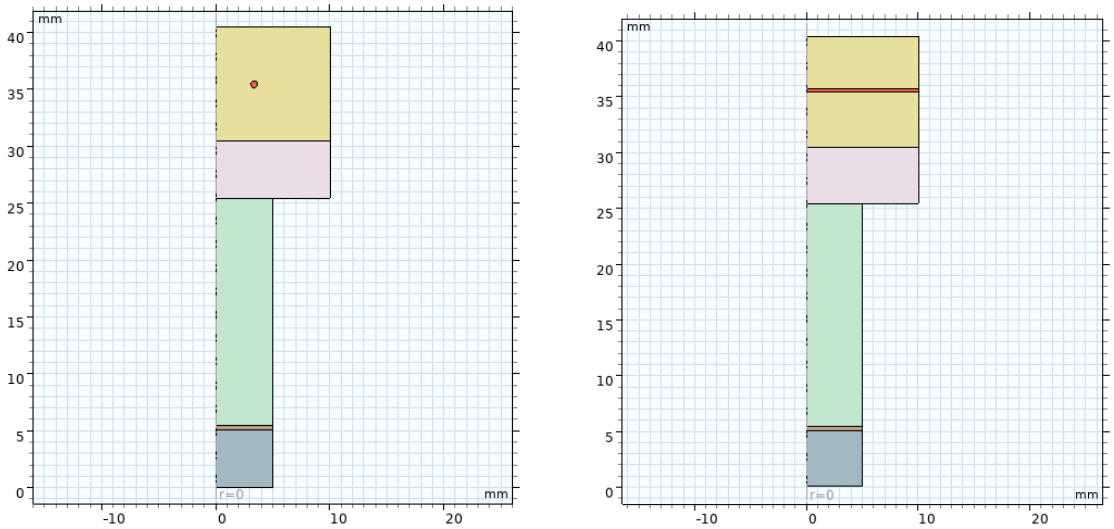

(a) Randomly placed vessel

(b) Extended vessel layer

Figure 4.13: Schematic representation of the multilayer acoustic model with the investigated vessel structures. The gray region denotes the backing layer, the brown region the piezoelectric element, the green region the buffer rod, the pink region the soft tissue layer, the yellow region the cortical bone layer, and the red region the blood vessel.

The ToF remained robust across all configurations, with the associated error magnitude consistently remaining below 1.3 %. Compared to the reference case without

vessel inclusion, both vessel geometries introduced additional reflections in the received RF signal (Figure 4.14). The vessel randomly positioned within the bone layer resulted in more temporally distributed secondary peaks, increasing signal complexity while preserving the main reflection structure. In contrast, the extended vessel layer generated a more distinct additional peak associated with the blood–vessel interface, accompanied by increased distortion and temporal broadening of the bone-related reflection. Despite these effects, the SNR remained high across all cases, ranging between 50 and 60 dB, ensuring reliable identification of the principal reflections.

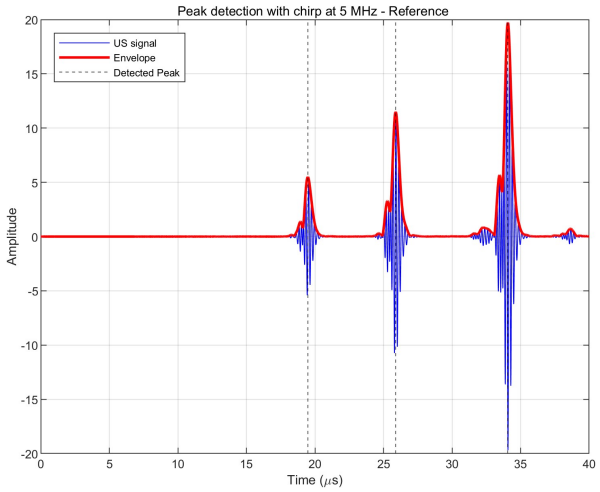

(a) Reference

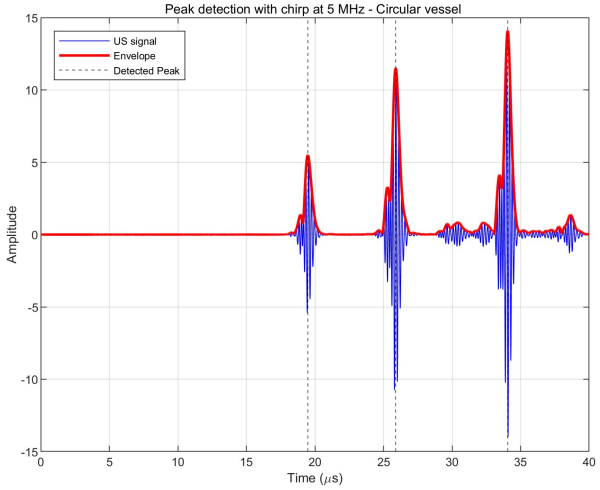

(b) Circular Geometry

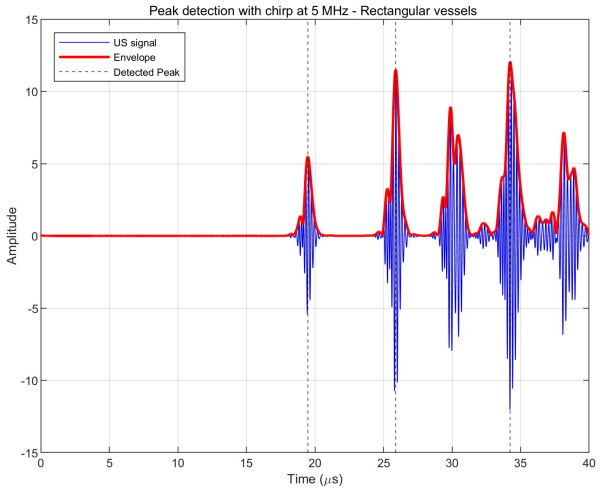

(c) Rectangular Geometry

Figure 4.14: Comparison of raw US signals, amplitude envelopes, and detected peaks for chirp excitations at 5 MHz for different configurations: (a) reference model without vessel inclusion, (b) model with the vessel randomly position within the bone layer, and (c) model with the extended vessel layer.

5 Discussion

This chapter discusses the results presented in Chapter 4 in relation to the purpose of evaluating ultrasound for determining soft tissue and cortical bone thickness in the temporal bone region prior to Ponto implantation. The findings are interpreted in terms of ultrasound wave propagation, excitation waveform, operating frequency, and multilayer tissue interactions, and are compared with previous studies related to ultrasound-based thickness estimation. In addition, the limitations of the analytical and numerical models are addressed, together with the implications of the results for future development and potential clinical implementation of the proposed method.

5.1 Summary of Results

The aim of this thesis was to investigate whether ultrasound can be used to site-specifically determine soft tissue and cortical bone thickness in the temporal bone region to support the preoperative assessment in Ponto implantation. Overall, the results indicate that the determination of ultrasound-based thickness is technically feasible under the analytical and numerical conditions considered in this study. Simulated pulse-echo signals showed that reflections from the relevant interfaces, including the buffer rod-skin, skin-bone, and bone-dura interfaces, could be distinguished.

The results showed that the skin layer thickness could be determined for all investigated thicknesses. The front-wall and back-wall reflections were clearly detectable, and the ToF error remained low in magnitude both with chirp and pulse excitation. While chirp and sine burst excitation produced the highest peak amplitudes, chirp and pulse excitation resulted in the narrowest peaks. Consequently, chirp excitation generally provided the best overall signal characterization, although pulse excitation demonstrated comparable performance. In the skin thickness sweep, the results showed a small systematic underestimation, with ToF error magnitude generally between 0.8 % and 1.5 %. The largest deviation was of 2 % and occurred for the thinnest skin layer of 3 mm using pulse excitation at 4 MHz. Even in the worst-case scenario, the skin-layer ToF error magnitude remained within a limited range, close to 1.5 % at all frequencies for chirp and between 0.8 % and 1.7 % for pulse excitation.

Similarly, the results for bone thickness determination were promising. The reflections from the front-wall and back-wall were detected for all investigated thicknesses. The ToF error magnitude was generally lower in magnitude for bone than for skin, remaining below 1 % in the frequency sweep. The lowest ToF error magnitude was observed with chirp excitation at 5 MHz, where the error was zero, and at 4 MHz for pulse excitation. In the bone thickness sweep, the ToF error magnitude remained below 1.3 %. Several configurations with larger bone thicknesses of 7, 8, 9, and 10 mm resulted in zero or near-zero error. In the worst-case scenario, the bone-layer

ToF error magnitude remained below 1 % at all frequencies and approached zero at 5 MHz for chirp excitation and varied between 0.1 % and 1.9 % for pulse excitation, again with the smallest deviation observed at 5 MHz. These results indicate that the determination of bone thickness is feasible despite the more challenging propagation conditions in hard tissue.

For the blood vessel simulation, the results showed that additional anatomical structures can introduce additional reflections, but the main reflections remained identifiable and the ToF error magnitude stayed below 1.3 %.

Importantly, the simulations confirms that both skin and bone thickness can be determined with the clinically required accuracy. The required accuracy was 1.5 mm for soft tissue thickness and 1 mm for bone thickness. Since the ToF error remained below 2 % in all investigated configurations, the corresponding thickness error would remain below these margins even for the smallest investigated tissue thickness of 3 mm. Under the simplified simulation conditions, the method therefore appears accurate enough to support the selection of suitable abutment and implant lengths.

Finally, the analytical model provided preliminary transducer design parameters for future development. The results indicated that suitable combinations of operating frequency and transducer dimensions could achieve a favorable balance between signal amplitude, temporal separation, and ToF accuracy. Both chirp and pulse excitation were suitable in terms of accuracy. However, pulse excitation may be advantageous for a future prototype because it is simpler to generate and process.

5.2 Interpretation and Comparison with Literature

The findings of this study are consistent with previous research showing that ultrasound can determine tissue thickness from echoes reflected at tissue interfaces. Earlier studies have applied this principle to both soft tissue and bone, although typically these tissues have been investigated separately. To the authors' knowledge, no previous study has specifically investigated an ultrasound-based method to determine both skin and bone thicknesses at the same measurement site in the temporal bone region for applications related to BC implants.

A particularly relevant reference point for this work is the SonoPointer concept [6], which demonstrated the feasibility of ultrasound-based local skull thickness estimation and motivated the use of coded excitation to improve echo detectability from bone interfaces. Chirp excitation can increase transmitted acoustic energy while preserving axial resolution after signal processing, making it advantageous when attenuation is significant or echoes are weak. However, the SonoPointer focused only on bone thickness estimation and did not address the additional challenge of measuring the overlying skin layer. Since this project builds on the same pulse-echo principle, chirp excitation was included as a natural starting point.

In addition to chirp excitation, sine burst and pulse excitation were investigated. Sine burst excitation represents a more conventional ultrasound signal and was also evaluated in the SonoPointer approach, while pulse excitation was included as a simpler alternative requiring less signal design and post-processing. Beyond comparing measurement performance, the purpose was to assess whether a less complex excitation strategy could still provide sufficient performance for a compact and clinically practical system.

The results showed that pulse excitation achieved comparable performance to chirp excitation under the investigated conditions. This suggests that the additional complexity of chirp excitation may not be necessary under the tested conditions. Although chirp excitation remains beneficial when higher transmitted energy or improved echo detectability is required, the findings suggest that reliable determination of both skin and bone thickness may also be achieved using a simpler pulse-based approach.

5.3 Explanation of Results

The analytical modelling and numerical simulations demonstrated that ultrasonic system behaviour depends on the interaction between excitation waveform, operating frequency, multilayer geometry, and acoustic interface properties. Although Chapter 4 presented trends in voltage peak, SPL, and ToF, these parameters are closely interconnected and reflect the underlying physics of ultrasonic wave propagation in biological tissues. Accurate thickness estimation therefore depends on balancing transmitted acoustic energy, temporal pulse confinement, and the ability to resolve successive reflections within the layered model. These interactions help explain why certain excitation strategies and frequency ranges provide more robust and reliable estimation of both soft tissue and cortical bone thickness.

5.3.1 Influence of Excitation Waveform on Signal Characteristics

The differences between chirp, pulse, and sine burst excitation are primarily related to the way each waveform distributes the acoustic energy in time and frequency, which directly influences the received ultrasound signal. Chirp excitation consistently produced the highest voltage peaks because its broadband and longer-duration waveform transferred more acoustic energy into the multilayer structure, resulting in stronger reflected echoes from the interfaces. In contrast, pulse excitation generated lower voltage peaks due to its shorter temporal duration and lower transmitted energy, while sine burst excitation generated broader temporal responses because of its multi-cycle structure.

These waveform-dependent properties strongly affected the SPL and the separation of successive reflections. The broader SPL values of sine burst excitation produced more extended waveforms, increasing overlap between successive echoes and reducing the accuracy of peak localization. In contrast, chirp and pulse excitation

produced sharper and more temporally confined responses, improving the separation of interface reflections and enabling a more reliable determination of the ToF.

Interestingly, pulse excitation achieved ToF accuracies similar to chirp excitation despite its lower signal amplitudes. This suggest that accurate determination of thickness depends not only on strong echoes, but also on having a compact and well-defined waveform. Overall, the results demonstrate the trade-off between signal energy and temporal resolution: chirp excitation improved signal detectability, while pulse excitation offered a simpler but still highly effective alternative for the determination of multilayer thickness.

5.3.2 Frequency-dependent Behaviour and Resolution Trade-offs

The frequency-dependent behaviour observed in the simulations is mainly governed by the relationship between excitation frequency, acoustic wavelength, and temporal confinement. As the excitation frequency increased from 2 MHz to 8 MHz, the SPL@FWHM decreased for both chirp and pulse excitation. This happened because higher frequencies correspond to shorter acoustic wavelengths, which naturally create more compact and temporally localized echoes. As a result, the system achieved better axial resolution and improved separation between successive reflections, making it easier to identify the different interfaces within the multilayer structure. The reduction in SPL was most pronounced at the lower frequencies, whereas the improvement gradually became less significant above approximately 6 MHz, indicating that increasing frequency beyond this point provided only limited gain in temporal confinement.

At the same time, the voltage peak increased with frequency for both excitation waveforms. Shorter wavelengths appear to interact more effectively with the acoustic interfaces, and the transducer may also operate more efficiently at higher frequencies. Although higher frequencies are normally linked to greater attenuation in biological tissue, the propagation distances in this study were short enough that the advantages of improved temporal confinement and interface sensitivity remained dominant.

Together, these findings demonstrate that the most balanced overall performance was obtained within an intermediate-frequency range. At lower frequencies, the broader pulse lengths caused greater overlap between echoes and reduced temporal resolution. At higher frequencies, however, the improvements became progressively smaller. The results, therefore, highlight the established trade-off in ultrasound design between resolution and propagation behaviour, where the intermediate frequencies provided the most stable conditions for accurate determination of multilayer thickness.

5.3.3 Mechanisms Influencing Time-of-flight Accuracy

The consistently low ToF errors observed throughout the simulations indicate that the dominant reflections within the multilayer structure remained sufficiently distin-

guishable across all investigated configurations. Accurate determination of ToF was mainly determined by the balance between signal amplitude, temporal compactness, and echo separability. Higher voltage peaks made interface-related reflections easier to detect and reduced uncertainty during peak localization, while shorter SPLs improve temporal precision by producing sharper echoes with less waveform spreading and overlap. Together, these factors improved the reliability of the arrival-time estimation.

The lower ToF errors observed for cortical bone compared to skin are likely related to the stronger acoustic impedance mismatch at the bone interface, which produced clearer and more distinct reflections. In contrast, the skin-related reflections were more influenced by the short propagation distance, interference with nearby reflections within the superficial layers, and the different material modelling approaches used in the simulations. Bone was modelled as a solid material, whereas skin was represented as an elastic medium, which likely introduced greater wave distortion and more complex propagation behaviour in the superficial layers.

The effect of tissue thickness also highlights the importance of echo separation. For thinner skin and bone layers, the front-wall and back-wall reflections occurred in close temporal proximity, increasing the possibility of overlap between echoes. As the layer thickness increased, the reflections became progressively more separated, reducing ambiguity in peak localization and improving the stability of the determined ToF. This also explains why several cases with almost zero error were observed at larger thicknesses.

The slight systematic underestimation observed in many configurations may additionally be related to the envelope detection process itself, where the detected envelope peak can appear slightly earlier than the theoretical centre of the reflected pulse. Overall, the results demonstrate that reliable determination of ToF in multilayer biological structures depends on maintaining a balance between signal strength, temporal confinement, and sufficient separation between the dominant echoes.

5.3.4 Influence of Multilayer Geometry

The multilayer geometry of the investigated model strongly influenced the temporal behaviour of the received ultrasound signals. As the ultrasonic wave encountered interfaces with different acoustic impedances, reflections and transmissions occurred at each boundaries. This created not only the primary echoes needed for the determination of thickness, but also additional secondary reflections and reverberations within the signal. As a result, tissue thickness mainly affected how closely these reflections appeared in time.

For thinner skin and bone layers, the front-wall and back-wall reflections occurred very close together, increasing waveform overlap and making secondary reflections more visible. When the layer thickness increased, the temporal separation between reflections also increased, allowing the interfaces to be distinguished more clearly and reducing the influence of waveform interaction on peak localization. This explains

the improved stability of the determination of ToF observed for larger thicknesses.

Introducing blood vessel geometries added another level of complexity to the received signals by creating additional reflecting interfaces along the propagation path. The randomly positioned vessel produced more distributed secondary peaks, meaning the reflected energy was spread over a wider temporal interval. In contrast, the extended vessel layer generated a more localized additional reflection together with increased temporal broadening of the bone-related echo. Despite this added complexity, the dominant reflections associated with the relevant interfaces remained identifiable, and the SNR remained high enough to allow stable peak detection. These findings suggest that the proposed ultrasound approach remains relatively robust even when the anatomical complexity increases, as long as the dominant interface reflections remain temporally distinguishable.

5.4 Limitations

Since this study was mainly based on analytical and numerical modelling, the results should be interpreted in relation to the assumptions and simplifications used. The main limitations are related to methodological choices in the study and to the level of detail of the models.

5.4.1 Methodological Limitations

One limitation is that the numerical simulations were evaluated against a simplified analytical model. The analytical model served as the ground truth reference, allowing the simulations to be assessed under controlled conditions. However, the analytical model is also based on assumptions and simplifications. Agreement between the numerical and analytical results should therefore be interpreted as verification of the numerical model under idealized conditions, rather than a validation of the method under realistic measurement settings.

A further limitation is that the signal extraction method was not fully consistent across all simulation studies. In the frequency-dependent analysis, the voltage signal at the piezo-buffer rod interface was obtained using a boundary probe, whereas a spatial line average over the same interface was used in the parametric study due to numerical limitations. Since these methods are not exactly equivalent, small differences in peak voltage, SPL and ToF may occur even for identical configurations. For this reason, the results should mainly be interpreted in terms of trends within each parameter study, rather than through direct quantitative comparisons between studies.

Finally, no experimental validation was included in this study. The results are therefore theoretical and simulation-based. Without measurements on tissue-mimicking phantoms, ex vivo samples, or human subjects, the accuracy and robustness of the method under practical conditions cannot be determined. Factors such as acoustic

coupling, probe positioning, surface curvature, measurement noise and biological variability were therefore not fully evaluated.

5.4.2 Modelling Limitations

The geometry used in the models was simplified compared with the real anatomy of the temporal bone region. The simulated tissue layers were represented using idealized geometries and clearly defined interfaces, while the real retroauricular region contains curved, heterogeneous, and patient-specific structures. Variations in tissue thickness, bone shape, and local anatomy were therefore not fully represented, which may affect how well the model represents ultrasound propagation and interface detection in practical measurements.

The material properties of biological tissues were also simplified. Soft tissue and bone were assigned fixed acoustic properties, although these properties vary between patients, anatomical locations, and tissue composition. Bone is especially complex, since its acoustic behaviour depends on factors such as density and porosity. The use of fixed material parameters therefore limits the ability of the model to represent patient-specific conditions and the full range of clinically relevant cases.

The analytical and numerical models were based on simplified descriptions of wave propagation. The analytical model assumed ideal wave propagation, simplified interface reflections, and known acoustic material properties, while the numerical model did not fully account for effects such as scattering, viscoelastic tissue behaviour, shear waves, or detailed bone microstructure. Although these assumptions made the models more manageable and suitable for studying general trends, they may affect the predicted reflection amplitudes, arrival times, and waveform shapes.

There are also limitations related to the numerical implementation. The computational domain was finite, and low-reflecting boundary conditions were used to approximate an open domain. Although these boundary conditions reduce artificial reflections, they do not remove them completely. In addition, numerical choices such as mesh resolution, time step size and discretization may introduce small errors in the simulated results.

Overall, the modelling results should be interpreted in relation to the assumptions and simplifications used in the study. The simulations provide useful insight into how different parameters may affect the ultrasound response, but they do not establish the clinical accuracy of the method.

6 Future Work

This chapter outlines possible directions for future work. The focus is on improving the modelling approach, validating the method experimentally, and exploring how the concept could be developed into a practical ultrasound-based measurement device for preoperative assessment.

6.1 Advanced Modelling Technique

The modelling approach used in this work is based on simplified descriptions of ultrasound wave propagation in biological tissues. These simplifications were necessary to keep both the analytical model and the numerical simulations computationally manageable. Future work could expand the model in several directions, including more realistic anatomical descriptions [47]. In addition alternative excitation signals, different transducer configurations, improved material selection, more advanced signal processing methods may further improve the interpretation of complex ultrasound signals and increase the clinical relevance of the simulations.

One important direction for future work is a more detailed representation of biological tissues and bone structures. In this study, the skin was modelled as a single homogeneous layer, while the bone was primarily treated as a homogeneous solid. In reality, both soft tissue and bone contain multiple internal structures with different mechanical properties that influence wave propagation, attenuation, reflections, and scattering. A first step toward a more realistic representation was explored by introducing a simplified blood vessel geometry into the bone model. The results showed that internal structures can significantly influence the received signal and create overlapping echoes, indicating that more advanced signal analysis techniques will likely be required for increasingly realistic anatomical models.

Another aspect that could be explored in future work is the use of alternative excitation signals. In this study, three excitation signals were evaluated: a chirp, a sine burst, and a pulse. The chirp and sine burst were selected based on previous literature, while the pulse was included to represent a short broadband excitation commonly used in medical ultrasound. Although these signals provided a useful comparison, other waveform designs, frequency contents, and modulation strategies could also be investigated to further optimize ultrasound performance.

Future studies could also investigate other transducer configurations beyond the single-element design used in this work. The single-element transducer enabled a controlled analysis of wave propagation and interface reflections, but other designs, such as dual-element transducers, may provide advantages in practical pulse-echo applications. Dual-element configurations can improve the separation between trans-

mitted and received signals, reduce transducer ring-down effects, and increase sensitivity close to the transducer surface. Exploring such configurations could therefore provide additional insight into probe performance and measurement accuracy.

Another area for future investigation is the choice of buffer rod material. PMMA was selected in this work because it provided a practical and well-defined material for the simulations. However, alternative materials may influence acoustic impedance matching, attenuation, internal reflections, and signal transmission differently. Evaluating different buffer rod materials could therefore contribute to improved ultrasound system performance.

Overall, the future development of this work points toward the combination of more realistic anatomical modelling and more advanced signal processing techniques. Although such improvements will increase model complexity, they are expected to produce more accurate ultrasound simulations and improve the relevance of the results for practical and clinical applications.

6.2 Experimental Validation

A part of future work should include experimental validation of the proposed ultrasound based method to determine thickness using a controlled bench top setup. As this thesis focuses on analytical modelling and numerical simulations, experimental testing is necessary to verify if the simulation results are replicable under practical measurement conditions.

The proposed setup consists of a pulser/receiver, an ultrasound transducer , a coupling medium, a layered material model, an oscilloscope or data acquisition system and a signal-processing stage (Figure 6.1). The pulser/receiver would excite the ultrasound transducer, which would transmit ultrasound waves through the coupling medium and into the layered material model. Reflections would occur at the interfaces between the different layers. The reflected echoes would then be received by the transducer, recorded by the oscilloscope or data acquisition system and processed to determine the layered thickness.

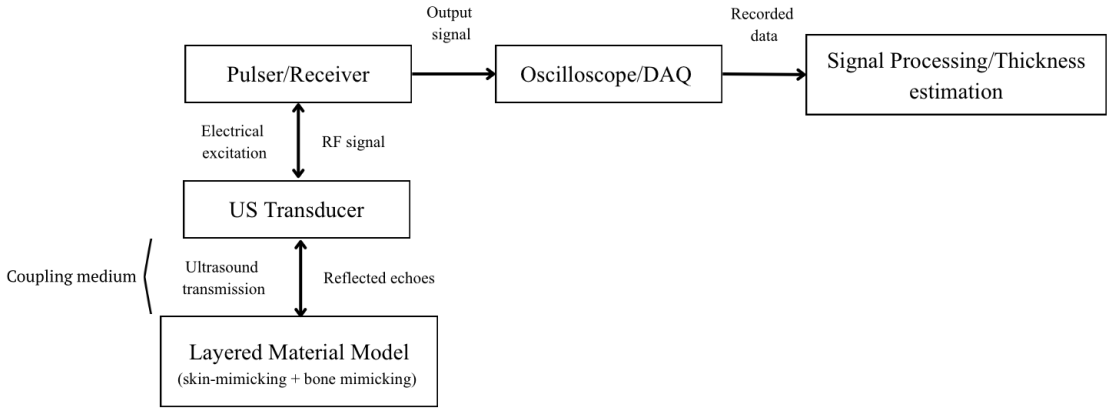

Figure 6.1: Proposed experimental setup for future experimental validation of the ultrasound-based thickness estimation method. The pulser/receiver excites the transducer, which transmits ultrasound into a layered material mode, through a coupling medium. Reflected echoes are recorded and processed to determine layer thickness.

The layered material model should consist of skin- and bone-mimicking materials with known and preferably adjustable thicknesses. Since thickness variations were investigated analytically and numerically, adjustable layers would allow the same conditions to be tested experimentally. This would make it possible to evaluate whether the same signal trends can be observed and if the method remains accurate across different skin and bone thicknesses.

Several practical factors should be controlled during testing, including probe alignment, coupling conditions and contact pressure, since these factors may affect the received signal and thus the determination of thickness. The acoustic properties of the layered material model should also be known, since the speed of sound is used to calculate thickness from the time-of-flight. If the bench top results are successful, future work could continue with more realistic phantoms and ex-vivo samples.

6.3 Future Device Design

Future work could investigate the design of a simplified ultrasound device intended specifically for pre-operative soft tissue assessment. Although the broader objective of this project includes the determination of both skin and bone thickness, a first clinical prototype may be more feasible if it focuses only on skin thickness, since this would directly address the challenge of selecting the correct abutment length for the Ponto system. By providing a local measurement of soft tissue thickness at the planned implant site, the device could reduce costs and simplify logistics by minimizing the need to order and ship all abutment variants.

The device could be designed as a compact handheld probe, either with an integrated display or a connection to a small external monitor. The clinician would place the probe on the skin behind the ear, perform a pulse-echo measurement, and receive a single output value corresponding to the local skin thickness. Limiting the device to skin thickness measurement would reduce the technical complexity significantly

since the system would only need to detect the echoes from the soft tissue-bone interface, which is relatively superficial. Rather than penetration depth, the design would prioritize axial resolution. Therefore, a relatively high center frequency combined with a short excitation pulse, could be suitable for accurate determination of time-of-flight for this application.

A later version could include bone thickness measurement, where the output would include both skin and bone thickness (Figure 6.2). This would require the detection of deeper and weaker echoes, making the system more dependent on penetration depth, signal-to-noise ratio, frequency selection, and more advanced signal processing, a concept that was investigated in this thesis. In either case, the probe should preferably have a small diameter to allow for local measurements in specific areas of the temporal bone region. This could help the clinician compare nearby measurement points and identify the optimal implant site by avoiding areas with poor acoustic coupling, air gaps, large blood vessels, or insufficient bone thickness. In addition, a pressure sensor could be integrated into the probe head to account for the pressure applied by the clinician during the measurement.

Figure 6.2: Conceptual visualization of a possible future handheld ultrasound device with an integrated display showing determined skin and bone thicknesses as output. Image generated using ChatGPT (OpenAI, 2026).

6.4 Regulatory and Clinical Validation Considerations

Future work should include a staged validation roadmap based on the final intended purpose of the device. A first step would be to perform a preliminary regulatory assessment to determine whether the system should be classified as a medical device or as a simpler measuring tool. If the device is intended to support patient selection, preoperative assessment, or intraoperative decision-making for Ponto implantation, it may be considered an active diagnostic device and would likely require formal

clinical evaluation. However, the final classification would need to be determined through a formal regulatory assessment.

Once technical feasibility has been demonstrated through experimental validation, a limited non-invasive volunteer study could be performed to assess usability, operator dependence and anatomical variability in the temporal bone region. At a later stage, a clinical performance study could compare ultrasound-based thickness estimates with an accepted reference method, such as CT-based measurements or intra-operative findings in BAHS candidates.

Together, these steps would provide the basis for clinical evaluation, risk assessment and further development towards a prototype that is clinically usable.

7 Conclusion

This thesis investigated the feasibility of using ultrasound to determine local soft tissue and cortical bone thickness in the temporal bone region relevant to implantation of the Ponto system. The work was motivated by the need for a non-invasive and site-specific preoperative method that could support implant and abutment selection while reducing reliance on intraoperative measurements and ionizing imaging methods. Using analytical modelling and numerical simulations, the study evaluated whether ultrasound could provide sufficient measurement accuracy under anatomically relevant conditions.

The results showed that, under idealized simulation conditions, the relevant interface reflections could be identified consistently across all investigated configurations. The buffer rod-skin, skin-bone, and bone-dura reflections appeared in the expected temporal sequence, enabling determination of both soft tissue and cortical bone thickness.

The findings demonstrated that accurate thickness determination depends on the balance between signal amplitude, temporal compactness, and echo separability. Chirp excitation provided high voltage peaks and short SPLs, although pulse excitation showed comparable overall performance. Cortical bone thickness consistently exhibited lower ToF error than soft tissue thickness, indicating reliable determination despite the more complex propagation conditions in hard tissue. Based on the combined results, a promising intermediate-frequency operating range was identified, providing a suitable balance between temporal resolution, signal detectability, and propagation behaviour.

The achieved accuracy indicates that the method has potential to meet the clinical requirements considered in this thesis. ToF errors generally remained below 2–3 %, corresponding to thickness deviations acceptable for supporting implant and abutment selection in the Ponto system. The method also remained robust in the presence of additional anatomical structures and secondary reflections.

In conclusion, the results indicate that ultrasound has strong potential as a complementary tool for preoperative assessment in Ponto implantation. In addition to enabling non-invasive determination of soft tissue and cortical bone thickness, the method may support site-specific evaluation of the temporal bone region to assist implant positioning while avoiding thin bone regions, large blood vessels, or air pockets. However, since the present work was limited to analytical and numerical modelling, experimental validation is required before the clinical applicability of the method can be established.

Bibliography

[1] *Deafness and hearing loss*, en. Accessed: Mar. 4, 2026. [Online]. Available: https://www.who.int/news-room/fact-sheets/detail/deafness-and-hearing-loss.

[2] S. E. Ellsperman, E. M. Nairn, and E. Z. Stucken, "Review of Bone Conduction Hearing Devices," *Audiology Research*, vol. 11, no. 2, pp. 207–219, May 2021, ISSN: 2039-4330. DOI: 10.3390/audiolres11020019. Accessed: Apr. 14, 2026. [Online]. Available: https://pmc.ncbi.nlm.nih.gov/articles/PMC8161441/.

[3] Oticonmedical.com, *Ponto Surgical Manual - Linear incision procedure*, 2023. Accessed: Apr. 11, 2026. [Online]. Available: https://bahsjourney.com/wp-content/uploads/2023/12/266971en_Surgical_Manual_2023.03_Original-file.pdf.

[4] D. Ensminger and L. J. Bond, *Ultrasonics: Fundamentals, Technologies, and Applications*, 4th ed. Boca Raton: CRC Press, Feb. 2024, ISBN: 978-0-429-28696-4. DOI: 10.1201/9780429286964.

[5] G.F.S., "The physical and biological effects of high-frequency sound-waves of great intensity: R. W. Wood and A. L. Loomis. (Phil. Mag., Sept., 1927)," *Journal of the Franklin Institute*, vol. 205, no. 1, pp. 151–153, Jan. 1928, ISSN: 0016-0032. DOI: 10.1016/S0016-0032(28)92379-0. Accessed: Apr. 28, 2026. [Online]. Available: https://www.sciencedirect.com/science/article/pii/S0016003228923790.

[6] P. A. Federspil, H. Tretbar, F. H. Bohlen, S. Glaser, and P. K. Plinkert, "Measurement of Skull Bone Thickness for Bone-Anchored Hearing Aids: An Experimental Study Comparing Both a Novel Ultrasound System (SonoPointer) and Computed Tomographic Scanning to Mechanical Measurements," en, vol. 31, no. 3, 2010. Accessed: Apr. 20, 2026.

[7] S. Hakim, K. Watkin, M. Elahi, and L. Lessard, "Measurement of cranial bone thickness using A-mode ultrasound," in *Proceedings of the 19th Annual International Conference of the IEEE Engineering in Medicine and Biology Society. 'Magnificent Milestones and Emerging Opportunities in Medical Engineering' (Cat. No.97CH36136)*, ISSN: 1094-687X, vol. 2, Oct. 1997, 613–616 vol.2. DOI: 10.1109/IEMBS.1997.757685. Accessed: Apr. 28, 2026. [Online]. Available: https://ieeexplore.ieee.org/document/757685.

[8] K. Stölzel, C. Bauknecht, K. Wernecke, and T. Schrom, "Measurement of skull thickness by ultrasound," ger, *Laryngo- Rhino- Otologie*, vol. 86, no. 2, pp. 107–111, Feb. 2007, ISSN: 0935-8943. DOI: 10.1055/s-2006-944755. Accessed: Apr. 28, 2026.

[9] H. Alexander and D. L. Miller, "Determining Skin Thickness with Pulsed Ultra Sound," *Journal of Investigative Dermatology*, vol. 72, no. 1, pp. 17–19, Jan. 1979, ISSN: 0022-202X. DOI: 10.1111/1523-1747.ep12530104. Accessed: Apr. 28, 2026. [Online]. Available: https://www.sciencedirect.com/science/article/pii/S0022202X15454259.

[10] M. Wróbel, M. Popko, and W. Szyfter, "Presurgical evaluation of retroauricular subcutaneous tissue thickness in BAHA surgery," eng, *Otology & Neurotology: Official Publication of the American Otological Society, American Neurotology Society [and] European Academy of Otology and Neurotology*, vol. 33, no. 3, pp. 421–424, Apr. 2012, ISSN: 1537-4505. DOI: 10.1097/MAO.0b013e318245cc68. Accessed: Apr. 28, 2026.

[11] *Ponto system*, en. Accessed: Apr. 15, 2026. [Online]. Available: https://www.oticonmedical.com/for-professionals/bone-anchored/ponto-system.

[12] *Bone Conduction Hearing | Oticon Medical*, en. Accessed: Apr. 15, 2026. [Online]. Available: https://www.oticonmedical.com/.

[13] H. Ellis and V. Mahadevan, "The surgical anatomy of the scalp," en, *Surgery (Oxford)*, vol. 32, e1–e5, May 2014, ISSN: 02639319. DOI: 10.1016/j.mpsur.2013.04.024. Accessed: Mar. 31, 2026. [Online]. Available: https://linkinghub.elsevier.com/retrieve/pii/S0263931913001075.

[14] *The Scalp - Layers - Innervation - Blood Supply*. Accessed: Mar. 31, 2026. [Online]. Available: https://teachmeanatomy.info/head/areas/scalp/.

[15] F. Gaillard, *English: Illustration depicting the layers of the scalp and meninges.* Jan. 2010. Accessed: Apr. 20, 2026. [Online]. Available: https://commons.wikimedia.org/wiki/File:Layers_of_the_scalp_and_meninges.png.

[16] B. W. Anderson, M. W. Kortz, A. C. Black, and K. A. Al Kharazi, "Anatomy, Head and Neck, Skull," eng, in *StatPearls*, Treasure Island (FL): StatPearls Publishing, 2025. Accessed: Mar. 6, 2026. [Online]. Available: http://www.ncbi.nlm.nih.gov/books/NBK499834/.

[17] LadyofHats, *File:Human skull side simplified (bones).svg*, Jan. 2007. Accessed: Mar. 6, 2026. [Online]. Available: https://commons.wikimedia.org/wiki/File:Human_skull_side_simplified_(bones).svg.

[18] A. B. Dublin and M. A. Al-Dhahir, "Anatomy, Head and Neck, Temporal Region," eng, in *StatPearls*, Treasure Island (FL): StatPearls Publishing, 2025. Accessed: Mar. 6, 2026. [Online]. Available: http://www.ncbi.nlm.nih.gov/books/NBK482497/.

[19] O. College, *English: Illustration from Anatomy & Physiology, Connexions Web site. http://cnx.org/content/col11496/1.6/, Jun 19, 2013.* Apr. 2013. Accessed: Mar. 6, 2026. [Online]. Available: https://commons.wikimedia.org/wiki/File:708_Temporal_Bone.jpg.

[20] V. Kekere and K. Alsayouri, "Anatomy, Head and Neck, Dura Mater," eng, in *StatPearls*, Treasure Island (FL): StatPearls Publishing, 2026. Accessed: Apr. 15, 2026. [Online]. Available: http://www.ncbi.nlm.nih.gov/books/NBK545301/.

[21] A. Sánchez López de Nava and S. Lasrado, "Physiology, Ear," eng, in *StatPearls*, Treasure Island (FL): StatPearls Publishing, 2025. Accessed: Mar. 4, 2026. [Online]. Available: http://www.ncbi.nlm.nih.gov/books/NBK540992/.

[22] R. A. Dobie and S. V. Hemel, "Basics of Sound, the Ear, and Hearing," en, in *Hearing Loss: Determining Eligibility for Social Security Benefits*, National Academies Press (US), 2004. Accessed: Mar. 4, 2026. [Online]. Available: https://www.ncbi.nlm.nih.gov/books/NBK207834/.

[23] OpenStax, *File:1404 The Structures of the Ear.jpg*, May 2016. Accessed: Mar. 6, 2026. [Online]. Available: https://commons.wikimedia.org/wiki/File:1404_The_Structures_of_the_Ear.jpg.

[24] S. Stenfelt, "Inner ear contribution to bone conduction hearing in the human," *Hearing Research*, Annual reviews 2015, vol. 329, pp. 41–51, Nov. 2015, ISSN: 0378-5955. DOI: 10.1016/j.heares.2014.12.003. Accessed: Mar. 4, 2026. [Online]. Available: https://www.sciencedirect.com/science/article/pii/S0378595514002020.

[25] J. P. Brandt and R. Winters, "Bone Conduction Evaluation," eng, in *StatPearls*, Treasure Island (FL): StatPearls Publishing, 2025. Accessed: Mar. 4, 2026. [Online]. Available: http://www.ncbi.nlm.nih.gov/books/NBK578177/.

[26] T. Sooriyamoorthy and O. De Jesus, "Conductive Hearing Loss," eng, in *StatPearls*, Treasure Island (FL): StatPearls Publishing, 2026. Accessed: Mar. 13, 2026. [Online]. Available: http://www.ncbi.nlm.nih.gov/books/NBK563267/.

[27] A. Pantaleo, A. Murri, G. Cavallaro, V. Pontillo, D. Auricchio, and N. Quaranta, "Single-Sided Deafness and Hearing Rehabilitation Modalities: Contralateral Routing of Signal Devices, Bone Conduction Devices, and Cochlear Implants," *Brain Sciences*, vol. 14, no. 1, p. 99, Jan. 2024, ISSN: 2076-3425. DOI: 10.3390/brainsci14010099. Accessed: Mar. 6, 2026. [Online]. Available: https://pmc.ncbi.nlm.nih.gov/articles/PMC10814000/.

[28] T. G. Calon et al., "Minimally Invasive Ponto Surgery Versus the Linear Incision Technique With Soft Tissue Preservation for Bone Conduction Hearing Implants: A Multicenter Randomized Controlled Trial," *Otology & Neurotology*, vol. 39, no. 7, pp. 882–893, Aug. 2018, ISSN: 1531-7129. DOI: 10.1097/MAO.0000000000001852. Accessed: Apr. 11, 2026. [Online]. Available: https://pmc.ncbi.nlm.nih.gov/articles/PMC6075882/.

[29] S. Reinfeldt, B. Håkansson, H. Taghavi, and M. Eeg-Olofsson, "New developments in bone-conduction hearing implants: A review," *Medical Devices (Auckland, N.Z.)*, vol. 8, pp. 79–93, Jan. 2015, ISSN: 1179-1470. DOI: 10.2147/MDER.S39691. Accessed: Apr. 14, 2026. [Online]. Available: https://pmc.ncbi.nlm.nih.gov/articles/PMC4303401/.

[30] Oticonmedical.com, *Candidacy Guide*, 2017. Accessed: Apr. 14, 2026. [Online]. Available: https://www.oticonmedical.com/-/media/medical/main/files/for-professionals/bahs/audiological-materials/guide/eng/candidacy-guide---english---m52735.pdf?la=en-gb.

[31] *Cochlear™ Baha® System | Bone Conduction Hearing Device*, en. Accessed: Apr. 14, 2026. [Online]. Available: https://www.cochlear.com/us/en/home/products-and-accessories/cochlear-baha-system.

[32] H. Lagerkvist, K. Carvalho, M. Holmberg, U. Petersson, C. Cremers, and M. Hultcrantz, "Ten years of experience with the Ponto bone-anchored hearing system—A systematic literature review," *Clinical Otolaryngology*, vol. 45, no. 5, pp. 667–680, Sep. 2020, ISSN: 1749-4478. DOI: 10.1111/coa.13556. Accessed: Mar. 29, 2026. [Online]. Available: https://pmc.ncbi.nlm.nih.gov/articles/PMC7496709/.

[33] M. L. Johansson, "The percutaneous implant. The effects of design, host site and surgery on the tissue response," en, 2018, Version Number: 1. DOI: 10.13140/RG.2.2.12834.73927/1. Accessed: Mar. 29, 2026. [Online]. Available: https://www.researchgate.net/doi/10.13140/RG.2.2.12834.73927/1.

[34] Oticonmedical.com, *Addenum to Surgical Manual - Including the MONO procedure*, 2021. Accessed: Apr. 11, 2026.

[35] L. D. S. Cruz et al., "Minimally invasive surgery as a new clinical standard for bone anchored hearing implants—real-world data from 10 years of follow-up and 228 surgeries," *Frontiers in Surgery*, vol. 10, p. 1 209 927, Jul. 2023, ISSN: 2296-875X. DOI: 10.3389/fsurg.2023.1209927. Accessed: Apr. 11, 2026. [Online]. Available: https://pmc.ncbi.nlm.nih.gov/articles/PMC10351910/.

[36] Oticonmedical.com, *The MONO procedure - functional and clinical aspects of a novel one-step drill system for installation of the Ponto system*, 2021. Accessed: Apr. 11, 2026. [Online]. Available: https://assets-we.cas.dgs.com/-/media/medical/main/files/for-professionals/bahs/surgical-materials/mono/236459ukomwhite-papermono-procedure202109low.pdf?la=en&rev=91D2&hash=A0D7CE342870322296F8403750CC4F16.

[37] V. Gibbs, D. Cole, and A. Sassano, *Ultrasound physics and technology: how, why and when*. Edinburgh ; New York: Churchill Livingstone/Elsevier, 2009, ISBN: 978-0-7020-3041-3. Accessed: Mar. 13, 2026.

[38] M. A. Sahin, M. Ali, J. Park, and G. Destgeer, "Fundamentals of Acoustic Wave Generation and Propagation," en, in *Acoustic Technologies in Biology and Medicine*, A. Ozcelik, R. Becker, and T. J. Huang, Eds., 1st ed., Wiley, Dec. 2023, pp. 1–36. DOI: 10.1002/9783527841325.ch1. Accessed: Mar. 13, 2026. [Online]. Available: https://onlinelibrary.wiley.com/doi/10.1002/9783527841325.ch1.

[39] Y. Takeuchi, "An investigation of a spread energy method for medical ultrasound systems: Part one: Theory and investigation," *Ultrasonics*, vol. 17, no. 4, pp. 175–182, Jul. 1979, ISSN: 0041-624X. DOI: 10.1016/0041-624X(79)90035-0. Accessed: Apr. 20, 2026.

[40] J. Krautkrämer and H. Krautkrämer, *Ultrasonic Testing of Materials*, en. Berlin, Heidelberg: Springer Berlin Heidelberg, 1990. DOI: 10.1007/978-3-662-10680-8. Accessed: Apr. 20, 2026. [Online]. Available: http://link.springer.com/10.1007/978-3-662-10680-8.

[41] C. Desilets, J. Fraser, and G. Kino, "The design of efficient broad-band piezoelectric transducers," *IEEE Transactions on Sonics and Ultrasonics*, vol. 25, no. 3, pp. 115–125, May 1978, ISSN: 2162-1403. DOI: 10.1109/T-SU.1978.31001. Accessed: Mar. 13, 2026. [Online]. Available: https://ieeexplore.ieee.org/document/1539077/.

[42] D. White, G. Curry, and R. Stevenson, "The acoustic characteristics of the skull," en, *Ultrasound in Medicine & Biology*, vol. 4, no. 3, pp. 225–252, Jan. 1978, ISSN: 03015629. DOI: 10.1016/0301-5629(78)90054-6. Accessed: Apr. 20, 2026. [Online]. Available: https://linkinghub.elsevier.com/retrieve/pii/0301562978900546.

[43] T. Rahne, S. Svensson, H. Lagerkvist, M. Holmberg, S. K. Plontke, and C. Wenzel, "Assessment of Temporal Bone Thickness for Implantation of a New Active Bone-Conduction Transducer," en-US, *Otology & Neurotology*, vol. 42, no. 2, p. 278, Feb. 2021, ISSN: 1531-7129. DOI: 10.1097/MAO.0000000000002919. Accessed: Apr. 20, 2026. [Online]. Available: https://journals.lww.com/otology-neurotology/fulltext/2021/02000/assessment_of_temporal_bone_thickness_for.24.aspx.

[44] Y. Chang, N. Kim, and S. Stenfelt, "The development of a whole-head human finite-element model for simulation of the transmission of bone-conducted sound," en, *The Journal of the Acoustical Society of America*, vol. 140, no. 3, pp. 1635–1651, Sep. 2016, ISSN: 0001-4966, 1520-8524. DOI: 10.1121/1.4962443. Accessed: Apr. 20, 2026. [Online]. Available: https://pubs.aip.org/jasa/article/140/3/1635/649539/The-development-of-a-whole-head-human-finite.

[45] A. Auperrin, R. Delille, D. Lesueur, K. Bruyère, C. Masson, and P. Drazétic, "Geometrical and material parameters to assess the macroscopic mechanical behaviour of fresh cranial bone samples," en, *Journal of Biomechanics*, vol. 47, no. 5, pp. 1180–1185, Mar. 2014, ISSN: 00219290. DOI: 10.1016/j.jbiomech.2013.10.060. Accessed: Apr. 20, 2026. [Online]. Available: https://linkinghub.elsevier.com/retrieve/pii/S0021929013005526.

[46] J. Lim, I. Dobrev, C. Röösli, S. Stenfelt, and N. Kim, "Development of a finite element model of a human head including auditory periphery for understanding of bone-conducted hearing," en, *Hearing Research*, vol. 421, p. 108 337, Aug. 2022, ISSN: 03785955. DOI: 10.1016/j.heares.2021.108337. Accessed: Apr. 20, 2026. [Online]. Available: https://linkinghub.elsevier.com/retrieve/pii/S0378595521001714.

[47] J. Gu and Y. Jing, "Modeling of wave propagation for medical ultrasound: A review," *IEEE Transactions on Ultrasonics, Ferroelectrics, and Frequency Control*, vol. 62, no. 11, pp. 1979–1992, Nov. 2015, ISSN: 0885-3010. DOI: 10.1109/TUFFC.2015.007034. Accessed: May 12, 2026. [Online]. Available: http://ieeexplore.ieee.org/document/7321705/.

A Appendix: Methods

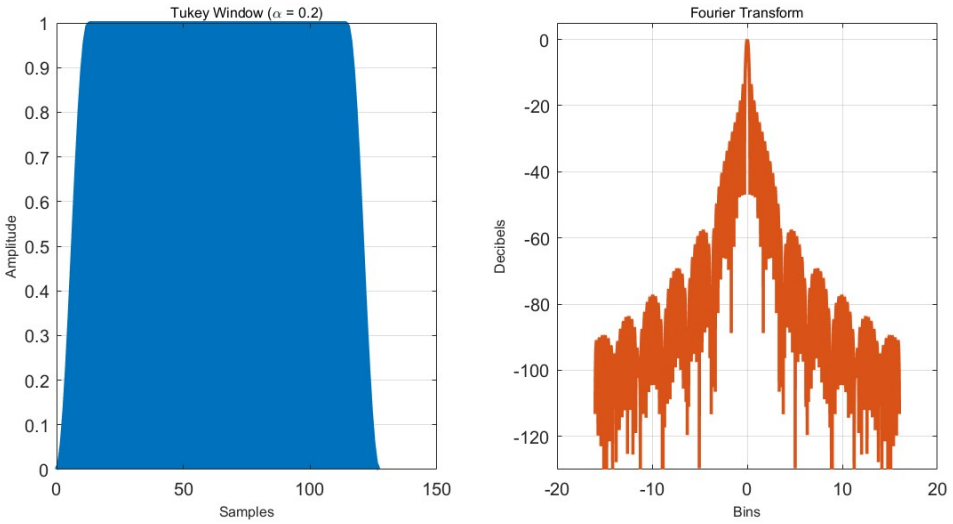

Figure A.1: Tukey window in the time domain (left) and corresponding Fourier transform magnitude response in the frequency domain (right).

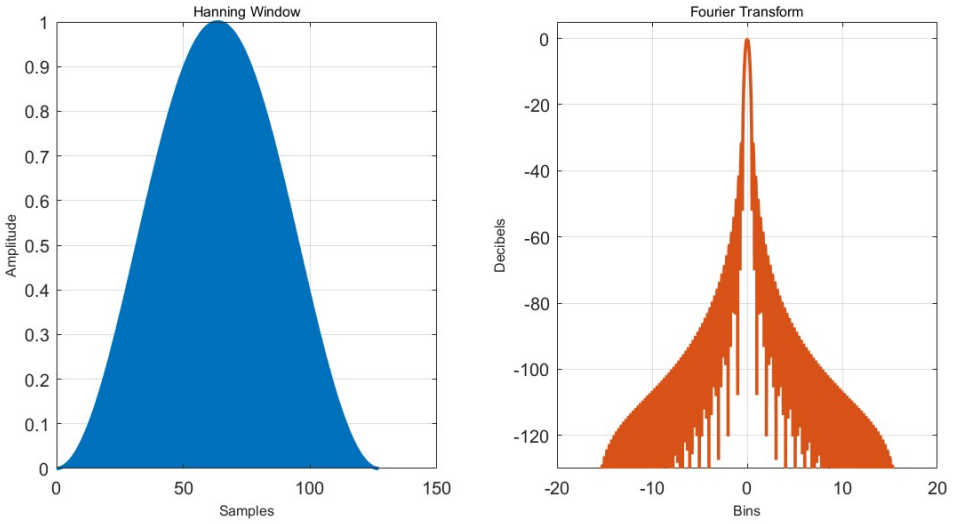

Figure A.2: Hanning window in the time domain (left) and corresponding Fourier transform magnitude response in the frequency domain (right).

B Appendix: Study Results

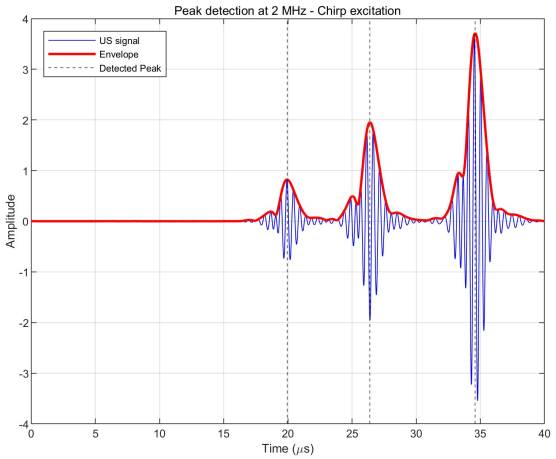

(a) 2 MHz

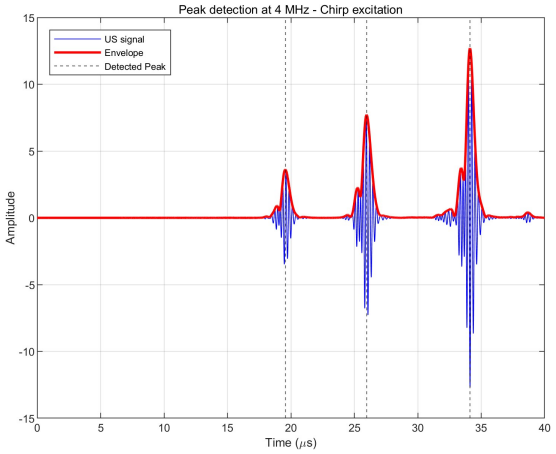

(b) 4 MHz

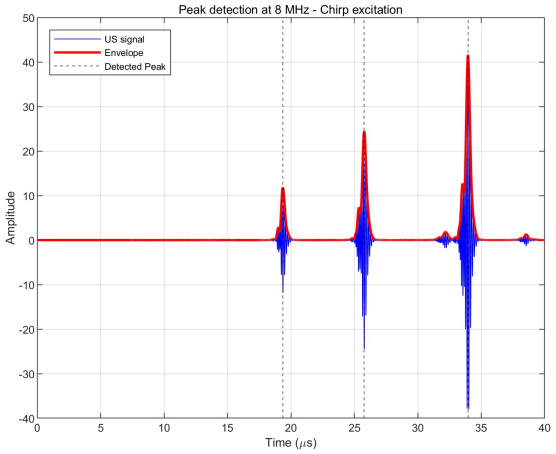

(c) 8 MHz

Figure B.1: Comparison of raw US signals, amplitude envelopes, and detected peaks with chirp excitations for different frequencies: (a) 2 MHz, (b) 4 MHz, and (c) 8 MHz.

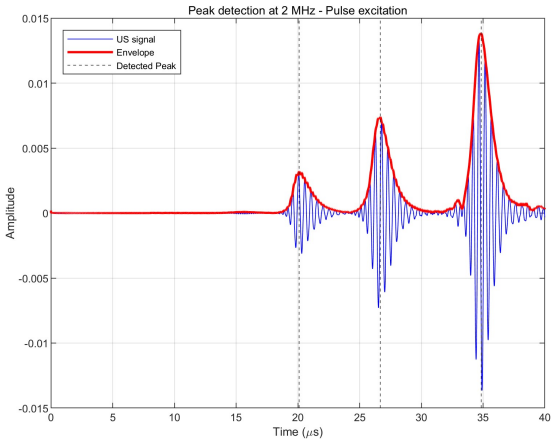

(a) 2 MHz

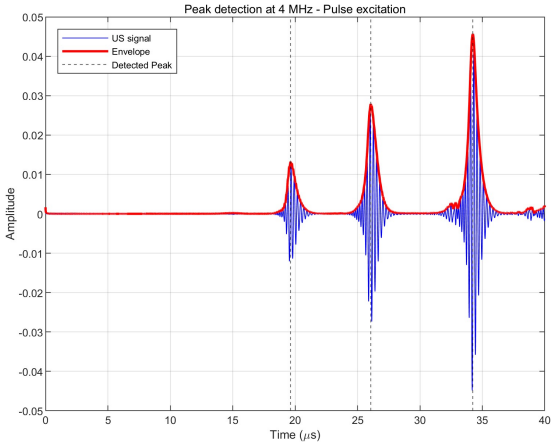

(b) 4 MHz

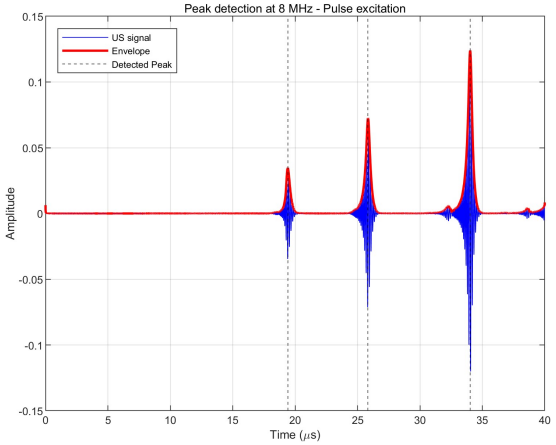

(c) 8 MHz

Figure B.2: Comparison of raw US signals, amplitude envelopes, and detected peaks with pulse excitations for different frequencies: (a) 2 MHz, (b) 4 MHz, and (c) 8 MHz.

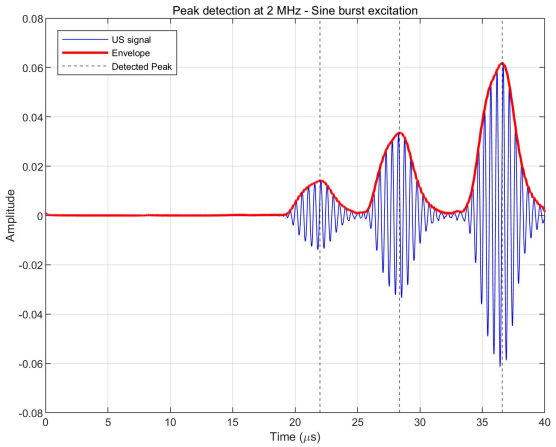

(a) 2 MHz

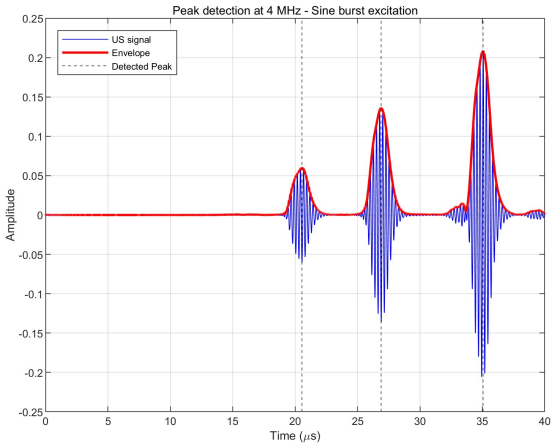

(b) 4 MHz

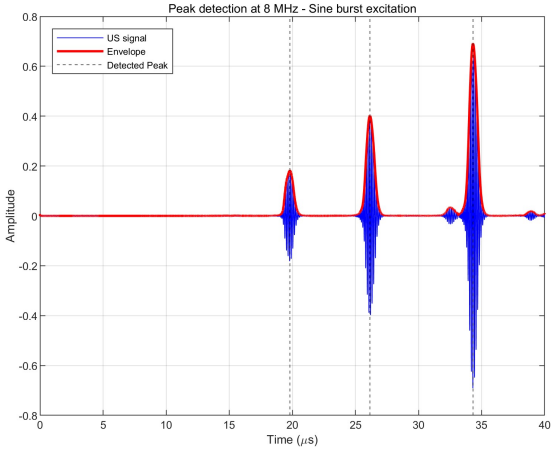

(c) 8 MHz

Figure B.3: Comparison of raw US signals, amplitude envelopes, and detected peaks with sine burst excitations for different frequencies: (a) 2 MHz, (b) 4 MHz, and (c) 8 MHz.

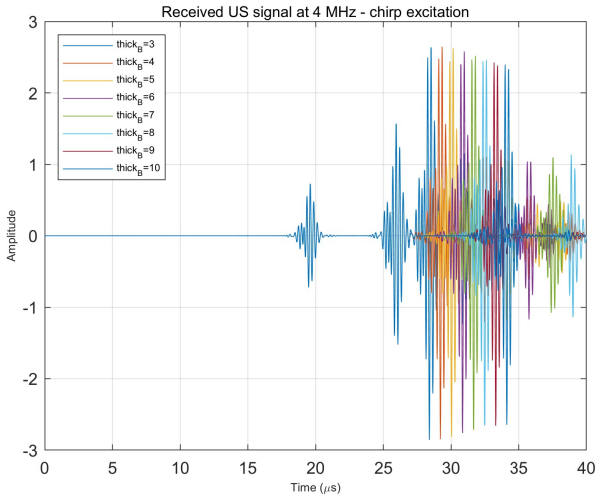

(a) 4 MHz

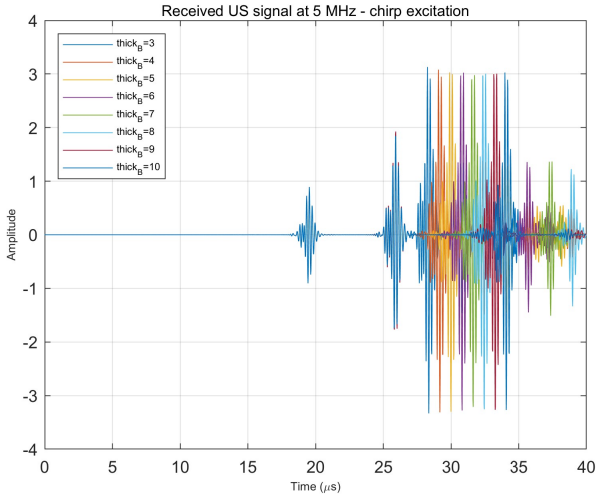

(b) 5 MHz

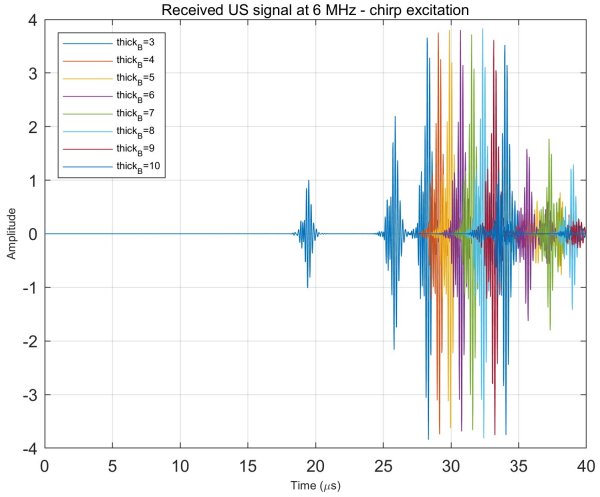

(c) 6 MHz

Figure B.4: Comparison of received ultrasound signals with chirp excitation across varying bone thicknesses (3–10 mm), illustrating frequency-dependent signal behaviour, for different operating frequencies: (a) 4 MHz, (b) 5 MHz, and (c) 6 MHz.

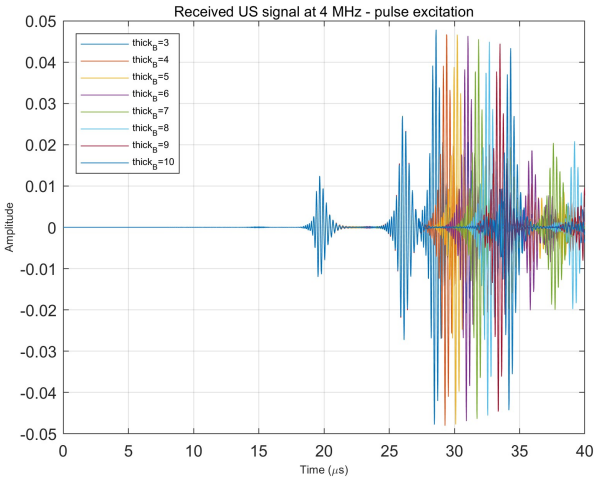

(a) 4 MHz

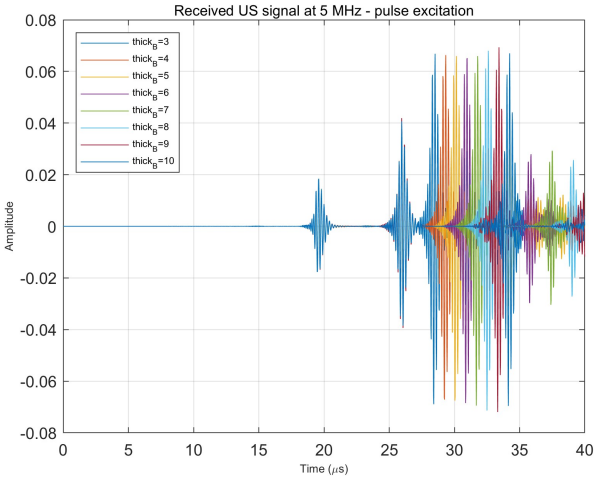

(b) 5 MHz

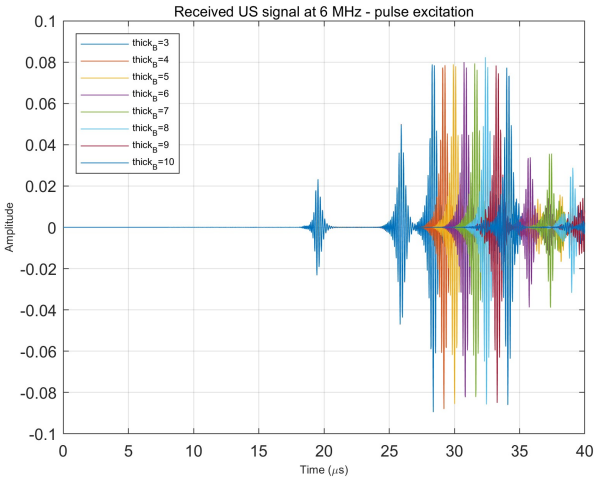

(c) 6 MHz

Figure B.5: Comparison of received ultrasound signals with pulse excitation across varying bone thicknesses (3–10 mm), illustrating frequency-dependent signal behaviour, for different operating frequencies: (a) 4 MHz, (b) 5 MHz, and (c) 6 MHz.

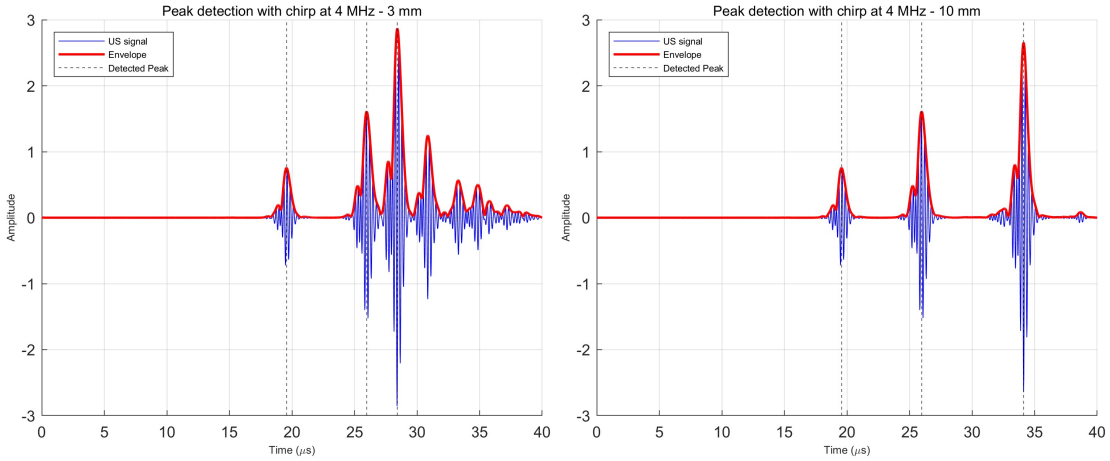

(a) 4 MHz, 3 mm

(b) 4 MHz, 10 mm

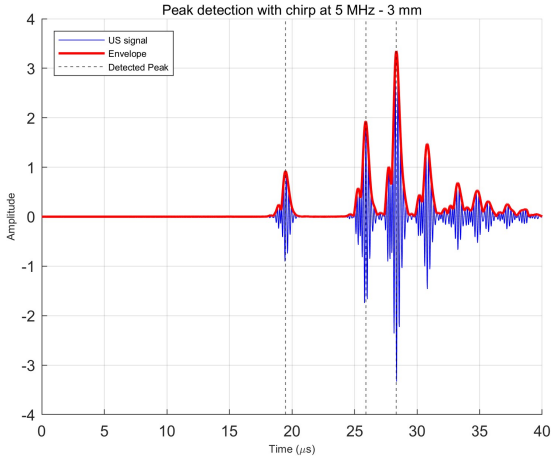

(c) 5 MHz, 3 mm

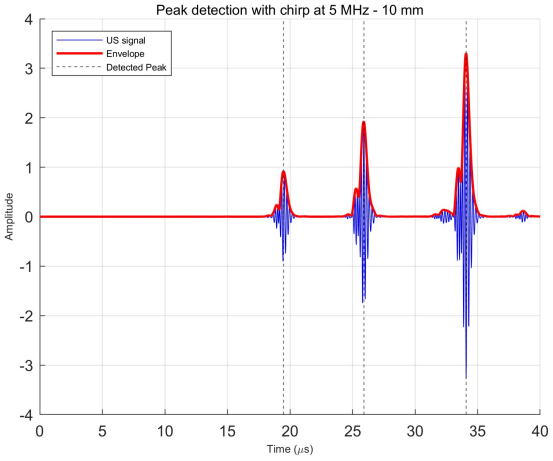

(d) 5 MHz, 10 mm

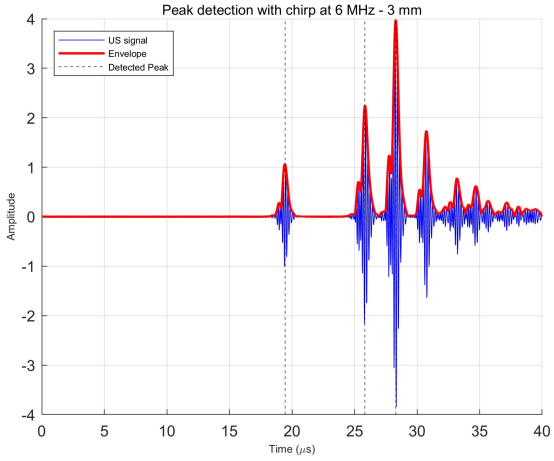

(e) 6 MHz, 3 mm

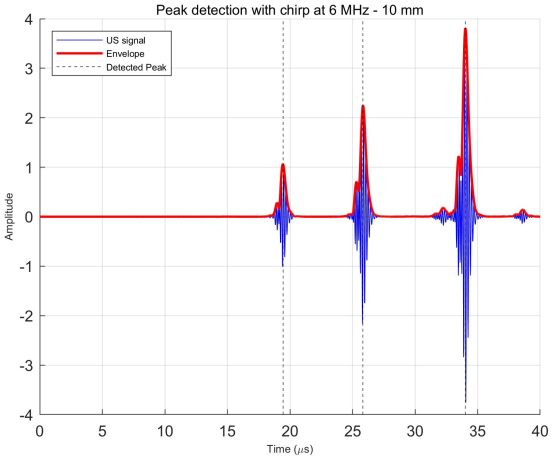

(f) 6 MHz, 10 mm

Figure B.6: Comparison of raw US signals, amplitude envelopes, and detected peaks with chirp excitation, illustrating the effect of bone thickness for extreme-cases of 3 mm and 10 mm, for different operating frequencies: (a, b) 4 MHz, (c, d) 5 MHz, (e, f) and 6 MHz.

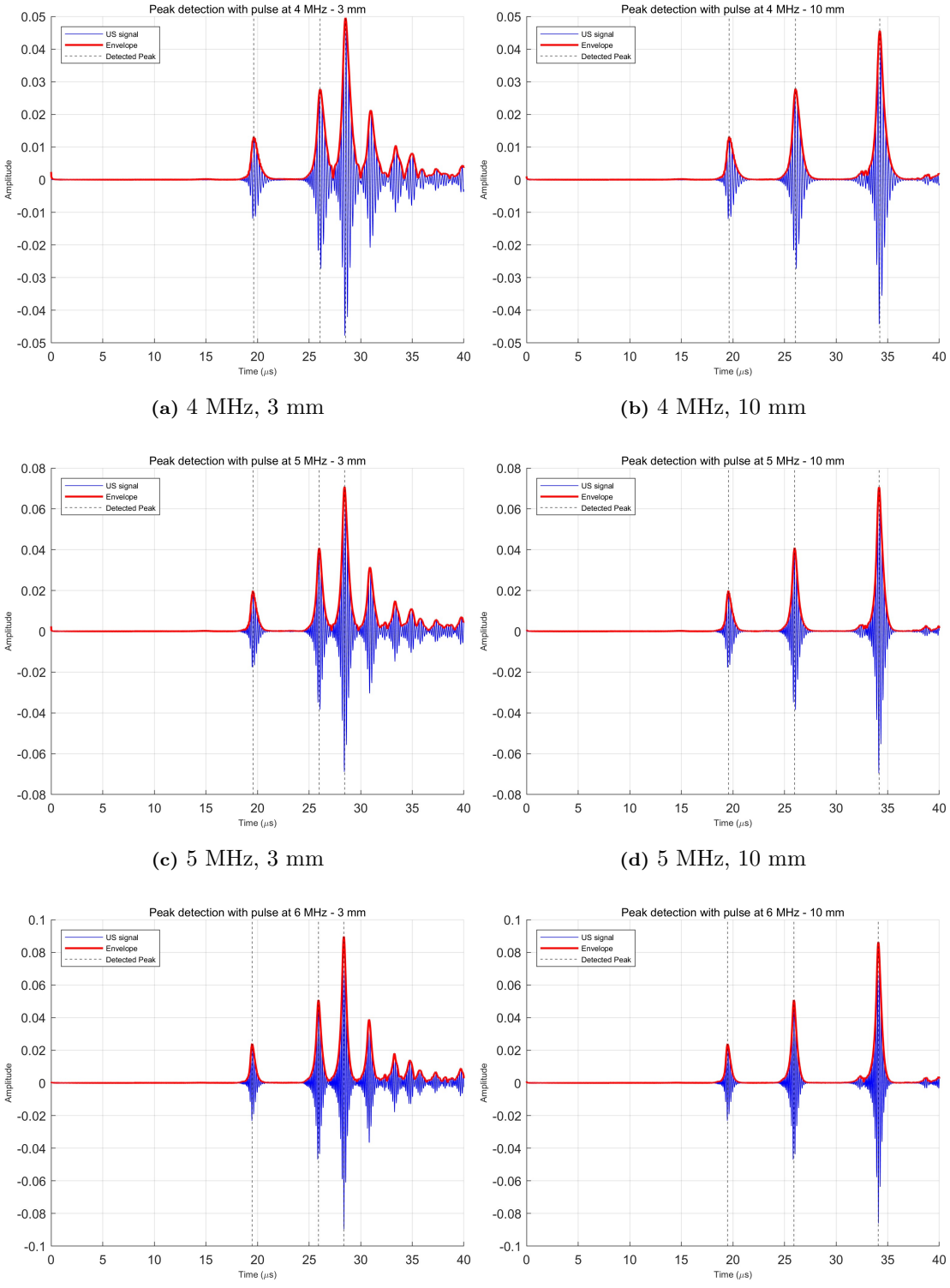

(a) 4 MHz, 3 mm

(b) 4 MHz, 10 mm

(c) 5 MHz, 3 mm

(d) 5 MHz, 10 mm

(e) 6 MHz, 3 mm

(f) 6 MHz, 10 mm

Figure B.7: Comparison of raw US signals, amplitude envelopes, and detected peaks with pulse excitation, illustrating the effect of bone thickness for extreme-cases of 3 mm and 10 mm, for different operating frequencies: (a, b) 4 MHz, (c, d) 5 MHz, (e, f) and 6 MHz.

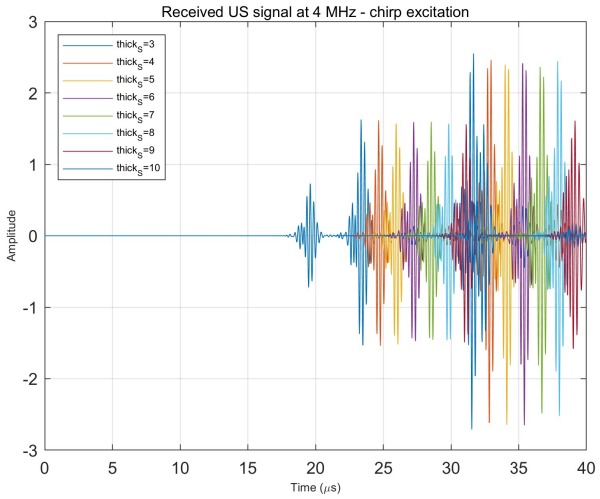

(a) 4 MHz

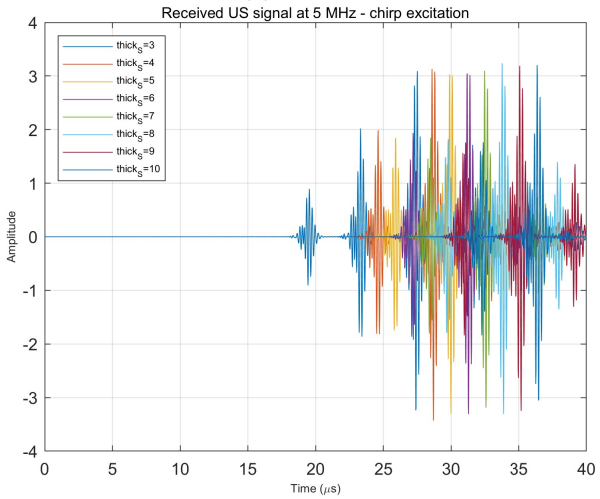

(b) 5 MHz

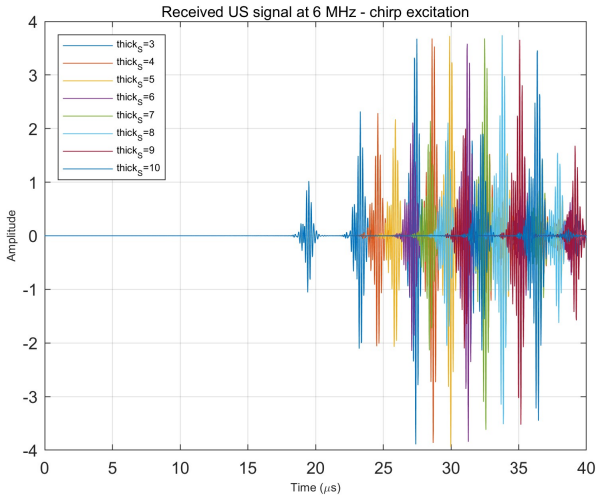

(c) 6 MHz

Figure B.8: Comparison of received ultrasound signals with chirp excitation across varying skin thicknesses (3–10 mm), illustrating frequency-dependent signal behaviour, for different operating frequencies: (a) 4 MHz, (b) 5 MHz, and (c) 6 MHz.

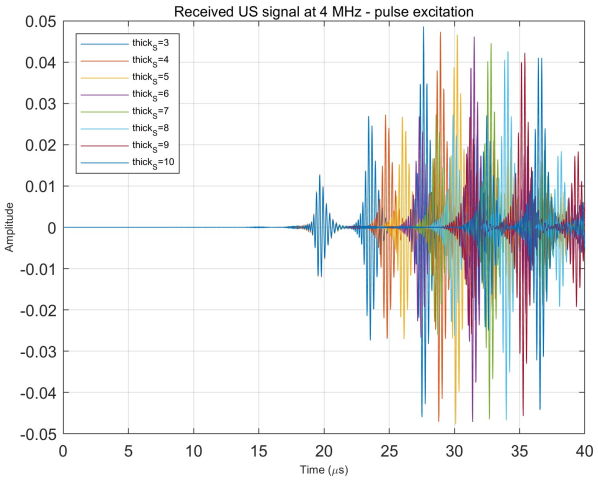

(a) 4 MHz

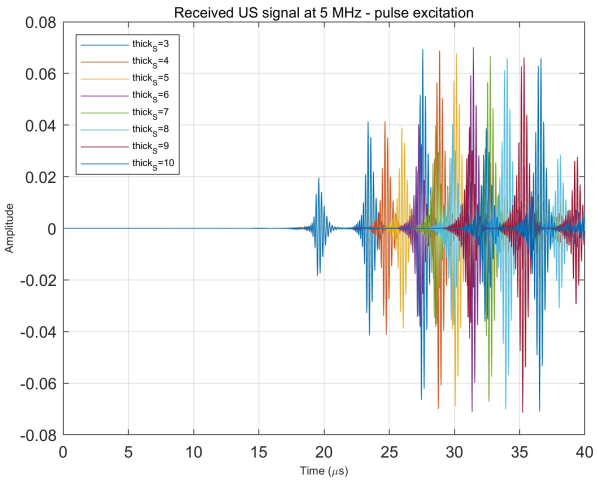

(b) 5 MHz

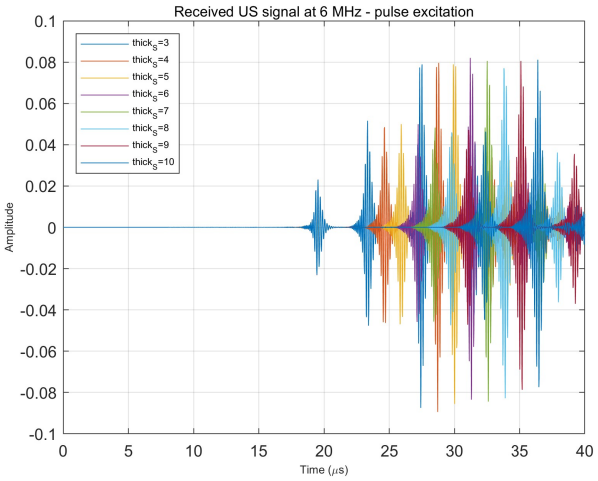

(c) 6 MHz

Figure B.9: Comparison of received ultrasound signals with pulse excitation across varying skin thicknesses (3–10 mm), illustrating frequency-dependent signal behaviour, for different operating frequencies: (a) 4 MHz, (b) 5 MHz, and (c) 6 MHz.

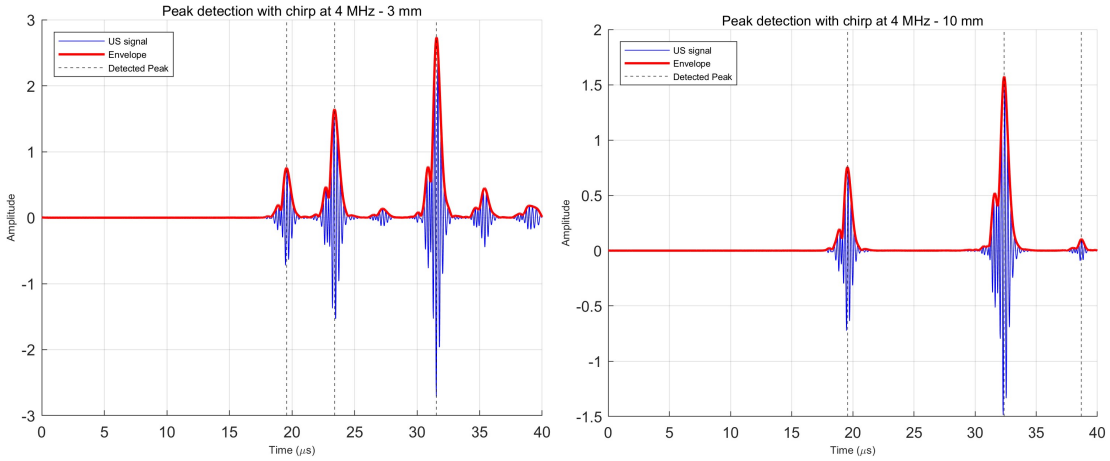

(a) 4 MHz, 3 mm

(b) 4 MHz, 10 mm

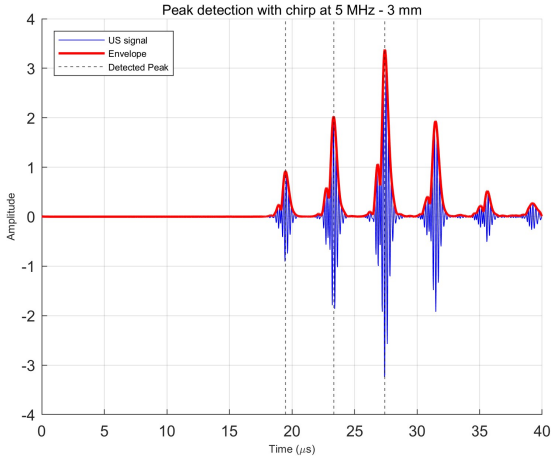

(c) 5 MHz, 3 mm

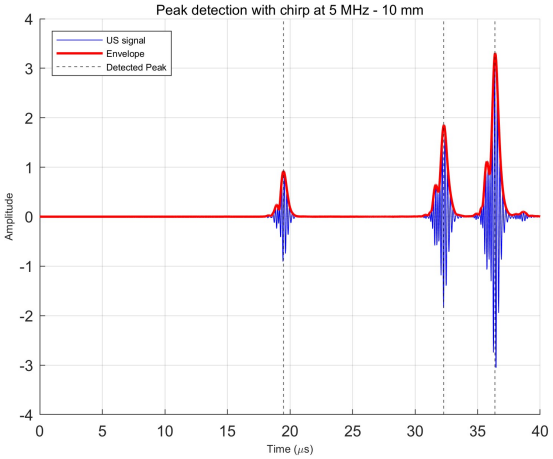

(d) 5 MHz, 10 mm

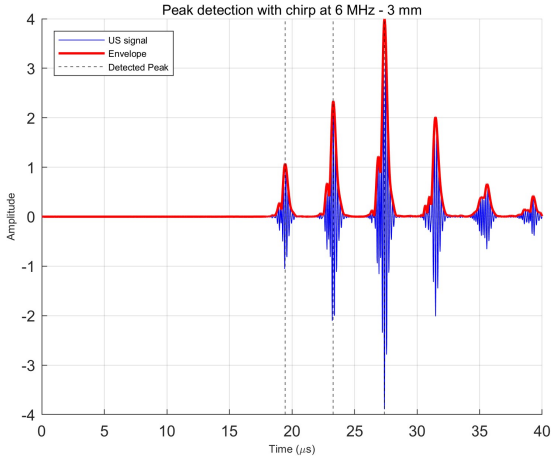

(e) 6 MHz, 3 mm

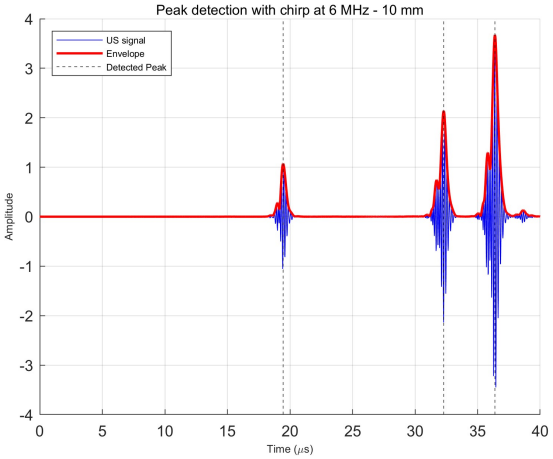

(f) 6 MHz, 10 mm

Figure B.10: Comparison of raw US signals, amplitude envelopes, and detected peaks with chirp excitation, illustrating the effect of skin thickness for extreme-cases of 3 mm and 10 mm, for different operating frequencies: (a, b) 4 MHz, (c, d) 5 MHz, (e, f) and 6 MHz.

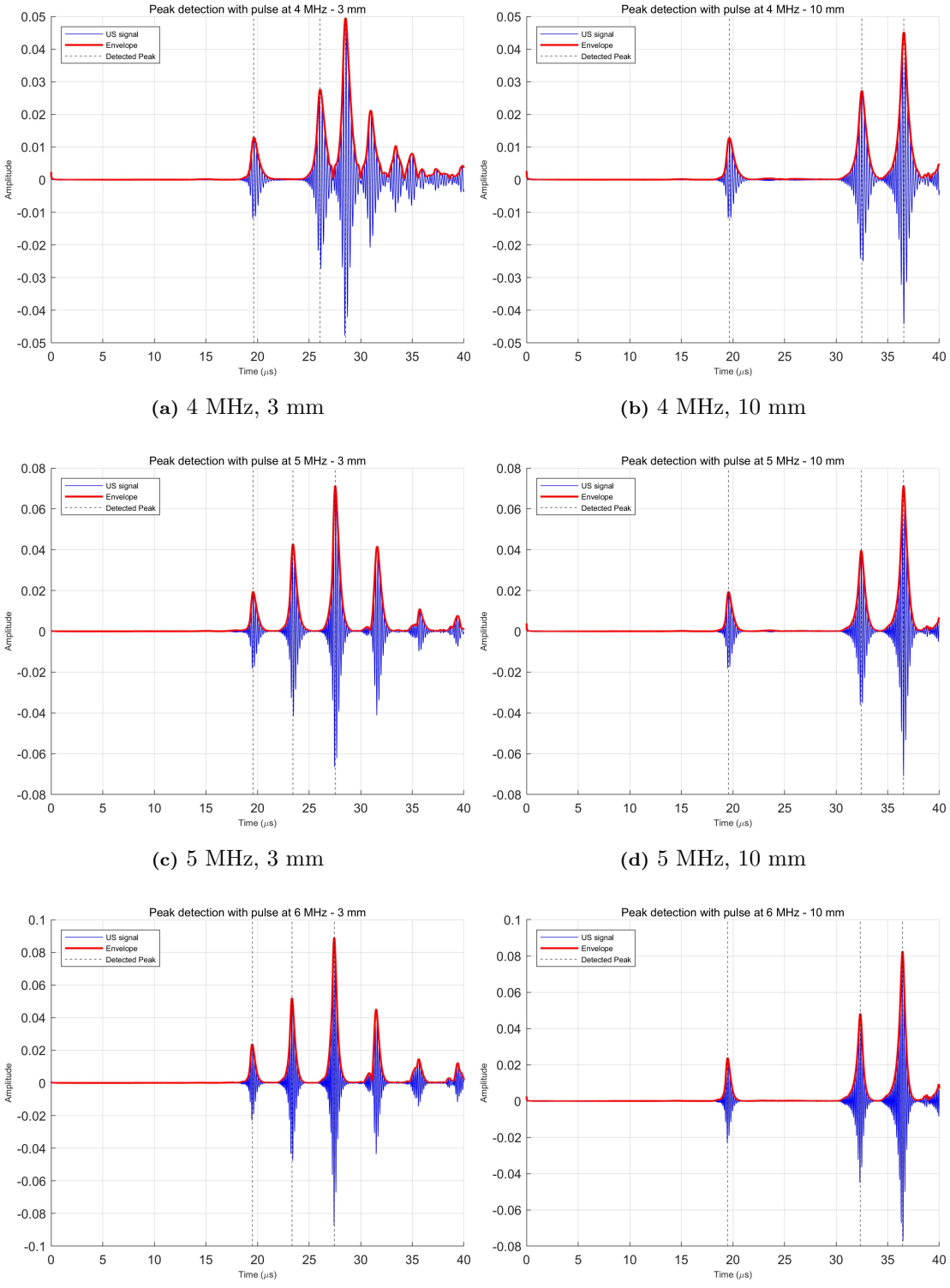

(a) 4 MHz, 3 mm

(b) 4 MHz, 10 mm

(c) 5 MHz, 3 mm

(d) 5 MHz, 10 mm

(e) 6 MHz, 3 mm

(f) 6 MHz, 10 mm

Figure B.11: Comparison of raw US signals, amplitude envelopes, and detected peaks with pulse excitation, illustrating the effect of skin thickness for extreme-cases of 3 mm and 10 mm, for different operating frequencies: (a, b) 4 MHz, (c, d) 5 MHz, (e, f) and 6 MHz.

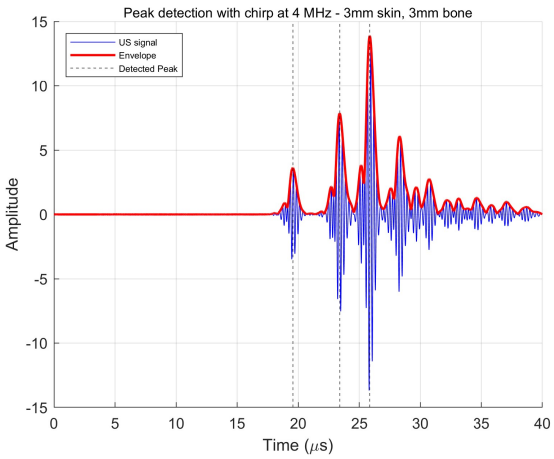

(a) Chirp excitation, 4 MHz

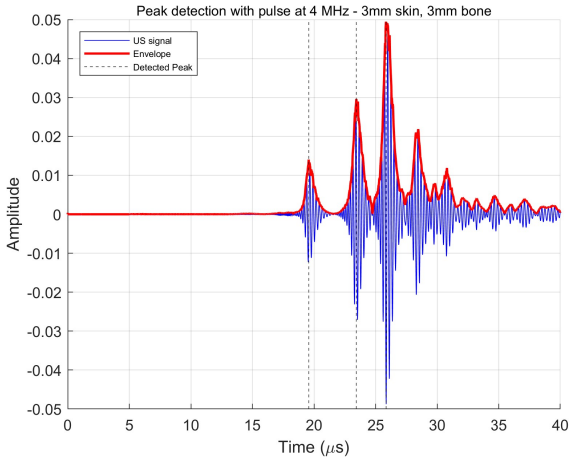

(b) Pulse excitation, 4 MHz

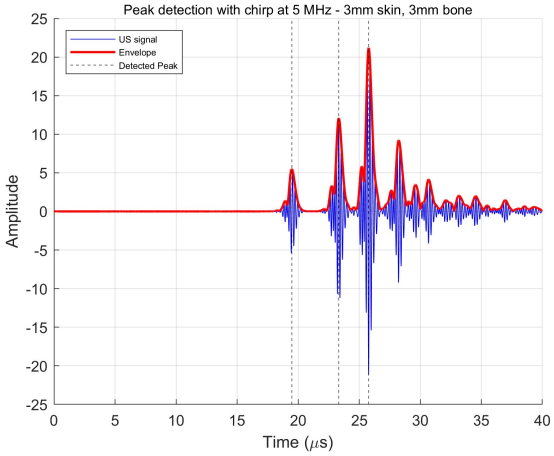

(c) Chirp excitation, 5 MHz

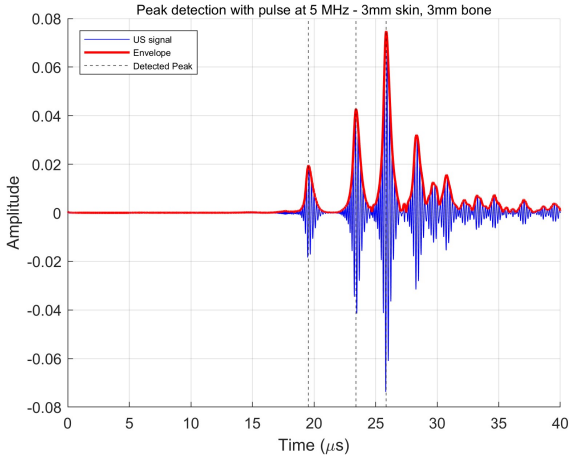

(d) Pulse excitation, 5 MHz

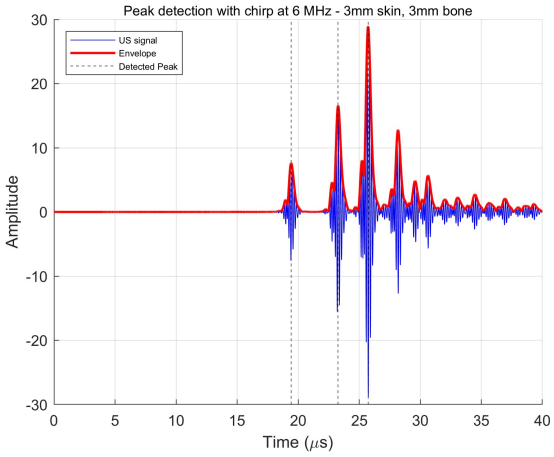

(e) Chirp excitation, 6 MHz

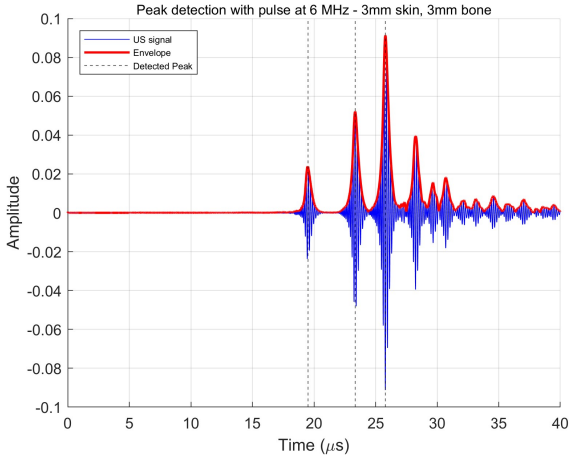

(f) Pulse excitation, 6 MHz

Figure B.12: Comparison of raw US signals, amplitude envelopes, and detected peaks with chirp and pulse excitation, under worst-case operating conditions for different operating frequencies: (a, b) 4 MHz, (c, d) 5 MHz, (e, f) and 6 MHz.

DEPARTMENT OF ELECTRICAL ENGINEERING
CHALMERS UNIVERSITY OF TECHNOLOGY
Gothenburg, Sweden
www.chalmers.se

CHALMERS
UNIVERSITY OF TECHNOLOGY